Cancer Cell

Article

Single-cell analysis defines a pancreatic fibroblast lineage that supports anti-tumor immunity

Graphical abstract

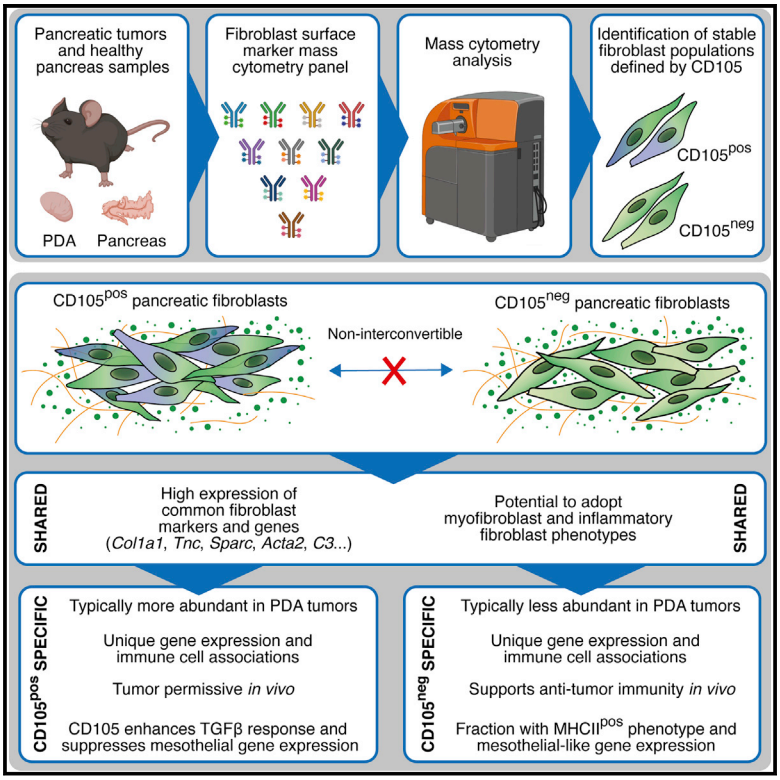

Highlights

- Mass cytometry analysis of mesenchymal stroma in murine normal and tumor tissue
- Mesenchymal heterogeneity is a feature of human and murine tissues and tumors
- CD105 expression distinguishes two pancreatic fibroblast lineages
- CD105^{neg} pancreatic fibroblasts support anti-tumor immunity to control tumor growth

Authors

Colin Hutton, Felix Heider, Adrian Blanco-Gomez, ..., Santiago Zelenay, Jennifer P. Morton, Claus Jørgensen

Correspondence

claus.jorgensen@cruk.manchester.ac.uk

In brief

Hutton et al. use mass cytometry to chart stromal cells and describe mesenchymal states and lineages in pancreatic ductal adenocarcinoma. CD105 (*Eng*) expression distinguishes two pancreatic fibroblast lineages with distinct functions. CD105^{pos} fibroblasts are tumor permissive, whereas CD105^{neg} fibroblasts suppress tumor growth in a manner dependent on adaptive immunity.

Hutton et al., 2021, Cancer Cell *39*, 1227–1244
September 13, 2021
https://doi.org/10.1016/j.ccell.2021.06.017

CellPress

Cancer Cell

CellPress
OPEN ACCESS

Article

Single-cell analysis defines a pancreatic fibroblast lineage that supports anti-tumor immunity

Colin Hutton,[1] Felix Heider,[1] Adrian Blanco-Gomez,[1] Antonia Banyard,[2] Alexander Kononov,[1] Xiaohong Zhang,[1] Saadia Karim,[3] Viola Paulus-Hock,[3] Dale Watt,[3] Nina Steele,[4,5,6] Samantha Kemp,[5,7] Elizabeth K.J. Hogg,[1] Joanna Kelly,[1] Rene-Filip Jackstadt,[3] Filipa Lopes,[8] Matteo Menotti,[9] Luke Chisholm,[10] Angela Lamarca,[11] Juan Valle,[11,12] Owen J. Sansom,[3,13] Caroline Springer,[8] Angeliki Malliri,[9] Richard Marais,[10] Marina Pasca di Magliano,[4,5] Santiago Zelenay,[14] Jennifer P. Morton,[3,13] and Claus Jørgensen[1,15,*]

[1]Systems Oncology, Cancer Research UK Manchester Institute, Alderley Park, Manchester SK10 4TG, UK
[2]Flow Cytometry Core, Cancer Research UK Manchester Institute, Alderley Park, Manchester SK10 4TG, UK
[3]Cancer Research UK Beatson Institute, Garscube Estate, Bearsden, Glasgow G61 1BD, UK
[4]University of Michigan, Rogel Cancer Center, University of Michigan, Ann Arbor, MI 48109, USA
[5]Department of Surgery, University of Michigan, Ann Arbor, MI 48109, USA
[6]Department of Cell and Developmental Biology, Ann Arbor, MI 48109, USA
[7]Molecular and Cellular Pathology Graduate Program, University of Michigan, Ann Arbor, MI 48109, USA
[8]Drug Discovery Unit, Cancer Research UK Manchester Institute, Alderley Park, Manchester SK10 4TG, UK
[9]Cell Signalling, Cancer Research UK Manchester Institute, Alderley Park, Manchester SK10 4TG, UK
[10]Molecular Oncology, Cancer Research UK Manchester Institute, Alderley Park, Manchester SK10 4TG, UK
[11]Department of Medical Oncology, The Christie NHS Foundation Trust, Wilmslow Road, Manchester M20 4BX, UK
[12]Institute of Cancer Sciences, University of Manchester, Wilmslow Road, Manchester M20 4BX, UK
[13]Institute of Cancer Sciences, University of Glasgow, Switchback Road, Garscube Estate, Glasgow G61 1QH, UK
[14]Cancer Immunity and Inflammation, Cancer Research UK Manchester Institute, Alderley Park, Manchester SK10 4TG, UK
[15]Lead contact
*Correspondence: claus.jorgensen@cruk.manchester.ac.uk
https://doi.org/10.1016/j.ccell.2021.06.017

SUMMARY

Fibroblasts display extensive transcriptional heterogeneity, yet functional annotation and characterization of their heterocellular relationships remains incomplete. Using mass cytometry, we chart the stromal composition of 18 murine tissues and 5 spontaneous tumor models, with an emphasis on mesenchymal phenotypes. This analysis reveals extensive stromal heterogeneity across tissues and tumors, and identifies coordinated relationships between mesenchymal and immune cell subsets in pancreatic ductal adenocarcinoma. Expression of CD105 demarks two stable and functionally distinct pancreatic fibroblast lineages, which are also identified in murine and human healthy tissues and tumors. Whereas CD105-positive pancreatic fibroblasts are permissive for tumor growth *in vivo*, CD105-negative fibroblasts are highly tumor suppressive. This restrictive effect is entirely dependent on functional adaptive immunity. Collectively, these results reveal two functionally distinct pancreatic fibroblast lineages and highlight the importance of mesenchymal and immune cell interactions in restricting tumor growth.

INTRODUCTION

Stromal fibroblasts are critical to normal tissue homeostasis but are functionally subverted in fibrotic, inflammatory, and neoplastic disease (Dakin et al., 2018; Driskell and Watt, 2015; Sahai et al., 2020). Coerced fibroblasts, and their heterocellular interactions, have therefore become attractive therapeutic targets in multiple disease indications (Dakin et al., 2018; Sahai et al., 2020). In particular, cancer-associated fibroblasts (CAFs) have been ascribed pleiotropic pro-tumorigenic functions, such as extracellular matrix remodeling and tissue stiffening, escape from immune surveillance, and promotion of therapeutic resistance (Feig et al., 2013; Hirata et al., 2015; Sahai et al., 2020). However, genetic and pharmacological ablation of fibroblasts in preclinical mouse models reduces survival, and a clinical trial broadly targeting fibroblasts in pancreatic cancer patients was terminated due to disease acceleration (NCT01130142) (Catenacci et al., 2015; Kim et al., 2014; Özdemir et al., 2014; Rhim et al., 2014). Consequently, functionally opposing fibroblast populations have been hypothesized to coexist in the tumor microenvironment (TME).

Cellular diversity arises from a combination of irreversible differentiation hierarchies (lineages) and distinct but plastic polarizations (states) (Croft et al., 2019; Janes, 2016; Tirosh et al., 2016; Wohlfahrt et al., 2019). For example, distinct lineages of spatially organized dermal fibroblasts arise during embryonic development and have discrete functions in adult skin

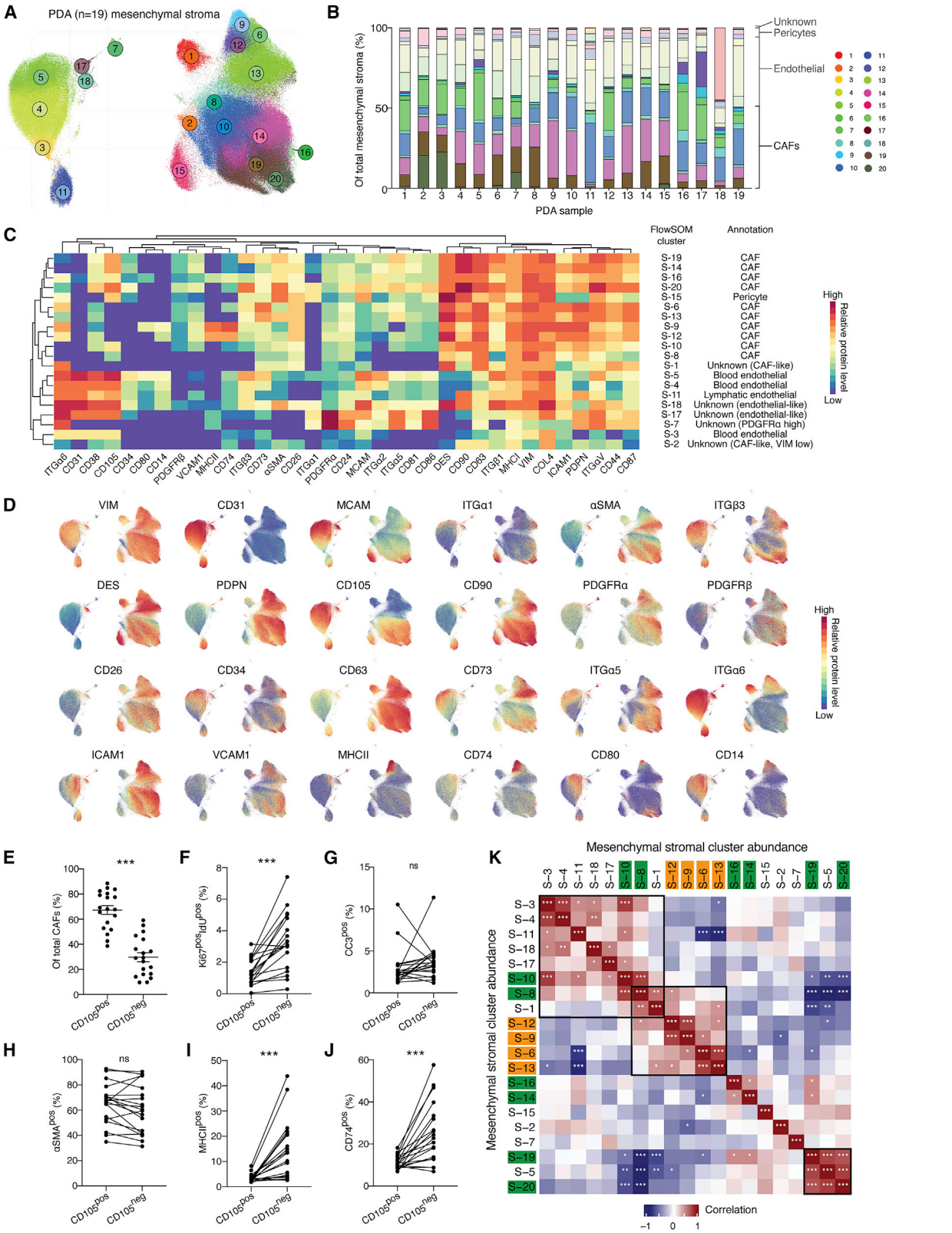

(legend on next page)

homeostasis and wound repair (Driskell et al., 2013; Rinkevich et al., 2015). However, whether functionally distinct fibroblast lineages exist in other mammalian tissues is not known. Moreover, fibroblasts have the capacity to adopt at least two phenotypically distinct states, with myofibroblastic or inflammatory characteristics (Biffi et al., 2019; Kuppe et al., 2020; Öhlund et al., 2017). Determining whether distinct fibroblast lineages and phenotypes are associated with specific pathologies is necessary for the efficient application of stromal-targeting therapies (Helms et al., 2020; Sahai et al., 2020).

Genetically engineered mouse models (GEMMs) have been instrumental in interrogating the TME. The *Pdx1-Cre;Kras$^{LSL\text{-}G12D/+}$;Trp53$^{LSL\text{-}R172H/+}$* (KPC) model of pancreatic ductal adenocarcinoma (PDA) recapitulates several aspects of the human disease, including genetic instability, therapeutic resistance, and an extensive desmoplastic microenvironment (Halbrook et al., 2019; Hingorani et al., 2005; Steele et al., 2016). Targeting specific pro-tumorigenic functions of fibroblasts in KPC tumors improves response to chemotherapy and sensitizes to immune checkpoint blockade (ICB) (Feig et al., 2013; Jiang et al., 2016; Miller et al., 2015; Shi et al., 2019). Similarly, targeting suppressive immune subsets also sensitizes to ICB and simultaneously alters desmoplasia, underscoring how mesenchymal and immune cell interactions balance pro- and anti-tumorigenic properties of the TME (Candido et al., 2018; Steele et al., 2016).

To chart mesenchymal and immune cell phenotypes in neoplastic disease, we immunophenotyped 14 million cells from 39 tumor samples, across 5 autochthonous murine models by mass cytometry (MC). In contrast to most CAF markers, CD105 demarks two discrete fibroblast populations in most normal and tumor-bearing tissues. The abundance of CD105^{pos} and CD105^{neg} CAFs correlate with distinct immune cell populations in PDA tumors, and diverge in their response to regulatory signals in the microenvironment. CD105^{pos} pancreatic fibroblasts are permissive for tumor growth *in vivo*. In contrast, CD105^{neg} fibroblasts potently restrict tumor growth, in a manner dependent on functional adaptive immunity and type 1 conventional dendritic cells (cDC1s).

RESULTS

Single-cell immunophenotyping of mesenchymal stromal cells

A practical barrier for characterizing fibroblast functions is a lack of robust cell surface markers for live cell isolation. We therefore assembled an MC antibody panel, emphasizing mesenchymal cell surface markers, for subsequent purification and characterization (Table S1). Established immune and epithelial cell lineage markers were included to aid annotation of non-mesenchymal lineages (Bendall and Nolan, 2012; Bendall et al., 2011). To ensure that bona fide mesenchymal cell populations were distinguishable from immune, endothelial, and tumor cells, including tumor cells having undergone epithelial to mesenchymal transition, we analyzed tumors from *Pdx1-Cre;Kras$^{LSL\text{-}G12D/+}$;Trp53$^{LSL\text{-}R172H/+}$;Rosa26$^{LSL\text{-}tdRFP/LSL\text{-}tdRFP}$* (RFP^{pos} KPC) mice. High-dimensional phenotypes were visualized using UMAP projections, demonstrating tumor cell (RFP^{pos} PCK^{high} EpCAM^{pos}) segregation from immune cells (CD45^{pos}), endothelial cells (ECs) (CD31^{pos}), and non-transformed mesenchymal stromal cells (RFP^{neg} CD45^{neg} CD31^{neg} CD90^{pos}), even when RFP was omitted from clustering (Figures S1A and S1B) (Becht et al., 2018; Van Gassen et al., 2015).

Phenotypic and compositional heterogeneity of pancreatic cancer-associated mesenchymal cells

To quantitatively annotate the composition of mesenchymal stromal cells in PDA, we analyzed 5 million cells from 19 tumors collected from KPC mice (Figures 1A–1D and S1C). Mesenchymal stromal cells constituted 12.6% ± 5.0% (mean ± standard deviation), CD45^{pos} immune cells 39.3% ± 14.7%, and tumor cells 47.8% ± 17.7% of all viable single cells.

Immune and tumor cells were excluded and the remaining cells were clustered using FlowSOM and visualized by UMAP projection (Figures 1A–1D and S1D). The mesenchymal subset composition varied extensively within and between tumors (Figures 1A–1D; Table S1). CD31^{pos} ECs comprised seven clusters, including three blood EC phenotypes (S-3, 4, and 5), one lymphatic EC cluster (S-11), and three other minor clusters (S-7, 17, and 18). Pericytes (S-15) form a single uniform and discrete cluster (Figures 1A–1D). Blood ECs (S-3, 4, and 5), form a continuum of phenotypes with graded abundance of MCAM, ITGβ3, and ITGα5 (Figures 1A–1D). Comparing EC subset abundances with macroscopic tumor features revealed an inverse relationship between the major blood EC cluster, S-4, and tumor weight (Figure S1E), suggesting that larger PDA tumors are not only poorly perfused due to vessel collapse, but also display insufficient vascularization (Olive et al., 2009; Provenzano et al., 2012).

The remaining clusters were designated as CAFs (8.2% ± 3.5% of all viable cells). PDPN, CD90, DES, and CD63 were

Figure 1. Phenotypic and compositional heterogeneity of pancreatic cancer-associated mesenchymal cells

(A) UMAP projection of single mesenchymal stromal cells from n = 19 tumors, with color-coded FlowSOM clusters (1–20). Total of 5 × 10^5 cell displayed.

(B) Stacked bar graph displaying relative abundance of KPC PDA mesenchymal stromal subclusters. Color coded as in (A) and separated into major mesenchymal groups.

(C) Heatmap of marker median mass intensities (MMIs) displayed as *Z* scores. Each FlowSOM cluster was grouped by unsupervised hierarchical clustering based on marker MMIs. Cell-type annotations based on canonical markers are listed.

(D) UMAP projection from (A) displaying overlaid signal intensity of selected phenotypic markers.

(E) Whisker plot with relative frequency of CD105^{pos} and CD105^{neg} CAFs displayed as mean ± SD. n = 19 KPC tumors.

(F–J) Relative frequency of S-phase (F), apoptotic (G), αSMA^{pos} (H), MHCII^{pos} (I) and CD74^{pos} (J) CAFs within total CD105^{pos} and CD105^{neg} CAFs. Paired populations from the same tumor samples are linked.

(K) Spearman correlation coefficients of all pairwise mesenchymal stroma cluster frequencies. CD105^{neg} (orange) and CD105^{pos} (green) CAF subsets highlighted.

Data are compared using paired t tests (E–J) or Spearman correlation adjusted for multiple testing using Benjamini-Hochberg correction (K). ns, not significant; *p < 0.05, **p < 0.01, ***p < 0.001.

See also Figure S1 and Table S1.

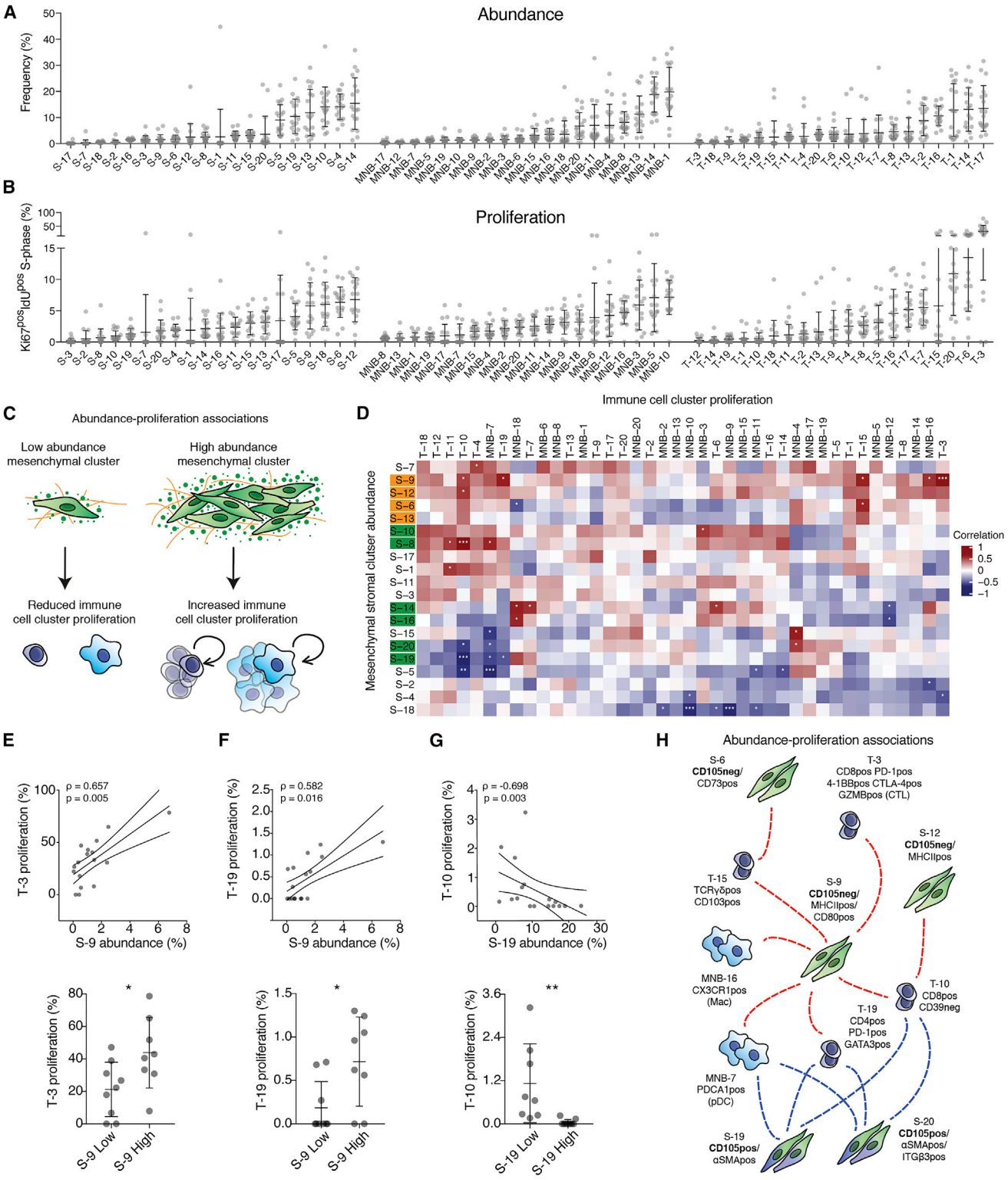

Figure 2. Co-regulated CAF and immune subsets within the PDA tumor microenvironment

(A and B) Relative frequency within parental population (A) and proliferative fraction ($Ki67^{pos}$ IdU^{pos}) (B) of annotated subsets. Data displayed as mean ± SD.

(C) Model of association between mesenchymal subset abundance and immune cell proliferation.

(D) Matrix of Spearman correlation coefficients of all pairwise mesenchymal subset frequencies and immune cell proliferation. $CD105^{neg}$ (orange) and $CD105^{pos}$ (green) CAF subsets highlighted.

(legend continued on next page)

abundant on most CAFs; however, these markers cannot be used in isolation to confidently identify all CAFs (Figures 1A–1D). Most markers, including αSMA, PDGFRα/β, MCAM, ICAM1, VCAM1, ITGα5, CD34, and CD73, displayed graded expression in several CAF clusters, revealing a spectrum of phenotypic states (Figures 1A–1D). For example, αSMA and PDGFRα displayed an inverse relationship across CAF subsets with αSMA^{high} clusters (S-19 and 20) and αSMA^{low}/PDGFRα^{high} clusters (S-6, 9, and 12) corresponding to myofibroblastic CAFs (myCAFs) and inflammatory CAFs (iCAFs), respectively (Biffi et al., 2019; Elyada et al., 2019). The dipeptidylpeptidase CD26, which demarks a distinct fibroblast lineage in the skin, displayed graded expression in PDA tumors, indicative of phenotypic states rather than a defined lineage (Driskell et al., 2013; Rinkevich et al., 2015). In contrast, the transforming growth factor β receptor (TGF-βR) co-receptor, CD105, clearly separated two distinct CAF populations in all 19 tumor samples analyzed (Figures 1A–1D). The CD105^{pos}:CD105^{neg} CAF ratio varied widely between different PDA tumors, where CD105^{pos} CAFs typically were more abundant (~7:3 ratio) (Figure 1E). However, CD105^{neg} CAFs were notably abundant in a minority of tumors. Moreover, CD105^{neg} CAFs were more proliferative in tumors, but did not display any differences in apoptotic rate (Figures 1F and 1G). Most markers, including αSMA and PDGFRα, displayed graded expression in both CD105^{pos} and CD105^{neg} CAFs, indicating that both populations can acquire myCAF and iCAF characteristics (Figures 1C and 1D) (Biffi et al., 2019; Kuppe et al., 2020; Öhlund et al., 2017). The extent of myofibroblast polarization for both CD105^{pos} and CD105^{neg} CAFs was highly variable (31.4%–92.3% of all CAFs) and exhibited remarkable co-variation between CAFs from the same tumor, indicative of highly coordinated regulation of the myCAF phenotype within each tumor (Figures 1H and S1F). Conversely, the laminin binding ITGα6, the lipopolysaccharide co-receptor, CD14, and several proteins involved in major histocompatibility complex class II (MHCII) antigen presentation (MHCII and CD74) were almost exclusive to CD105^{neg} CAFs (S-9 and 12), indicating that the majority of the recently described antigen-presenting CAF (apCAFs) fall within the CD105^{neg} CAF subset (Figures 1A–1D, 1I, and 1J) (Elyada et al., 2019). Re-analysis of available single-cell transcriptomic (scRNA-seq) data (Elyada et al., 2019) confirmed that differential *Eng* (CD105) expression separates two CAF populations, with myCAF and iCAF signature gene expression in both *Eng*^{pos} and *Eng*^{neg} clusters and apCAF gene expression restricted to the *Eng*^{neg} cluster (Figure S1G). Finally, correlation analysis of the relative abundances between mesenchymal subsets revealed distinct coordinated relationships within, but not between, most CD105^{pos} or CD105^{neg} subsets, suggesting that each population responds distinctly to regulatory signals within the TME (Figure 1K).

Co-regulated CAF and immune subsets within the PDA tumor microenvironment

In addition to fibrotic expansion, developing PDA is characterized by a co-evolving tumor-permissive inflammation (Clark et al., 2007; Collins et al., 2012). To reveal phenotypic relationships between mesenchymal and immune cell populations in PDA, we used MC to annotate and quantify CD45^{pos} CD3ε^{neg} (myeloid, natural killer, and B cell [MNB]) and CD45^{pos} CD3ε^{pos} (T cell) subsets (Figures S2A–S2H) in tumors that had already been annotated for mesenchymal stromal composition.

All major immune subsets were identified and quantified (Figures S2A–S2H; Table S2) (Bendall et al., 2011; Spitzer et al., 2017). Monocytes (MNB-6, 8, 12) and macrophages (MNB-11, 14–20) were notably abundant and phenotypically heterogeneous, with graded expression of T cell inhibitory checkpoint ligands and chemotactic receptors (Figures S2A–S2D) (Di Mitri et al., 2019). In contrast, CD45^{pos} CD3ε^{pos} T cells constituted only 4.0% ± 3.9% of all viable cells. CD4^{pos} T cells were predominantly FOXP3^{pos} T regulatory cells (Figures S2E–S2H). The majority of all CD8^{pos} T cells (75.7% ± 23.4%) in these tumors were PD-1^{neg} CD39^{neg} bystanders, where only three minor CD8^{pos} T cell subsets (T-3, 4, and 6) expressed markers indicative of T cell receptor engagement (Figures S2E–S2H) (Simoni et al., 2018). T-4 (PD-1^{high} CD39^{high} CD38^{high}) resemble the "terminally exhausted" phenotype, with a lack of GZMB expression, high EOMES, and reduced effector function (Simoni et al., 2018; Thommen et al., 2018). T-3 (PD-1^{int} CD39^{pos} CD38^{neg} GZMB^{pos} CTLA-4^{pos} 4-1BB^{pos} T-BET^{pos}) is phenotypically consistent with an active but not terminally exhausted phenotype and has been associated with improved capacity for expansion and tumor control (Leun et al., 2020; Philip et al., 2017). T-6 is the only CD8^{pos} PD-1^{pos} subset to express the transcription factor TCF-1, associated with stem/progenitor-like functions and high expansion potential during immunotherapy (Leun et al., 2020; Yost et al., 2019).

Annotation of the relative subset abundance, the proliferating cell fraction (%Ki67^{pos} IdU^{pos} cells), and apoptotic cell fraction (%CC3^{pos} cells) revealed extensive variability of all stromal subsets between tumors (Figures 2A, 2B, and S3A; Table S2). For example, T cell subsets display striking variation in proliferation rates, where the CD8^{pos} T cell subset, T-3, was highly proliferative only in some tumors (mean 33.8% ± 20.4%) (Figure 2B). Notably, three of the most proliferative mesenchymal subsets were all CD105^{neg} CAFs, including the MHCII^{pos} CD74^{pos} S-9 and S-12.

To find potential heterocellular relationships, we leveraged the inherent variability between these spontaneous tumors and correlated the abundance, proliferation, and apoptotic fractions of stromal subsets in a pairwise manner (Figures S3B and S3C; Table S2) (Chevrier et al., 2017; Jackson et al., 2020). The abundance of specific mesenchymal subsets correlated with the

(E–G) Spearman correlation analysis of S-9 (E, F) and S-19 (G) relative frequency with proliferative fraction of T-3 (E), T-19 (F), and T-10 (G) (top). ρ = Spearman correlation coefficient, 90% confidence intervals displayed. PDA tumors split into high (n = 7) or low (n = 8) fractions of S-9 (E and F) and S-19 (G) with proliferative fraction of T-3 (E), T-19 (F), and T-10 (G) displayed as mean ± SD (bottom).

(H) Model of positive (red) and negative (blue) correlations of CD105^{pos} and CD105^{neg} CAF subset abundance and proliferation of selected immune subsets.

Samples were compared using unpaired t tests (E–G) (bottom) or Spearman correlation adjusted for multiple testing using Benjamini-Hochberg correction (D, E–G) (top). ns, not significant; *p < 0.05, **p < 0.01, ***p < 0.001.

See also Figures S2 and S3 and Table S2.

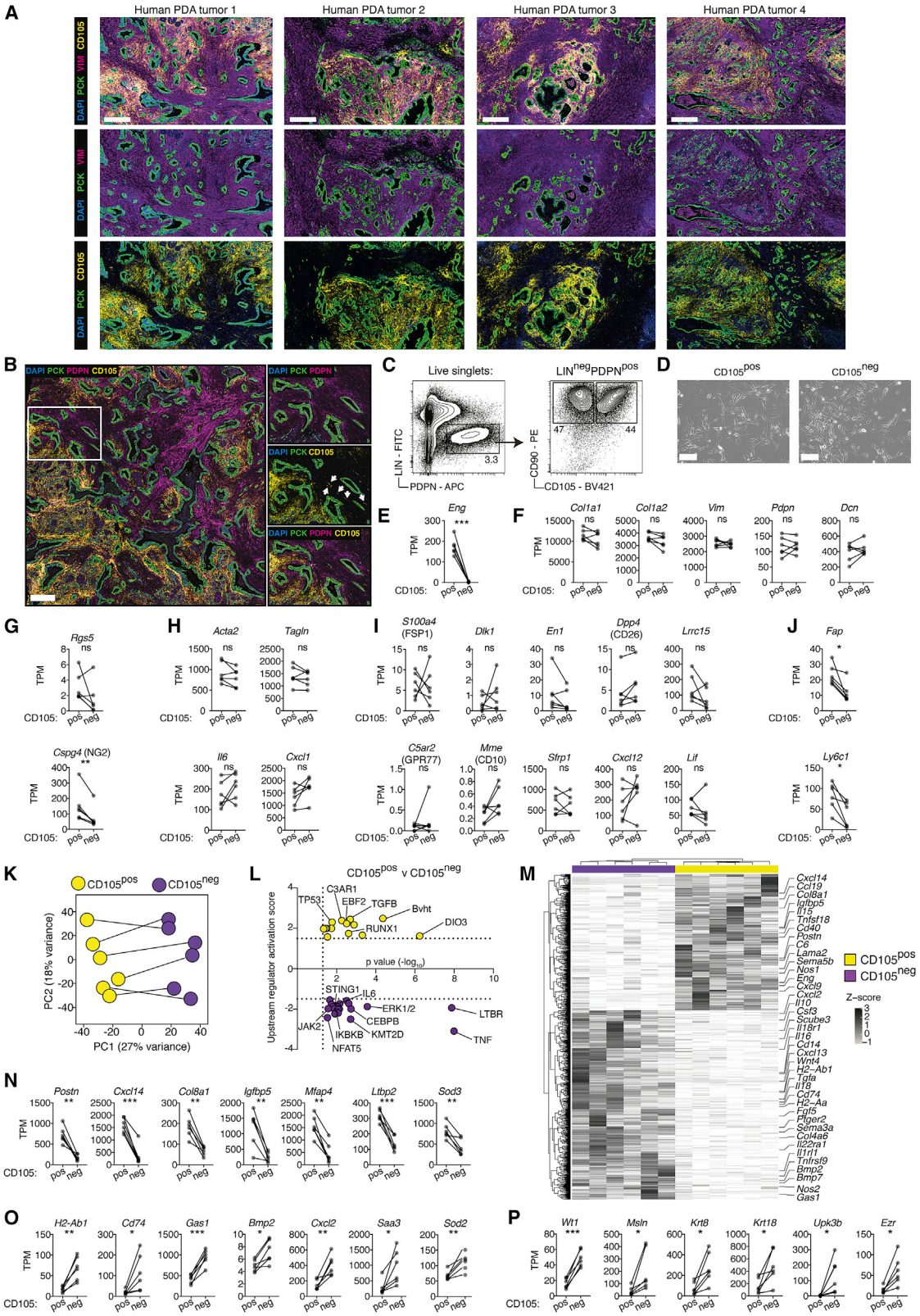

(legend on next page)

proliferation rate of several immune subsets, reflecting possible directional interactions (Figures 2C–2G). For example, the abundance of mesenchymal subset S-9 (CD105^{neg} MHCII^{pos} CD74^{pos}) was positively correlated with the proliferation of several T cell subsets, including the antigen-experienced CD4 T cell subset (T-19) and the CD8^{pos} CD39^{neg} T-10 subset (Figures 2E–2G). Moreover, S-9 was the only mesenchymal subset positively associated with increased proliferation of the antigen experienced, but not terminally exhausted, T-3 subset (Figures 2D and 2E). In contrast, the CD105^{pos} αSMA^{high} CAF subsets (S-19 and 20) were anti-correlated with the proliferation of T-19 and 10 (Figures 2D and 2G). Markedly, some CD105^{pos} and CD105^{neg} mesenchymal subsets displayed opposing relationships with several immune subsets, suggestive of contrasting immune-modulatory effects (Figures 2D and 2H).

CD105 expression discriminates two distinct CAF populations in murine and human PDA

To determine whether CD105^{pos} and CD105^{neg} CAFs were also present in human PDA, we co-stained human resected samples for pan-cytokeratin (PCK) to mark epithelial cells, VIM or PDPN to mark CAFs and CD105. Both CD105^{pos} and CD105^{neg} CAFs were clearly identified and regionally distributed in the stroma, demonstrating that these CAF populations are preserved in human disease (Figures 3A and 3B; Table S3).

To establish if CD105^{pos} and CD105^{neg} CAFs are phenotypically distinct, we used the MC data to design a fluorescence-activated cell sorting (FACS) gating strategy and collected paired CD105^{pos} and CD105^{neg} CAFs from six KPC PDA tumors for gene expression analysis (Figures 3C–3P and S4A). In agreement with the MC analysis (Figure 1F), the relative abundance of CD105^{pos} and CD105^{neg} CAFs varied extensively between samples, and plated cells exhibited mesenchymal morphology (Figures 3D and S4A). Genes associated with general fibroblast identity, such as *Col1a1*, *Col1a2*, *Vim*, *Pdpn*, and *Dcn*, were expressed at equal levels in both the CD105^{pos} and CD105^{neg} populations and neither population had significantly different expression of the pericyte-associated gene *Rgs5*, however, CD105^{pos} CAFs have higher *Cspg4* expression (Figures 3E–3G). Genes associated with myCAF and iCAF identity as well as genes previously reported to define heterogeneous fibroblast populations, such as *S100a4* (FSP1), *Dpp4* (CD26), *Dlk1*, *En1*, *Lrcc15*, *C5ar2* (GPR77), *Mme* (CD10), Sfrp1, *Cxcl12*, and *Lif*, were all equally expressed between CD105^{pos} and CD105^{neg} CAFs (Figures 3H and 3I) (Dominguez et al., 2020; Driskell et al., 2013; Feig et al., 2013; Lichtenberger et al., 2016; Rinkevich et al., 2015; Su et al., 2018). Expression of *Fap* and *Ly6c1*, which have previously been used for isolation of CAF populations, were enriched in CD105^{pos} CAFs (Elyada et al., 2019; Feig et al., 2013). However, CD105^{neg} CAFs variably express some level of these genes *in vivo* (Figure 3J).

Principal-component (PC) analysis of differentially expressed genes (DEGs) confirmed the major variance across samples (PC1) was related to CD105 status, suggesting that consistent differences in CD105^{pos} and CD105^{neg} CAF gene expression are conserved across tumors (Figure 3K). Ingenuity Pathway Analysis (IPA) highlighted several differentially engaged upstream regulators and pathways, with TGF-β signaling enriched in CD105^{pos} CAFs, and LTBR, tumor necrosis factor alpha (TNF-α), nuclear factor κB (NF-κB), interleukin-6 (IL-6), JAK2, and STING1 signaling enriched in CD105^{neg} CAFs (Figures 3L and S4B). A large number of genes encoding secreted products with known functional relevance in the TME were differentially expressed (Figures 3M–3O). For example, *Postn*, *Cxcl14*, and *Igfbp5* were increased in CD105^{pos} CAFs, and *Cxcl2*, *Gas1*, *Bmp2*, and *Nos2* were elevated in CD105^{neg} CAFs, which was also confirmed by re-analysis of available KPC scRNA-seq data (Figures 3M–3O, S4C, and S4D) (Elyada et al., 2019). Notably, single-cell *Eng* mRNA levels appear lower in iCAF-polarized CD105^{pos} cells, which makes accurate annotation of CD105 status by single-cell mRNA levels alone challenging (Figures S4C and S1G). As expected, genes involved in MHCII antigen presentation were predominantly expressed in CD105^{neg} CAFs, confirming an overlap between apCAFs and CD105^{neg} CAFs (Figures 3O and S4D). Moreover, CD105^{neg} CAFs express higher levels of several genes associated with mesothelial cell identity, including *Wt1*, *Msln*, *Krt8/18*, *Upk3b*, and *Ezr*, although the expression was non-uniform and restricted to a sub-fraction of *Eng*^{neg} cells (Figures 3P and S4D). Analysis of scRNA-seq data from human PDA tumors and normal adjacent tissue confirmed the presence of distinct *ENG*^{pos} and *ENG*^{neg} populations with expected distribution of CD105^{pos} and CD105^{neg} signature genes (Figures S4E–S4G) (Steele et al., 2020). Notably, myCAF and iCAF signature genes were also expressed across both *ENG*^{pos}

Figure 3. CD105 expression discriminates two distinct CAF populations in murine and human PDA

(A and B) Immunohistochemistry (IHC) of human PDA tumor samples stained for pan-cytokeratin (PCK) (green), CD105 (yellow), DAPI (blue) and vimentin (VIM) (A) or podoplanin (PDPN) (B) (purple). Insert is magnified with arrows annotating vessels (right) (B). Representative images of n = 15 tumor samples. Scale bar = 500 μm..

(C and D) Fluorescence-activated cell sorting plots (C) and *in vitro* cultures (D) of CD105^{pos} and CD105^{neg} CAFs. Representative of n = 6 independent experiments. Scale bar, 150 μm.

(E–J) RNA-seq expression analysis of paired CD105^{pos} (n = 6) and CD105^{neg} (n = 6) PDA CAFs. Isolations from the same tumor sample are linked. Gene expression calculated as transcripts per kilobase million (TPM). Displaying *Eng* (the gene encoding CD105) (E), canonical fibroblast genes (F), canonical pericyte genes (G), myCAF- and iCAF-associated genes (H), and genes associated with fibroblast heterogeneity in other studies (I–J).

(K) Principal-component (PC) analysis of differentially expressed genes between CD105^{pos} (n = 6, yellow) and CD105^{neg} (n = 6, purple) PDA CAFs. DEGs determined using DEseq2 as >2 fold-change and Benjamini-Hochberg adjusted $p < 0.05$. Paired CAFs from the same tumor are linked.

(L) Ingenuity Pathway Analysis of CD105^{pos} (Yellow) and CD105^{neg} (purple) CAF DEGs, displaying upstream activators.

(M) Heatmap of expression levels of all 1007 CAF DEGs, displayed as row *Z* scores. Example DEGs are highlighted.

(N–P) CD105^{pos} PDA CAF DEGs (N), CD105^{neg} PDA CAF DEGs (O), and CD105^{neg} CAF DEGs associated with mesothelial cell identity (P). Gene expression calculated as TPM. Isolations from the same tumor sample are linked.

Samples are compared using paired t tests (D–I and M–O). ns, not significant; *$p < 0.05$, **$p < 0.01$, ***$p < 0.001$.

See also Figure S4 and Table S3.

and *ENG*^{neg} clusters in human PDA (Figure S4G). Collectively, this demonstrates the presence of CD105^{pos} and CD105^{neg} CAFs in human PDA and highlights their potential to differentially respond to and modify the inflammatory TME.

Phenotypic plasticity of mesenchymal marker expression

We hypothesized that lineage-restricted fibroblast subsets would be defined by distinct and stable marker expression, whereas graded marker expression likely reflects cellular plasticity (Figures 1A–1D). Since CAFs are tumor educated, we reasoned that fibroblasts from the normal tissue would reveal intrinsic differences in fibroblast hierarchies and therefore examined whether CD105 expression is stable or dynamically regulated in naive fibroblasts. Pancreatic fibroblasts (PaFs) were expanded from healthy tissue, revealing CD105^{pos} and CD105^{neg} PaF populations, which could be purified by FACS and cultured (Figure S5A). PaFs remained CD105^{pos} or CD105^{neg} after extended passaging and were able to generate stable cell lines (Figure 4A). Moreover, CD105 remained differentially expressed after treatment with tumor cell-conditioned medium, by direct tumor cell co-culture, or following extended culture with fibroblast-modulating signals TGF-β1, IL-1α, and interferon gamma (IFN-γ) (Figures 4B, 4C, and S5B). CD105 expression also distinguished two separate and stable populations in isolated human PaFs, and demarked two distinct fibroblast populations in non-tumor-bearing tissue adjacent to PDA (Figures 4D and S5C). Interestingly, CD105^{pos} and CD105^{neg} PaFs were discretely localized in the inflamed pancreas, with CD105^{pos} PaFs observed in the intra-acinar regions of the pancreas and the CD105^{neg} PaFs in the inter-acinar regions (Figure S5C). Finally, scRNA-seq analysis of *in-vitro*-expanded primary murine PaFs 7 days after isolation, confirmed that *Eng* expression defines the two major cell clusters, with expected expression of signature genes (Figures S5A, S5D–S5K). *Eng* transcripts were incompletely detected by scRNA-seq in clusters that have robust CD105 protein expression by flow cytometry (Figures S5A and S5I). Clustering was further divided by proliferation-associated genes (Figure S5K), indicating that differential *Eng*/CD105 expression captured the major source of heterogeneity in PaFs. Thus, CD105 is a key cell surface discriminator of two distinct human and murine PaF lineages.

To subsequently determine how individual stimulations regulate marker expression in an unbiased, but experimentally controlled manner, we treated freshly isolated PaFs with 17 individual fibroblast-modulating signals for 72 h and analyzed marker expression by MC (Figures 4E–4H; Table S4). Importantly, distinct PaF populations remained clearly separated by bimodal CD105 expression across all stimulations (Figures 4E and 4F). Moreover, the relative abundance of CD105^{pos} and CD105^{neg} PaFs remained consistent across most of the 17 treatments, except for TGF-β1, which increased the fraction of CD105^{pos} PaFs, and TNF-α and IFN-γ, which increased the relative abundance CD105^{neg} PaFs (Figures 4E and 4F).

Hierarchical clustering of normalized median marker intensities revealed a diverse range of responses across both CD105^{pos} and CD105^{neg} populations, illustrating a high degree of phenotypic plasticity in both PaF populations (Figures 4G and 4H). Compared with the MC analysis of KPC tumors (Figures 1A–1D), markers with both broad and graded expression were dynamically regulated by individual signals, indicating that fibroblast surface marker abundance, in most cases, reflects dynamic changes in the local signaling environment. Some signals, such as TNF-α, IL-1α, and IL-1β, decrease αSMA and MCAM and increase PDGFRα and VCAM1 levels in both CD105^{pos} and CD105^{neg} populations, as expected. However, several other stimulations differentially regulate marker levels in CD105^{pos} and CD105^{neg} PaFs (Figures 4G and 4H). IFN-γ treatment increases MHCII, CD74, and CD80 in both CD105^{pos} and CD105^{neg} PaFs, which was verified using orthogonal flow cytometry (Figures 4I and 4J). In addition, this interferon-induced MHCII^{pos} fibroblast phenotype is inhibited in both CD105^{pos} and CD105^{neg} PaFs by simultaneous treatment with TGF-β1 or tumor cell-conditioned medium, suggesting that local signal integration shapes fibroblast phenotypes *in vivo* (Figures 4I and 4J). Finally, direct co-cultures of PaFs and pancreatic cancer cells induced a unique fibroblast marker signature, with elevated proliferation and expression of CD86 and CD90 (Figures 4G and 4H). This supports the notion that heterocellular interactions impose unique fibroblast phenotypes (Tape et al., 2016; Wei et al., 2020). Together, these results demonstrate that CD105 expression remains restricted and stable in isolated PaFs and therefore denote fibroblast lineages, whereas other tested markers are dynamically regulated and reflect fibroblast phenotypic plasticity.

Differential signaling engagement of CD105^{pos} and CD105^{neg} PaFs

To determine whether CD105^{pos} and CD105^{neg} PaFs also exhibit differences in their engagement of signaling networks, we analyzed selected signaling nodes in stimulated PaFs by MC (Figure 5A; Table S5). Strikingly, CD105^{pos} and CD105^{neg} PaFs exhibited distinct signaling responses even under controlled *in vitro* conditions. For example, IL-1α and IL-1β, engage NF-κB signaling more prominently in CD105^{pos} PaFs; and leukemia inhibitory factor (LIF), as well as IL-6, which both engage the common gp130 co-receptor, have distinct effects on signaling across PaF populations, with greater STAT3 phosphorylation in CD105^{pos} PaFs. This suggests that the two populations are intrinsically constrained in their signaling response.

We subsequently compared early gene expression changes after short 6 h TGF-β1, IL-1α, or IFN-γ treatment (Figures 5B–5D; Table S5) to determine whether observed differences in cellular signaling response is reflected in gene expression. This analysis highlighted a selective engagement of early transcriptional networks, where CD105^{pos} PaFs exhibited a significantly increased number of DEGs after stimulation with both TGF-β1 and IL-1α (Figures 5B and 5C). Although CD105 protein has no reported signaling capacity by itself, the receptor has been demonstrated to modulate the affinity of TGF-β family ligands to the TGF-βR signaling complex (Valluru et al., 2011). To test the role of CD105 in mediating TGF-β signaling, we used CRISPR-Cas-9 to delete *Eng* in CD105^{pos} PaFs (Figure S6A). Loss of CD105 dampened the early transcriptional response to TGF-β1 compared with parental CD105^{pos} PaFs, with a reduction from 151 DEGs in parental CD105^{pos} PaFs to 76 DEGs in CD105^{KO} PaFs (Figure 5B). In addition, the key TGF-β signaling mediator, *Smad3* is more highly expressed in CD105^{pos} PaFs

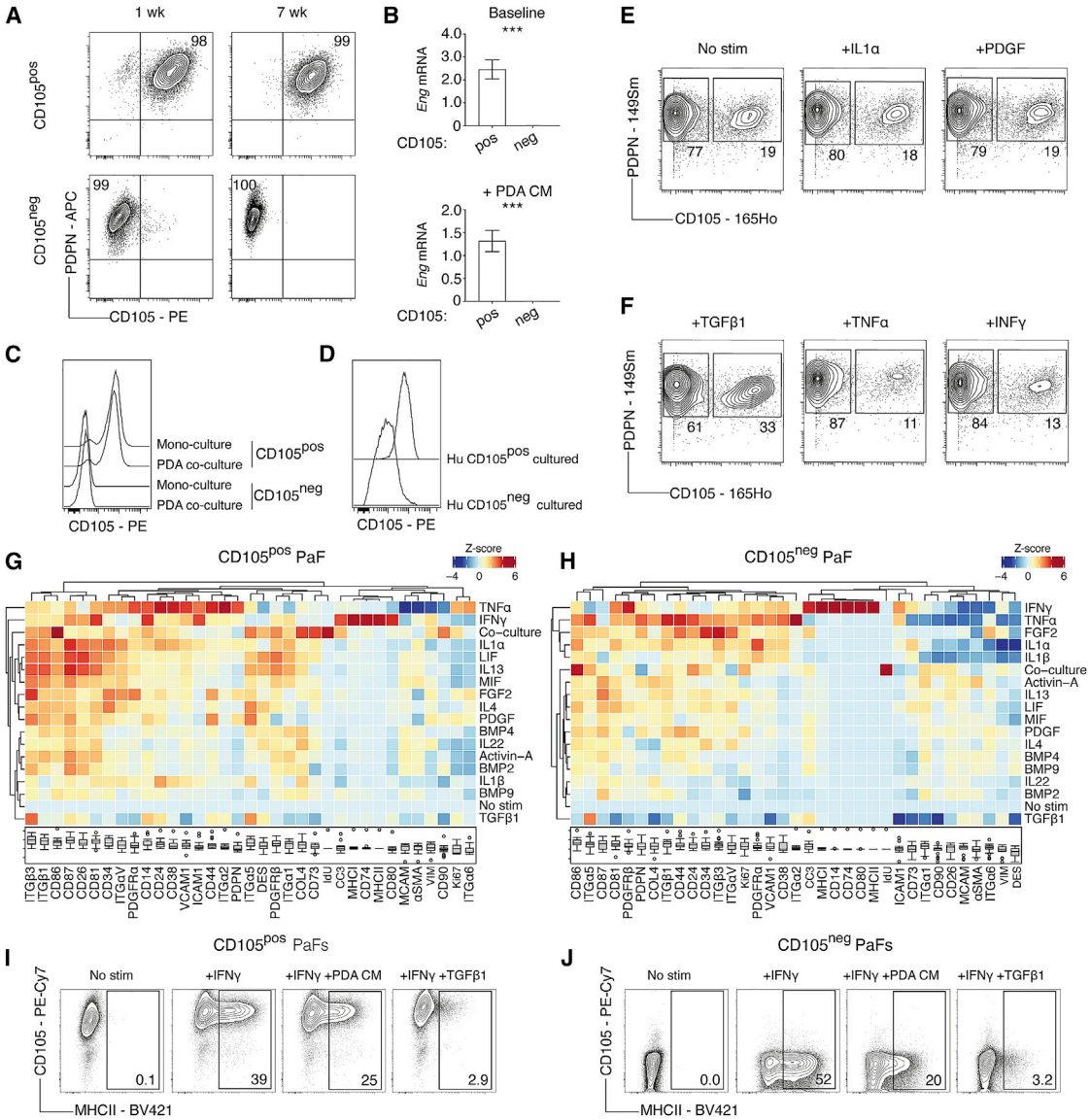

Figure 4. Phenotypic plasticity of mesenchymal marker expression

(A) Flow cytometry analysis of PDPN and CD105 in purified and *in-vitro*-cultured CD105^{pos} and CD105^{neg} pancreatic fibroblasts (PaFs) after 1 and 7 weeks. Plots are representative of n = 4 experiments. Relative frequencies shown in relevant quadrants.

(B) Normalized *Eng* mRNA expression in purified CD105^{pos} (n = 4) and CD105^{neg} PaFs (n = 4) treated with control (top) or KPC PDA conditioned medium (bottom). Data displayed as mean ± SD.

(C) Representative flow cytometry analysis (n = 4) of CD105 on GFP^{pos}CD105^{pos} and GFP^{pos}CD105^{neg} PaFs in mono- or co-culture with RFP^{pos} KPC PDA tumor cells.

(D) Representative flow cytometry analysis (n = 3) of CD105 in isolated CD105^{pos} and CD105^{neg} human PaFs after >3 weeks of *in vitro* culture.

(E and F) MC analysis of primary PaFs treated with the indicated ligands for 3 days. Representative plots displaying relative frequencies of CD105^{pos} and CD105^{neg} PaFs.

(G and H) Heatmap of median marker intensity (MMI) displayed as column *Z* scores for each phenotypic marker on CD105^{pos} (G) and CD105^{neg} (H) PaFs after 3 days of treatment as indicated. Boxplots show MMI with upper and lower boundary of the interquartile range and whiskers denoting maximum and minimum values minus outliers, across all conditions.

(I and J) Representative flow cytometry analysis (n = 3) of CD105^{pos} (I) and CD105^{neg} (J) PaFs with IFN-γ, IFN-γ + KPC PDA conditioned medium, or IFN-γ + TGF-β1 treatment.

Samples are compared using unpaired t tests (B) (top and bottom). ns, not significant; *p < 0.05, **p < 0.01, ***p < 0.001.

See also Figure S5 and Table S4.

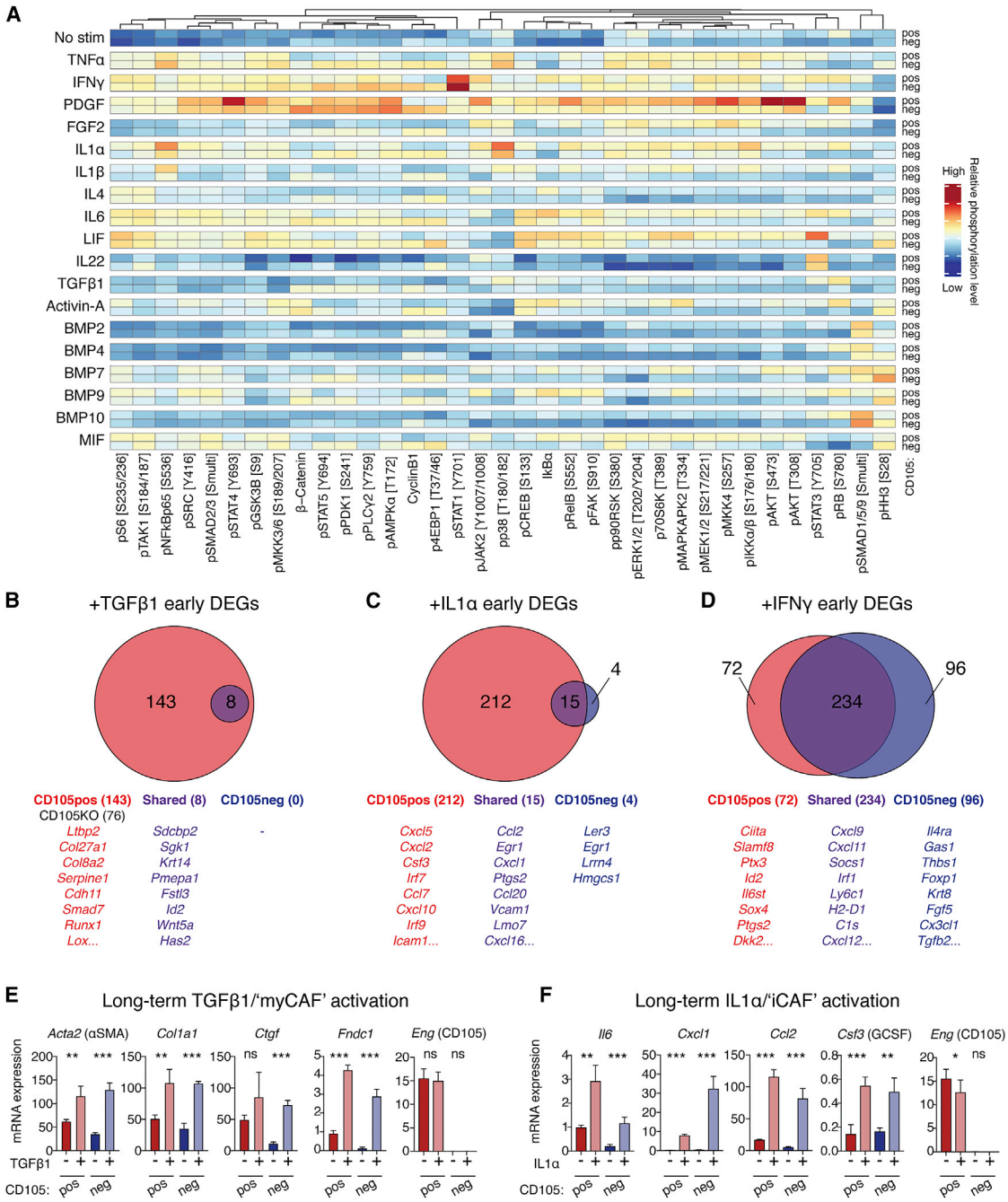

Figure 5. Differential signaling engagement of CD105^{pos} and CD105^{neg} PaFs

(A) MC analysis of CD105^{pos} and CD105^{neg} PaFs signaling. Data are displayed as median mass intensities (MMI) and column *Z* scores. Specific phosphorylation sites are annotated in brackets.

(B–D) RNA-seq analysis of CD105^{pos} and CD105^{neg} PaFs stimulated as displayed for 6 h (n = 3). DEGs were identified using DEseq2 with Benjamini-Hochberg adjusted $p < 0.05$. Data are displayed as Venn diagrams (top), with example genes listed (below). Unique DEGs of CD105^{pos} PaFs in red, CD105^{neg} PaFs in blue, and shared in purple. Numbers of significant DEGs are displayed in parenthesis.

(E and F) Expression of myCAF (E) and iCAF (F) genes from CD105^{pos} and CD105^{neg} PaFs stimulated with TGF-β1 or IL-1α (n = 4) for 3 days. *Eng* expression is also shown. Data displayed as mean ± SD.

Samples were compared using unpaired t tests (E and F). ns, not significant; *$p < 0.05$, **$p < 0.01$, ***$p < 0.001$.

See also Figure S6 and Table S5.

(Figure S6B). Curiously, the expression of several mesothelial-associated genes (e.g., *Msln* and *Upk3b*) are increased in CD105^{pos} PaFs when CD105 is deleted, demonstrating that CD105 itself suppresses a mesothelial-associated gene program in fibroblasts (Figure S6C). Moreover, both of the IL-1 receptors, *Il1r1* and *Il1rp*, as well as the key signaling mediator, *Myd88*, were more highly expressed in CD105^{pos} PaFs, which may underlie increased IL-1 sensitivity at this early time point (Figure S6B). Furthermore, *Il6st* (Gp130) is more abundant in CD105^{pos} PaFs, providing a possible explanation for the increased sensitivity to LIF and IL-6 (Figures 5A and S6B). The response to IFN-γ was more equal and the majority of IFN-γ early DEGs (234 genes) were shared between the CD105^{pos} and CD105^{neg} PaFs, including well established IFN-γ response genes, such as *Irf1*. However, both populations have a number of unique DEGs, indicative of a largely similar "core" IFN-γ response, with some population-specific differences.

As the MC and *ex vivo* gene expression analysis indicated that both CD105^{pos} and CD105^{neg} CAFs adopt myCAF and iCAF phenotypes *in vivo* (Figures 1C, 1D, and 3H), we treated CD105^{pos} and CD105^{neg} PaFs with TGF-β1 or IL-1α for an extended period (72 h) and analyzed gene expression by qPCR (Figures 5E and 5F). In agreement with the MC analysis, prolonged stimulation induced myCAF and iCAF phenotypes in both CD105^{pos} and CD105^{neg} PaFs. Differential *Eng* expression was retained across all conditions although CD105^{pos} PaFs that are iCAF-polarized have reduced *Eng* mRNA levels (Figures 5E and 5F). Thus, CD105^{pos} and CD105^{neg} PaFs appear to have different sensitivity to TGF-β1 and IL-1α activation at early time points (which may be more relevant when ligand abundance is limited) but both populations have the capacity to adopt both myCAF and iCAF phenotypes under extended stimulation (which may be more reflective of the extended activation that occurs in tumors).

CD105^{neg} fibroblasts restrict tumor growth *in vivo*

To determine whether CD105^{pos} and CD105^{neg} fibroblasts differentially influence tumor growth *in vivo* we established a subcutaneous co-injection model, reasoning that possible confounding effects from resident PaFs would be bypassed in this simplified model. Indeed, tumors formed by injecting an established KPC PDA tumor cell line alone exhibit low-level infiltration of host fibroblasts at early time points (Figure S7A). Moreover, when KPC PDA tumor cells were mixed with an equal number of GFP-labeled PaFs and injected subcutaneously, GFP^{pos} PaFs were retained after transplantation and exhibit stable differential CD105 expression (Figures 6A, S7B, and S7C).

Compared with control PDA tumor cells, co-injected CD105^{pos} PaFs did not significantly influence tumor volume at endpoint (Figure 6B). However, co-injection of CD105^{neg} PaFs dramatically restricts tumor growth and improves survival (Figures 6B and 6C), with 40% of mice exhibiting complete macroscopic and histological tumor regressions. Mixing CD105^{pos} and CD105^{neg} fibroblasts at a 1:1 ratio, but maintaining a constant total number of fibroblasts, also suppressed tumor growth; however, no full regressions were observed (Figure 6B). These findings are consistent across multiple independent studies and are reproduced with a second PDA tumor cell line and PaF lines with no GFP expression (Figures S7D–S7F). Thus, these results demonstrate that CD105^{pos} PaFs are permissive to tumor growth, whereas CD105^{neg} fibroblasts are highly tumor restrictive and that, in 1:1 mixtures of fibroblasts, the suppressive effect is dominant.

Co-injection of PDA tumor cells with CD105^{pos} or CD105^{neg} PaFs in NOD-*scid.Il2rg*$^{-/-}$ (deficient in innate and adaptive immune functions) or in *Rag1*$^{-/-}$ mice (deficient in mature T and B cells), did not affect tumor growth compared with mono-transplanted PDA tumor cells (Figures 6D and 6E). In addition, the restrictive effect of CD105^{neg} on tumor growth was highly blunted in *Baft3*$^{-/-}$ animals, which lack cDC1s (Figure 6F). Thus, the growth-suppressive effect of CD105^{neg} PaFs *in vivo* entirely depends on functional adaptive immunity, with a major contribution from cDC1s.

Since CD105^{neg} CAFs are almost unique in expression of MHCII antigen presentation machinery *in vivo* (Figures 1D, 1I, 1J, and 3O), and can be induced to express these *in vitro* (Figures 4G–4J), we sought to explore whether MHCII, CD74, and CD80 were required for the *in vivo* tumor-suppressive effect of CD105^{neg} PaFs. We disrupted the expression of these genes in CD105^{neg} PaFs using CRISPR-Cas-9 (Figures S7G and S7H) and investigated the ensuing effect *in vivo* (Figure 6G). However, co-implanted CD105^{neg} PaFs retained their restrictive capacity across all conditions. Thus, fibroblast MHCII antigen presentation is not required for the tumor-suppressive effect. To determine whether CD105 expression actively represses the tumor-restrictive phenotype, we co-implanted PDA tumor cells and CD105^{pos} PaFs disrupted for CD105 expression (CD105^{KO}) (Figure S6A). Injected CD105^{KO} fibroblasts did not differentially affect tumor growth compared with non-targeting gRNA-transfected CD105^{pos} PaFs (Figure S7I). Thus, CD105 is a useful marker of distinct fibroblast lineages but does not functionally contribute to the divergent tumor growth *in vivo.*

To investigate how co-injected CD105^{pos} and CD105^{neg} PaFs modulate the tumor microenvironment, we isolated developing tumors of similar size 10 days after injection and analyzed bulk gene expression profiles (Figures 6H–6J; Table S6). Consistent with loss of tumor suppression in animals with adaptive immunity deficiencies (Figures 6D–6F), we observed divergent engagement of immune-suppressive and immune-stimulatory transcriptional programs in CD105^{pos} and CD105^{neg} co-implanted tumors (Figures 6H–6J). DEG analysis highlighted increased expression of transcripts in CD105^{neg} co-injected tumors that are associated with T cell infiltration (*Cd3d*, *Lck*, *Zap70*, *Il2rb*, *Cd96*), effector CD8 T cells/Th1 CD4 T cells/innate lymphocytes (*Tbx21*), T cell memory precursor differentiation (*Il7r*), cDC1 (*Batf3*), and general DC (*Itgax*) infiltration, and antigen presentation (*H2-DMb1*, *H2-DMa*, *Cd74*) (Figure 6H). Furthermore, IPA revealed engagement of pathways and upstream regulators with established roles in productive anti-tumor immune responses, such as DC maturation, T cell activation, IFN-γ signaling, and innate lymphoid signaling, in CD105^{neg} PaF co-transplants (Figures 6I–6J) and MCPcounter analysis indicated an enrichment for DCs and CD8 T cells (Figure S7J) (Becht et al., 2016). Thus, these data support a role for CD105^{neg} PaFs in establishing a tumor-suppressive inflammatory reaction.

CD105^{pos} and CD105^{neg} fibroblasts are identified in normal and tumor-bearing tissues

To expand the analysis of stromal fibroblasts beyond PDA and the pancreas, we analyzed low passage, primary fibroblast

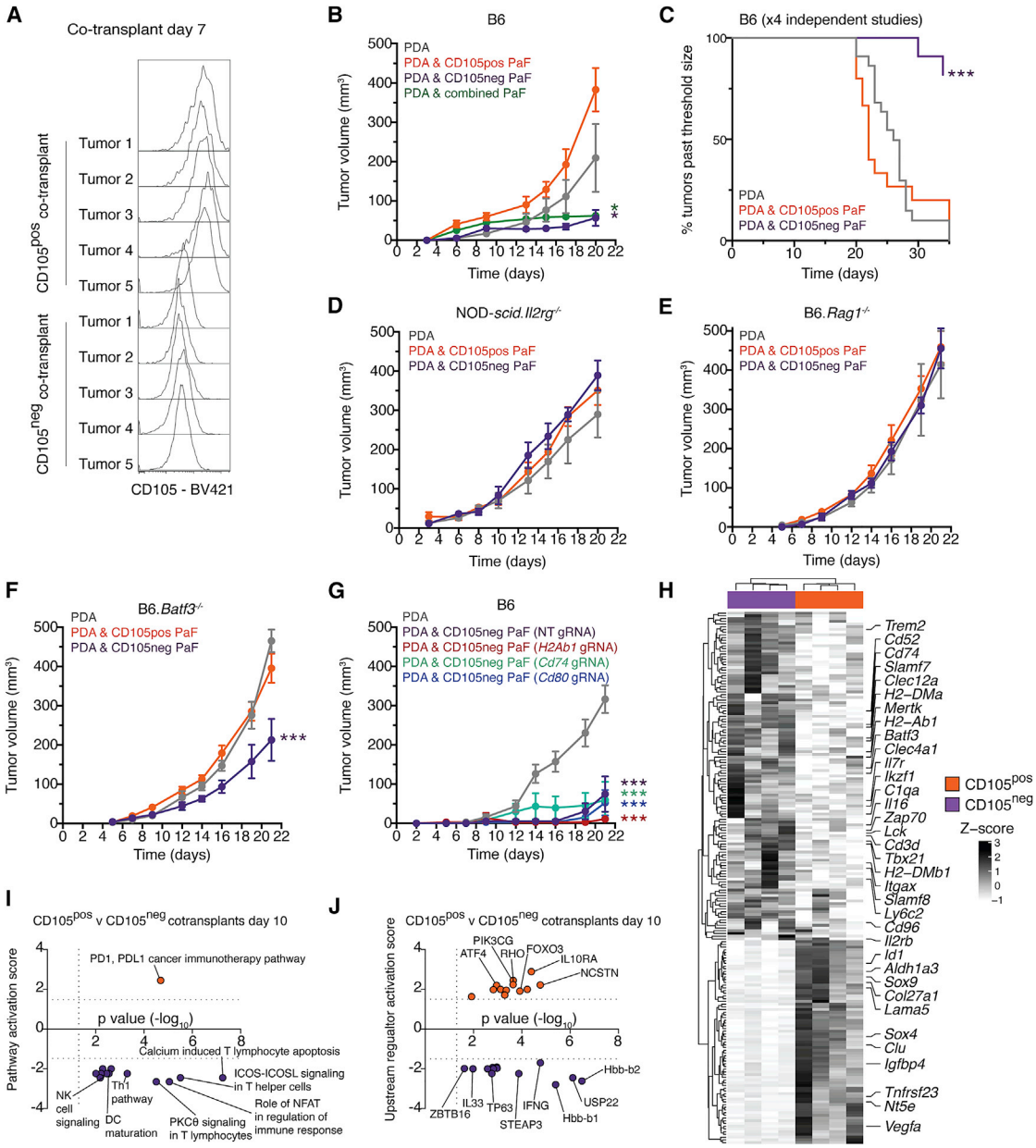

Figure 6. CD105^{neg} fibroblasts restrict tumor growth *in vivo*

(A) Flow cytometry analysis of co-implanted GFP^{pos} CD105^{pos} or CD105^{neg} PaFs 7 days after co-injection.

(B) Tumor growth of subcutaneous injection of 10^5 PDA tumor cells or co-transplantation with 10^5 CD105^{pos} or CD105^{neg} PaFs in syngeneic B6 mice. n = 5 mice per condition. Data are representative of n = 4 separate experiments. For the combined condition a 1:1 mixture of CD105^{pos}:CD105^{neg} PaFs was used and the total number of PaFs kept constant.

(C) Kaplan-Meier analysis of tumors exceeding a threshold volume of 400 mm^3 (n = 4 independent studies, in total n = 14–22 mice per condition).

(D–F) As for (B) but with NOD-*scid.Il2rg*$^{-/-}$ (n = 4 to 5 per condition) (D) B6.*Rag1*$^{-/-}$ (n = 6 per condition) (E), and B6.*Batf3*$^{-/-}$ (n = 8 to 9 per condition) (F) mice.

(G) As for (A) but with CD105^{neg} PaFs disrupted for *H2Ab1*, *Cd74*, and *Cd80* expression. Non-targeting gRNA transfected CD105^{neg} PaFs were used as control.

(H–J) Bulk RNA-seq analysis of co-injected PDA tumor cells with CD105^{pos} (orange) and CD105^{neg} (purple) PaFs at day 10. Heatmap of differentially expressed genes displayed as row *Z* scores (H), Ingenuity Pathway Analysis of differentially activated pathways (I), and upstream regulators (J).

Data are displayed as mean tumor volumes ± standard error of the mean (SEM) (B–G). Conditions were compared using two-way ANOVA (B and D–G) and log rank test (C). *p < 0.05, **p < 0.01, ***p < 0.001.

See also Figure S7 and Table S6.

cultures from 18 normal tissues by MC, revealing both CD105^{pos} and CD105^{neg} fibroblast populations from most healthy murine tissues examined (Figures 7A and S8A; Table S7). Notably, the ratio of CD105^{pos} and CD105^{neg} fibroblasts varied across tissues, which may reflect inter-tissue heterogeneity or differential sensitivity to *in vitro* expansion. Fibroblast isolations, which

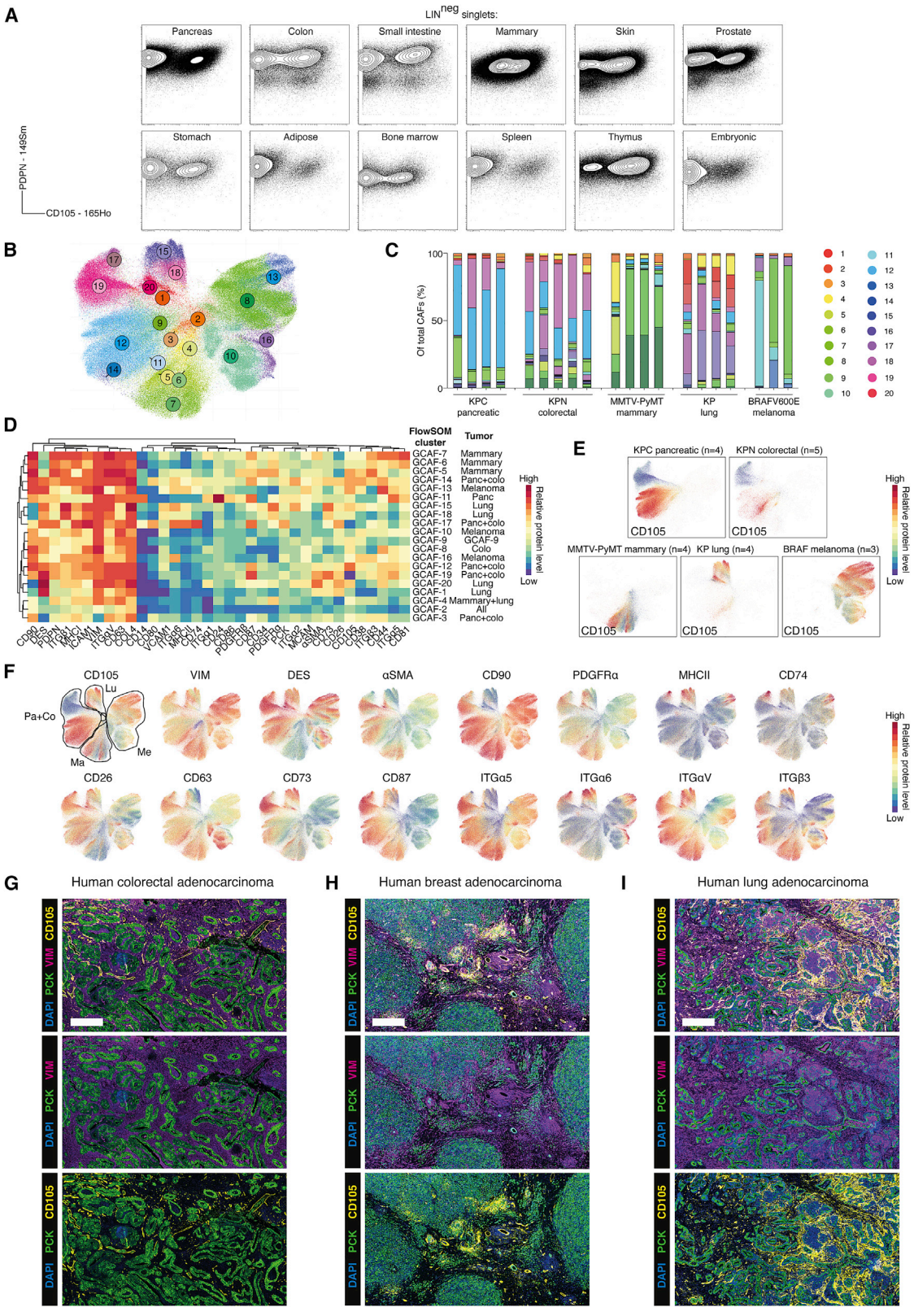

(legend on next page)

initially appeared homogeneous (such as isolations from the liver and lung), contained both CD105^{pos} and CD105^{neg} fibroblasts when analyzed at earlier time points (Figures S8A and S8B), suggesting that fibroblast heterogeneity can be rapidly lost by *in vitro* culture. Consistent with the observation that CD105 expression is restricted in PaFs, FACS-purified CD105^{pos} and CD105^{neg} fibroblasts from the liver and lung also retained differential CD105 expression *in vitro* (Figure S8C). Furthermore, gene expression analysis comparing CD105^{pos} and CD105^{neg} pancreatic and liver fibroblasts confirmed CD105 status as the major source of variation (Figure S8D), highlighting DEGs associated with CD105 status (Figures S8E and S8F).

We subsequently analyzed CAFs in 20 tumors from 5 autochthonous GEMMs (Figures 7B–7F and S8G–S8J). FlowSOM clustering and UMAP visualization highlighted the presence of distinct CAF subsets across all tumors (Figures 7B–7F and S8G–S8J). Interestingly, while lung (KP), mammary (MMTV-PyMT), and melanoma (BRAF^{V600E}) CAFs clustered according to their tissue of origin, several CAF clusters from pancreatic (KPC) and colorectal (KPN) tumors overlapped considerably, indicating phenotypic conservation of the CAFs between these two tissues (Figures 7B–7F). Few markers were broadly expressed (such as VIM, COLIV, CD63, and ITGαV) although none were expressed in all CAFs (Figures 7D, 7F, and S8G). Moreover, individual markers exhibited clear tissue-specific variation *in vivo* (Figures 7D and 7F). As expected, pancreatic tumors (KPC) contained mixtures of CD105^{pos} and CD105^{neg} CAFs, with CD105^{pos} CAFs favored. In contrast, colorectal (KPN) and mammary (MMTV-PyMT) tumors contained more abundant CD105^{neg} CAFs, whereas lung (KP) and melanoma (BRAF^{V600E}) tumors were dominated by CD105^{pos} CAFs (Figure 7E). This observation was supported by immunohistochemistry in FPPE human tumor samples (Figures 7G–7I and S8K–S8M; Table S7). Thus, CD105^{pos} and CD105^{neg} CAFs are present in normal and tumor-bearing mammalian tissue.

DISCUSSION

Fibroblast lineages play distinct roles in development, homeostasis, and wound repair of the skin, and specific fibroblast states are increasingly recognized as regulators of immune cell function in inflammatory disease and cancer (Dominguez et al., 2020; Driskell et al., 2013; Koliaraki et al., 2020; Rinkevich et al., 2015). CD105 is well established as an abundant and robust marker for all EC subtypes, pericytes, and mesenchymal stem cells, and has furthermore been noted in the stroma of human prostate and colorectal tumors and in human healthy breast tissue (Kato et al., 2018; Lv et al., 2014; Morsing et al., 2016; Paauwe et al., 2018; Pittenger et al., 2019). The data presented here demonstrate that CD105 demarks two pancreatic fibroblast lineages with distinct tumor-permissive and restrictive functions: CD105^{pos} fibroblasts are tumor permissive, whereas CD105^{neg} fibroblasts restrict tumor growth in a manner that is dependent on functional adaptive immunity.

Within both CD105^{pos} and CD105^{neg} fibroblast populations, environmentally regulated signals further diversify the fibroblast repertoire. For example, CD105^{pos} and CD105^{neg} populations respond differently to fibroblast-modulating signals, such as LIF, IL-1, and TGF-β, and apCAF and mesothelial cell markers (MHCII and CD74) are predominantly expressed in CD105^{neg} CAFs. Nonetheless, both populations express myCAF and iCAF markers *in vivo*, and isolated CD105^{pos} and CD105^{neg} PaFs can be induced to express myCAF and iCAF signature genes *in vitro*. Notably, CD105^{pos} fibroblasts are transcriptionally more responsive to TGF-β1, and *Eng* expression is decreased in CD105^{pos} iCAFs. This is in agreement with scRNA-seq data, which demonstrated expression of both myCAF and iCAF signature genes in both *Eng*^{pos} and *Eng*^{neg} subsets. However, within the *Eng*^{pos} subset, *Eng* expression correlates with the expression of established myCAF genes.

The detection of mesothelial cell transcripts (*Wt1*, *Msln*, *Krt8/18*, *Upk3b*) in a fraction of CD105^{neg} PDA CAFs indicate a developmental relationship between CD105^{neg} CAFs and the mesothelium. Indeed, mesothelial cells can adopt fibroblastic characteristics under TGF-β exposure (Namvar et al., 2018), and fibroblasts and smooth muscle cells in the lung and other trunk organs derive, in a sonic hedgehog-dependent process, from mesothelial precursors during tissue development (Cano et al., 2013; Dixit et al., 2013; Koopmans and Rinkevich, 2018; Rinkevich et al., 2012; Wilm, 2005). While mesothelial-like cells have been observed at the invasive edge of colorectal tumors (Gordillo et al., 2020), this cell type remains an otherwise understudied source of fibroblasts in tumors. The data presented here indicate that fibroblasts that are developmentally related to the mesothelium have intrinsically distinct functions. Future lineage-tracing studies will be needed to accurately determine whether CD105^{pos} and CD105^{neg} fibroblasts and CAFs arise from common or distinct differentiation hierarchies during tissue development.

The notable inter-tumoral heterogeneity of CAF subsets observed in PDA, combined with low preservation of CAF

Figure 7. CD105^{pos} and CD105^{neg} fibroblasts are identified in normal and tumor-bearing tissues

(A) MC analysis of *in-vitro*-expanded primary fibroblasts. Plots show PDPN and CD105 levels. LIN, EpCAM CD31 CD45.

(B) UMAP projection of CAFs from KPC pancreatic (n = 4), KPN colorectal (n = 5), MMTV-PyMT mammary (n = 4), KP lung (n = 4), and BRAF^{V600E} melanoma (n = 3) GEMMs. FlowSOM clusters are color coded. Total of 5 × 10^5 cell displayed.

(C) Stacked bar graphs of GEMM CAF (GCAF) clusters displayed as a fraction of total CAFs. FlowSOM colors based on (B).

(D) Heatmap of marker median mass intensities (MMIs) displayed as *Z* scores. Each GCAF FlowSOM cluster is grouped by unsupervised hierarchical clustering based on marker MMIs. Cell-type annotations based on canonical phenotypic markers are listed. Tumor type/s that the GCAF clusters predominantly arise from are listed.

(E) UMAP projection from (B) displaying overlaid signal intensity of CD105 with annotated tumor types.

(F) UMAP projection from (B) displaying overlaid signal intensity of example markers. The tumor types of origin are highlighted: Pa, pancreatic; Co, colorectal; Ma, mammary; Lu, lung; Me, melanoma.

(G–I) Representative IHC analysis of human colorectal (n = 9), breast (n = 8), and lung adenocarcinoma (n = 6) tumor samples stained for pan-cytokeratin (PCK) (green), vimentin (VIM) (purple), CD105 (yellow), and DAPI (blue). Scale bar, 500 μm.

See also Figure S8 and Table S7.

subsets across tumors in different organs, underscores the importance of determining the functional roles of CAF subsets across different tissues and tumors. For example, while CD26 defines fibroblasts lineages in the skin (Driskell et al., 2013; Rinkevich et al., 2015), it is dynamically regulated in PaFs. Moreover, although $CD105^{pos}$ and $CD105^{neg}$ fibroblasts isolated from the pancreas and liver show stable CD105 expression and exhibit conserved gene expression patterns, many genes remain expressed in a tissue-specific manner.

Single-cell technologies, such as MC, have been instrumental to define cellular subsets in the TME (Bendall et al., 2011; Chevrier et al., 2017). Whereas the abundance and phenotype within cell populations can be readily compared across tumors and tissues, tumor and stromal cells may exhibit differences in their liberation and details of local tissue structure is lost. Thus, future *in situ* studies are needed to establish regional differences in the cellular neighborhood of $CD105^{pos}$ and $CD105^{neg}$ CAFs.

Determining how inherent tumor-restrictive effects of naive $CD105^{neg}$ PaFs are bypassed as tumors develop, and whether anti-tumor immunity may also be regulated by $CD105^{neg}$ CAFs in established tumors is important. Indeed, the balance between $CD105^{pos}$ and $CD105^{neg}$ fibroblasts could be a key determinant of the local immune environment in PDA and may be exploited therapeutically. However, the function of $CD105^{pos}$ CAFs needs further characterization. Specifically, mono-injections of the PDA tumor cell lines used in this study grew aggressively and therefore only minimally depended on stromal-supportive signals, suggesting that tumor promoting effects from co-injected fibroblasts may not be fully captured with this model. Moreover, while $CD105^{pos}$ and $CD105^{neg}$ fibroblast populations are identified in multiple tumors and normal tissues, and also appear preserved in human tissue, further studies are needed to determine whether the tumor-permissive and restrictive functions of $CD105^{pos}$ and $CD105^{neg}$ fibroblasts are broadly conserved.

We envisage that the presented phenotypic atlas will accelerate much needed functional studies of the mesenchyme to improve our understanding of shared fibroblast features across different tissues to thereby enhance the application of stromal-targeting therapies.

STAR★METHODS

Detailed methods are provided in the online version of this paper and include the following:

- KEY RESOURCES TABLE
- RESOURCE AVAILABILITY
  - Lead contact
  - Materials availability
  - Data and code availability
- EXPERIMENTAL MODELS
  - Animal models
  - Human tissue samples
  - Cell lines and culture
- METHODS DETAILS
  - Mass cytometry antibody conjugation
  - Tumor disaggregations
  - Mass cytometry live/dead and extracellular staining
  - Mass cytometry barcoding and intracellular staining
  - Mass cytometry DNA staining and acquisition
  - Mass cytometry data processing
  - Mouse organ disaggregations
  - Mass cytometry cell signaling panel generation
  - Mass cytometry signaling analysis
  - Multiplexed immunofluorescence
  - FACS and flow cytometry
  - Bulk RNA sequencing and analysis
  - scRNA-seq re-analysis
  - scRNA-seq of *in vitro* pancreatic fibroblasts
  - *In vitro* fibroblast isolation and culture
  - BioMark HD multiplex qPCR
  - Genetically engineered annimal models
  - Subcutaneous co-transplant model
  - Immunohistochemistry of subcutaneous tumors
  - CRISPR-Cas-9 gene editing
- QUANTIFICATION AND STATISTICAL ANALYSIS

SUPPLEMENTAL INFORMATION

Supplemental information can be found online at https://doi.org/10.1016/j.ccell.2021.06.017.

ACKNOWLEDGMENTS

This work was supported by Cancer Research UK Institute Awards C5759/A27412 (to C.J., A.M., R.M., C.S., and S.Z.), A17196 and A21139 (to O.J.S.), and A29996 (to J.P.M.), Experimental Medicine Programme Award (A25236 to C.J., O.J.S., and J.P.M.) and European Research Council Consolidator Award (ERC-2017-COG 772577 to C.J.).

A.L. received funding from ASCO Conquer Cancer Foundation Young Investigator Award and The Christie Charity. The authors would like to acknowledge colleagues at CRUK Manchester Institute Systems Oncology Team for valuable input, CRUK Manchester Institute core facilities, in particular flow cytometry, molecular biology, and visualization irradiation analysis, as well as the Biological Services Unit at the CRUK Beatson Institute. We would also like to thank William C. Hahn, Didier Trono, Inder Verma, Fernando Calvo, and Tim Somervaille for kindly sharing plasmids. Graphical abstract was created with images from BioRender.com.

AUTHOR CONTRIBUTIONS

C.H. planned and conducted the experiments, analyzed the data, and wrote the manuscript. A.B.-G., F.H., and E.H. planned and conducted the experiments and analyzed the data. A.B. analyzed the data. A.K. conducted computational analysis. X.Z. planned and conducted the experiments. A.B., S. Karim, S. Kemp, D.W., J.K., and V.P.-H. provided technical support, conducted experiments, and provided reagents. F.H., N.S., and S. Karim, S. Kemp conducted the experiments and analyzed the data. A.L., J.V., M.P.d.M., R.-F.J., O.J.S., F.L., C.S., M.M., A.M., L.C., and R.M. provided reagents and experimental advice. S.Z. provided reagents and oversight. J.P.M. conducted the experiments, and provided reagents and oversight. C.J. conceived the project, analyzed the data, provided oversight, and wrote the manuscript.

DECLARATION OF INTERESTS

O.S. receives funding from Novartis, AstraZeneca, RedEx and Cancer Research Technology. C.J. receives funding from AstraZeneca. R.M. is an expert witness for Pfizer and, as a former employee of the Institute of Cancer Research (ICR) in London, may benefit financially from commercialized programs. C.S. and F.L. are former employees of the ICR in London and may benefit financially from commercialized programs. The other authors declare no competing interests.

Received: July 28, 2020
Revised: April 19, 2021
Accepted: June 25, 2021
Published: July 22, 2021

REFERENCES

Anders, S., and Huber, W. (2010). Differential expression analysis for sequence count data. Genome Biol. *11*, R106.

Bankhead, P., Loughrey, M.B., Fernandez, J.A., Dombrowski, Y., McArt, D.G., Dunne, P.D., McQuaid, S., Gray, R.T., Murray, L.J., Coleman, H.G., et al. (2017). QuPath: open source software for digital pathology image analysis. Sci. Rep. *7*, 16878.

Becht, E., Giraldo, N.A., Lacroix, L., Buttard, B., Elarouci, N., Petitprez, F., Selves, J., Laurent-Puig, P., Sautès-Fridman, C., Fridman, W.H., et al. (2016). Estimating the population abundance of tissue-infiltrating immune and stromal cell populations using gene expression. Genome Biol. *17*, 218.

Becht, E., McInnes, L., Healy, J., Dutertre, C.-A., Kwok, I.W.H., Ng, L.G., Ginhoux, F., and Newell, E.W. (2018). Dimensionality reduction for visualizing single-cell data using UMAP. Nat. Biotechnol. *37*, 38–44.

Bendall, S.C., and Nolan, G.P. (2012). From single cells to deep phenotypes in cancer. Nat. Biotechnol. *30*, 639–647.

Bendall, S.C., Simonds, E.F., Qiu, P., Amir, E.-A.D., Krutzik, P.O., Finck, R., Bruggner, R.V., Melamed, R., Trejo, A., Ornatsky, O.I., et al. (2011). Single-cell mass cytometry of differential immune and drug responses across a human hematopoietic continuum. Science *332*, 687–696.

Biffi, G., Oni, T.E., Spielman, B., Hao, Y., Elyada, E., Park, Y., Preall, J., and Tuveson, D.A. (2019). IL1-Induced JAK/STAT signaling is antagonized by TGFβ to shape CAF heterogeneity in pancreatic ductal adenocarcinoma. Cancer Discov. *9*, 282–301.

Butler, A., Hoffman, P., Smibert, P., Papalexi, E., and Satija, R. (2018). Integrating single-cell transcriptomic data across different conditions, technologies, and species. Nat. Biotechnol. *36*, 411–420.

Candido, J.B., Morton, J.P., Bailey, P., Campbell, A.D., Karim, S.A., Jamieson, T., Lapienyte, L., Gopinathan, A., Clark, W., McGhee, E.J., et al. (2018). CSF1R+ macrophages sustain pancreatic tumor growth through T cell suppression and maintenance of key gene programs that define the squamous subtype. CellReports *23*, 1448–1460.

Cano, E., Carmona, R., and Muñoz-Chápuli, R. (2013). Wt1-expressing progenitors contribute to multiple tissues in the developing lung. Am. J. Physiol. Lung Cell. Mol. Physiol. *305*, L322–L332.

Catenacci, D.V.T., Junttila, M.R., Karrison, T., Bahary, N., Horiba, M.N., Nattam, S.R., Marsh, R., Wallace, J., Kozloff, M., Rajdev, L., et al. (2015). Randomized phase Ib/II study of gemcitabine plus placebo or vismodegib, a hedgehog pathway inhibitor, in patients with metastatic pancreatic cancer. J. Clin. Oncol. *33*, 4284–4292.

Chevrier, S., Levine, J.H., Zanotelli, V.R.T., Silina, K., Schulz, D., Bacac, M., Ries, C.H., Ailles, L., Jewett, M.A.S., Moch, H., et al. (2017). An immune atlas of clear cell renal cell carcinoma. Cell *169*, 736–738.e18.

Clark, C.E., Hingorani, S.R., Mick, R., Combs, C., Tuveson, D.A., and Vonderheide, R.H. (2007). Dynamics of the immune reaction to pancreatic cancer from inception to invasion. Cancer Res. *67*, 9518–9527.

Collins, M.A., Bednar, F., Zhang, Y., Brisset, J.-C., Galbán, S., Galbán, C.J., Rakshit, S., Flannagan, K.S., Adsay, N.V., and Pasca di Magliano, M. (2012). Oncogenic Kras is required for both the initiation and maintenance of pancreatic cancer in mice. J. Clin. Invest. *122*, 639–653.

Croft, A.P., Campos, J., Jansen, K., Turner, J.D., Marshall, J., Attar, M., Savary, L., Wehmeyer, C., Naylor, A.J., Kemble, S., et al. (2019). Distinct fibroblast subsets drive inflammation and damage in arthritis. Nature *570*, 246–251.

Dakin, S.G., Coles, M., Sherlock, J.P., Powrie, F., Carr, A.J., and Buckley, C.D. (2018). Pathogenic stromal cells as therapeutic targets in joint inflammation. Nat. Rev. Rheumatol. *14*, 1–13.

Dhomen, N., Reis-Filho, J.S., da Rocha Dias, S., Hayward, R., Savage, K., Delmas, V., Larue, L., Pritchard, C., and Marais, R. (2009). Oncogenic Braf induces melanocyte senescence and melanoma in mice. Cancer Cell *15*, 294–303.

Di Mitri, D., Mirenda, M., Vasilevska, J., Calcinotto, A., Delaleu, N., Revandkar, A., Gil, V., Boysen, G., Losa, M., Mosole, S., et al. (2019). Re-education of tumor-associated macrophages by CXCR2 blockade drives senescence and tumor inhibition in advanced prostate cancer. Cell Rep. *28*, 2156–2168.e5.

Dixit, R., Ai, X., and Fine, A. (2013). Derivation of lung mesenchymal lineages from the fetal mesothelium requires hedgehog signaling for mesothelial cell entry. Development *140*, 4398–4406.

Dominguez, C.X., Muller, S., Keerthivasan, S., Koeppen, H., Hung, J., Gierke, S., Breart, B., Foreman, O., Bainbridge, T.W., Castiglioni, A., et al. (2020). Single-cell RNA sequencing reveals stromal evolution into LRRC15+ myofibroblasts as a determinant of patient response to cancer immunotherapy. Cancer Discov. *10*, 232–253.

Driskell, R.R., and Watt, F.M. (2015). Understanding fibroblast heterogeneity in the skin. Trends Cell Biol. *25*, 92–99.

Driskell, R.R., Lichtenberger, B.M., Hoste, E., Kretzschmar, K., Simons, Ben D., Charalambous, M., Ferron, S.R., Herault, Y., Pavlovic, G., Ferguson-Smith, A.C., et al. (2013). Distinct fibroblast lineages determine dermal architecture in skin development and repair. Nature *504*, 277–281.

Elyada, E., Bolisetty, M., Laise, P., Flynn, W.F., Courtois, E.T., Burkhart, R.A., Teinor, J.A., Belleau, P., Biffi, G., Lucito, M.S., et al. (2019). Cross-species single-cell analysis of pancreatic ductal adenocarcinoma reveals antigen-presenting cancer-associated fibroblasts. Cancer Discov. *9*, 1102–1123.

Feig, C., Jones, J.O., Kraman, M., Wells, R.J.B., Deonarine, A., Chan, D.S., Connell, C.M., Roberts, E.W., Zhao, Q., Caballero, O.L., et al. (2013). Targeting CXCL12 from FAP-expressing carcinoma-associated fibroblasts synergizes with anti-PD-L1 immunotherapy in pancreatic cancer. Proc. Natl. Acad. Sci. *110*, 20212–20217.

Gordillo, C.H., Sandoval, P., Muñoz-Hernández, P., Pascual-Antón, L., López-Cabrera, M., and Jiménez-Heffernan, J.A. (2020). Mesothelial-to-mesenchymal transition contributes to the generation of carcinoma-associated fibroblasts in locally advanced primary colorectal carcinomas. Cancers *12*, 499.

Guy, C.T., Cardiff, R.D., and Muller, W.J. (1992). Induction of mammary tumors by expression of polyomavirus middle T oncogene: a transgenic mouse model for metastatic disease. Mol. Cell. Biol. *12*, 954–961.

Hahne, F., LeMeur, N., Brinkman, R.R., Ellis, B., Haaland, P., Sarkar, D., Spidlen, J., Strain, E., and Gentleman, R. (2009). flowCore: a Bioconductor package for high throughput flow cytometry. BMC Bioinformatics *10*, 106.

Halbrook, C.J., Pontious, C., Kovalenko, I., Lapienyte, L., Dreyer, S., Lee, H.-J., Thurston, G., Zhang, Y., Lazarus, J., Sajjakulnukit, P., et al. (2019). Macrophage-released pyrimidines inhibit gemcitabine therapy in pancreatic cancer. Cell Metab. *29*, 1390–1399.e1396.

Han, G., Spitzer, M.H., Bendall, S.C., Fantl, W.J., and Nolan, G.P. (2018). Metal-isotope-tagged monoclonal antibodies for high-dimensional mass cytometry. Nat. Protoc. *13*, 2121–2148.

Harris, W.J., Huang, X., Lynch, J.T., Spencer, G.J., Hitchin, J.R., Li, Y., Ciceri, F., Blaser, J.G., Greystoke, B.F., Jordan, A.M., et al. (2012). The histone demethylase KDM1A sustains the oncogenic potential of MLL-AF9 leukemia stem cells. Cancer Cell *21*, 473–487.

Hashimshony, T., Senderovich, N., Avital, G., Klochendler, A., de Leeuw, Y., Anavy, L., Gennert, D., Li, S., Livak, K.J., Rozenblatt-Rosen, O., et al. (2016). CEL-Seq2: sensitive highly-multiplexed single-cell RNA-Seq. Genome Biol. *17*, 77.

Helms, E., Onate, M.K., and Sherman, M.H. (2020). Fibroblast heterogeneity in the pancreatic tumor microenvironment. Cancer Discov. *10*, 1–10.

Hildner, K., Edelson, B.T., Purtha, W.E., Diamond, M., Matsushita, H., Kohyama, M., Calderon, B., Schraml, B.U., Unanue, E.R., Diamond, M.S., et al. (2008). Batf3 deficiency reveals a critical role for CD8alpha+ dendritic cells in cytotoxic T cell immunity. Science *322*, 1097–1100.

Hingorani, S.R., Wang, L., Multani, A.S., Combs, C., Deramaudt, T.B., Hruban, R.H., Rustgi, A.K., Chang, S., and Tuveson, D.A. (2005). Trp53R172H and KrasG12D cooperate to promote chromosomal instability and widely metastatic pancreatic ductal adenocarcinoma in mice. Cancer Cell *7*, 469–483.

Hirata, E., Girotti, M.R., Viros, A., Hooper, S., Spencer-Dene, B., Matsuda, M., Larkin, J., Marais, R., and Sahai, E. (2015). Intravital imaging reveals how BRAF inhibition generates drug-tolerant microenvironments with high integrin β1/FAK signaling. Cancer Cell *27*, 574–588.

Jackson, E.L., Willis, N., Mercer, K., Bronson, R.T., Crowley, D., Montoya, R., Jacks, T., and Tuveson, D.A. (2001). Analysis of lung tumor initiation and progression using conditional expression of oncogenic K-ras. Genes Dev. *15*, 3243–3248.

Jackson, H.W., Fischer, J.R., Zanotelli, V.R.T., Ali, H.R., Mechera, R., Soysal, S.D., Moch, H., Muenst, S., Varga, Z., Weber, W.P., et al. (2020). The single-cell pathology landscape of breast cancer. Nature *177*, 1–25.

Jackstadt, R., van Hooff, S.R., Leach, J.D., Cortes-Lavaud, X., Lohuis, J.O., Ridgway, R.A., Wouters, V.M., Roper, J., Kendall, T.J., Roxburgh, C.S., et al. (2019). Epithelial NOTCH signaling rewires the tumor microenvironment of colorectal cancer to drive poor-prognosis subtypes and metastasis. Cancer Cell *36*, 319–336 e317.

Janes, K.A. (2016). Single-cell states versus single-cell atlases—two classes of heterogeneity that differ in meaning and method. Curr. Opin. Biotechnol. *39*, 120–125.

Jiang, H., Hegde, S., Knolhoff, B.L., Zhu, Y., Herndon, J.M., Meyer, M.A., Nywening, T.M., Hawkins, W.G., Shapiro, I.M., Weaver, D.T., et al. (2016). Targeting focal adhesion kinase renders pancreatic cancers responsive to checkpoint immunotherapy. Nat. Med. *22*, 1–13.

Kato, M., Placencio-Hickok, V.R., Madhav, A., Haldar, S., Tripathi, M., Billet, S., Mishra, R., Smith, B., Rohena-Rivera, K., Agarwal, P., et al. (2018). Heterogeneous cancer-associated fibroblast population potentiates neuroendocrine differentiation and castrate resistance in a CD105-dependent manner. Oncogene *303*, 1–15.

Kim, E.J., Sahai, V., Abel, E.V., Griffith, K.A., Greenson, J.K., Takebe, N., Khan, G.N., Blau, J.L., Craig, R., Balis, U.G., et al. (2014). Pilot clinical trial of hedgehog pathway inhibitor GDC-0449 (vismodegib) in combination with gemcitabine in patients with metastatic pancreatic adenocarcinoma. Clin. Cancer Res. *20*, 5937–5945.

Koliaraki, V., Prados, A., Armaka, M., and Kollias, G. (2020). The mesenchymal context in inflammation, immunity and cancer. Nat. Immunol. *21*, 974–982. https://doi.org/10.1038/s41590-020-0741-2.

Koopmans, T., and Rinkevich, Y. (2018). Mesothelial to mesenchyme transition as a major developmental and pathological player in trunk organs and their cavities. Commun. Biol. *1*, 170.

Kumar, S., Lun, X.K., Bodenmiller, B., Rodriguez Martinez, M., and Koeppl, H. (2020). Stabilized reconstruction of signaling networks from single-cell cue-response data. Sci. Rep. *10*, 1233.

Kuppe, C., Ibrahim, M.M., Kranz, J., Zhang, X., Ziegler, S., n, J.P.-P.X., Jansen, J., Reimer, K.C., Smith, J.R., Dobie, R., et al. (2020). Decoding myofibroblast origins in human kidney fibrosis. Nature *589*, 1–42.

Leun, A.M., Thommen, D.S., and Schumacher, T.N. (2020). CD8+ T cell states in human cancer: insights from single-cell analysis. Nat. Rev. Cancer *77*, 1–15.

Lichtenberger, B.M., Mastrogiannaki, M., and Watt, F.M. (2016). Epidermal β-catenin activation remodels the dermis via paracrine signalling to distinct fibroblast lineages. Nat. Commun. *7*, 10537.

Love, M.I., Huber, W., and Anders, S. (2014). Moderated estimation of fold change and dispersion for RNA-seq data with DESeq2. Genome Biol. *15*, 550.

Luche, H., Weber, O., Nageswara Rao, T., Blum, C., and Fehling, H.J. (2007). Faithful activation of an extra-bright red fluorescent protein in "knock-in" Cre-reporter mice ideally suited for lineage tracing studies. Eur. J. Immunol. *37*, 43–53.

Lun, X.K., Szklarczyk, D., Gabor, A., Dobberstein, N., Zanotelli, V.R.T., Saez-Rodriguez, J., von Mering, C., and Bodenmiller, B. (2019). Analysis of the human kinome and phosphatome by mass cytometry reveals overexpression-induced effects on cancer-related signaling. Mol. Cell *74*, 1086–1102 e1085.

Lun, X.K., Zanotelli, V.R., Wade, J.D., Schapiro, D., Tognetti, M., Dobberstein, N., and Bodenmiller, B. (2017). Influence of node abundance on signaling network state and dynamics analyzed by mass cytometry. Nat. Biotechnol. *35*, 164–172.

Lv, F.-J., Tuan, R.S., Cheung, K.M.C., and Leung, V.Y.L. (2014). Concise review: the surface markers and identity of human mesenchymal stem cells. Stem Cells *32*, 1408–1419.

Marino, S., Vooijs, M., van Der Gulden, H., Jonkers, J., and Berns, A. (2000). Induction of medulloblastomas in p53-null mutant mice by somatic inactivation of Rb in the external granular layer cells of the cerebellum. Genes Dev. *14*, 994–1004.

Mercer, K., Giblett, S., Green, S., Lloyd, D., DaRocha Dias, S., Plumb, M., Marais, R., and Pritchard, C. (2005). Expression of endogenous oncogenic V600EB-raf induces proliferation and developmental defects in mice and transformation of primary fibroblasts. Cancer Res. *65*, 11493–11500.

Meuwissen, R., Linn, S.C., van der Valk, M., Mooi, W.J., and Berns, A. (2001). Mouse model for lung tumorigenesis through Cre/lox controlled sporadic activation of the K-Ras oncogene. Oncogene *20*, 6551–6558.

Miller, B.W., Morton, J.P., Pinese, M., Saturno, G., Jamieson, N.B., McGhee, E., Timpson, P., Leach, J., McGarry, L., Shanks, E., et al. (2015). Targeting the LOX/hypoxia axis reverses many of the features that make pancreatic cancer deadly: inhibition of LOX abrogates metastasis and enhances drug efficacy. EMBO Mol. Med. *7*, 1063–1076.

Mombaerts, P., Iacomini, J., Johnson, R.S., Herrup, K., Tonegawa, S., and Papaioannou, V.E. (1992). RAG-1-deficient mice have no mature B and T lymphocytes. Cell *68*, 869–877.

Morsing, M., Klitgaard, M.C., Jafari, A., Villadsen, R., Kassem, M., Petersen, O.W., and Rønnov-Jessen, L. (2016). Evidence of two distinct functionally specialized fibroblast lineages in breast stroma. Breast Cancer Res. *18*, 108–119.

Muraro, M.J., Dharmadhikari, G., Grun, D., Groen, N., Dielen, T., Jansen, E., van Gurp, L., Engelse, M.A., Carlotti, F., de Koning, E.J., et al. (2016). A single-cell transcriptome atlas of the human pancreas. Cell Syst. *3*, 385–394 e383.

Namvar, S., Woolf, A.S., Zeef, L.A., Wilm, T., Wilm, B., and Herrick, S.E. (2018). Functional molecules in mesothelial-to-mesenchymal transition revealed by transcriptome analyses. J. Pathol. *245*, 491–501.

Olive, K.P., Jacobetz, M.A., Davidson, C.J., Gopinathan, A., McIntyre, D., Honess, D., Madhu, B., Goldgraben, M.A., Caldwell, M.E., Allard, D., et al. (2009). Inhibition of Hedgehog signaling enhances delivery of chemotherapy in a mouse model of pancreatic cancer. Science *324*, 1457–1461.

Öhlund, D., Handly-Santana, A., Biffi, G., Elyada, E., Almeida, A.S., Ponz-Sarvise, M., Corbo, V., Oni, T.E., Hearn, S.A., Lee, E.J., et al. (2017). Distinct populations of inflammatory fibroblasts and myofibroblasts in pancreatic cancer. J. Exp. Med. *214*, 579–596.

Özdemir, B.C., Pentcheva-Hoang, T., Carstens, J.L., Zheng, X., Wu, C.-C., Simpson, T.R., Laklai, H., Sugimoto, H., Kahlert, C., Novitskiy, S.V., et al. (2014). Depletion of carcinoma-associated fibroblasts and fibrosis induces immunosuppression and accelerates pancreas cancer with reduced survival. Cancer Cell *25*, 1–16.

Paauwe, M., Schoonderwoerd, M.J.A., Helderman, R.F.C.P., Harryvan, T.J., Groenewoud, A., van Pelt, G.W., Bor, R., Hemmer, D.M., Versteeg, H.H., Snaar-Jagalska, B.E., et al. (2018). Endoglin expression on cancer-associated fibroblasts regulates invasion and stimulates colorectal cancer metastasis. Clin. Cancer Res. *24*, 6331–6344.

Philip, M., Fairchild, L., Sun, L., Horste, E.L., Camara, S., Shakiba, M., Scott, A.C., Viale, A., Lauer, P., Merghoub, T., et al. (2017). Chromatin states define tumour-specific T cell dysfunction and reprogramming. Nature *545*, 452–456.

Pittenger, M.F., Discher, D.E., Péault, B.M., Phinney, D.G., Hare, J.M., and Caplan, A.I. (2019). Mesenchymal stem cell perspective: cell biology to clinical progress. NPJ Regen. Med. *4*, 1–15.

Provenzano, P.P., Cuevas, C., Chang, A.E., Goel, V.K., Hoff Von, D.D., and Hingorani, S.R. (2012). Enzymatic targeting of the stroma ablates physical barriers to treatment of pancreatic ductal adenocarcinoma. Cancer Cell *21*, 418–429.

Rapsomaniki, M.A., Lun, X.K., Woerner, S., Laumanns, M., Bodenmiller, B., and Martinez, M.R. (2018). CellCycleTRACER accounts for cell cycle and volume in mass cytometry data. Nat. Commun. *9*, 632.

Rhim, A.D., Oberstein, P.E., Thomas, D.H., Mirek, E.T., Palermo, C.F., Sastra, S.A., Dekleva, E.N., Saunders, T., Becerra, C.P., Tattersall, I.W., et al. (2014). Stromal elements act to restrain, rather than support, pancreatic ductal adenocarcinoma. Cancer Cell *25*, 735–747.

Rinkevich, Y., Walmsley, G.G., Hu, M.S., Maan, Z.N., Newman, A.M., Drukker, M., Januszyk, M., Krampitz, G.W., Gurtner, G.C., Lorenz, H.P., et al. (2015). Identification and isolation of a dermal lineage with intrinsic fibrogenic potential. Science *348*, aaa2151.

Rinkevich, Y., Mori, T., Sahoo, D., Xu, P.-X., Bermingham, J.R., and Weissman, I.L. (2012). Identification and prospective isolation of a mesothelial precursor lineage giving rise to smooth muscle cells and fibroblasts for mammalian internal organs, and their vasculature. Nat. Cell Biol. *14*, 1251–1260.

Sahai, E., Astsaturov, I., Cukierman, E., DeNardo, D.G., Egeblad, M., Evans, R.M., Fearon, D., Greten, F.R., Hingorani, S.R., Hunter, T., et al. (2020). A framework for advancing our understanding of cancer-associated fibroblasts. Nat. Rev. Cancer *6*, 1–13.

Shi, Y., Gao, W., Lytle, N.K., Huang, P., Yuan, X., Dann, A.M., Ridinger-Saison, M., DelGiorno, K.E., Antal, C.E., Liang, G., et al. (2019). Targeting LIF-mediated paracrine interaction for pancreatic cancer therapy and monitoring. Nature *569*, 1–27.

Simoni, Y., Becht, E., Fehlings, M., Loh, C.Y., Koo, S.-L., Teng, K.W.W., Yeong, J.P.S., Nahar, R., Zhang, T., Kared, H., et al. (2018). Bystander CD8+ T cells are abundant and phenotypically distinct in human tumour infiltrates. Nature *557*, 575–579.

Spitzer, M.H., Carmi, Y., Reticker-Flynn, N.E., Kwek, S.S., Madhireddy, D., Martins, M.M., Gherardini, P.F., Prestwood, T.R., Chabon, J., Bendall, S.C., et al. (2017). Systemic immunity is required for effective cancer immunotherapy. Cell *168*, 487–502.e15.

Steele, C.W., Karim, S.A., Leach, J.D.G., Bailey, P., Upstill-Goddard, R., Rishi, L., Foth, M., Bryson, S., McDaid, K., Wilson, Z., et al. (2016). CXCR2 inhibition profoundly suppresses metastases and augments immunotherapy in pancreatic ductal adenocarcinoma. Cancer Cell *29*, 832–845.

Steele, N.G., Carpenter, E.S., Kemp, S.B., Sirihorachai, V.R., The, S., Delrosario, L., Lazarus, J., Amir, E.-a.D., Gunchick, V., Espinoza, C., et al. (2020). Multimodal mapping of the tumor and peripheral blood immune landscape in human pancreatic cancer. Nat. Cancer *1*, 1097–1112.

Su, S., Chen, J., Yao, H., Liu, J., Yu, S., Lao, L., Wang, M., Luo, M., Xing, Y., Chen, F., et al. (2018). CD10+GPR77+ cancer-associated fibroblasts promote cancer formation and chemoresistance by sustaining cancer stemness. Cell *172*, 1–33.

Tape, C.J., Ling, S., Dimitriadi, M., McMahon, K.M., Worboys, J.D., Leong, H.S., Norrie, I.C., Miller, C.J., Poulogiannis, G., Lauffenburger, D.A., et al. (2016). Oncogenic KRAS regulates tumor cell signaling via stromal reciprocation. Cell *165*, 910–920.

Thommen, D.S., Koelzer, V.H., Herzig, P., Roller, A., Trefny, M., Dimeloe, S., Kiialainen, A., Hanhart, J., Schill, C., Hess, C., et al. (2018). A transcriptionally and functionally distinct PD-1+ CD8+ T cell pool with predictive potential in non-small-cell lung cancer treated with PD-1 blockade. Nat. Med. *24*, 1–17.

Tirosh, I., Izar, B., Prakadan, S.M., Wadsworth, M.H., Treacy, D., Trombetta, J.J., Rotem, A., Rodman, C., Lian, C., Murphy, G., et al. (2016). Dissecting the multicellular ecosystem of metastatic melanoma by single-cell RNA-seq. Science *352*, 189–196.

Valluru, M., Staton, C.A., Reed, M.W.R., and Brown, N.J. (2011). Transforming growth factor-β and endoglin signaling orchestrate wound healing. Front. Physiol. *2*, 89.

Van den Brink, S.C., Sage, F., Vertesy, A., Spanjaard, B., Peterson-Maduro, J., Baron, C.S., Robin, C., and van Oudenaarden, A. (2017). Single-cell sequencing reveals dissociation-induced gene expression in tissue subpopulations. Nat. Methods *14*, 935–936.

Van Gassen, S., Callebaut, B., Van Helden, M.J., Lambrecht, B.N., Demeester, P., Dhaene, T., and Saeys, Y. (2015). FlowSOM: using self-organizing maps for visualization and interpretation of cytometry data. Cytometry *87*, 636–645.

Wei, K., Korsunsky, I., Marshall, J.L., Gao, A., Watts, G.F.M., Major, T., Croft, A.P., Watts, J., Blazar, P.E., Lange, J.K., et al. (2020). Notch signalling drives synovial fibroblast identity and arthritis pathology. Nature *582*, 259–264.

Wilm, B. (2005). The serosal mesothelium is a major source of smooth muscle cells of the gut vasculature. Development *132*, 5317–5328.

Wohlfahrt, T., Rauber, S., Uebe, S., Luber, M., Soare, A., Ekici, A., Weber, S., Matei, A.-E., Chen, C.-W., Maier, C., et al. (2019). PU.1 controls fibroblast polarization and tissue fibrosis. Nature *566*, 1–27.

Yajima, I., Belloir, E., Bourgeois, Y., Kumasaka, M., Delmas, V., and Larue, L. (2006). Spatiotemporal gene control by the Cre-ERT2 system in melanocytes. Genesis *44*, 34–43.

Yost, K.E., Satpathy, A.T., Wells, D.K., Qi, Y., Wang, C., Kageyama, R., McNamara, K.L., Granja, J.M., Sarin, K.Y., Brown, R.A., et al. (2019). Clonal replacement of tumor-specific T cells following PD-1 blockade. Nat. Med. *25*, 1–33.

Zunder, E.R., Finck, R., Behbehani, G.K., Amir el, A.D., Krishnaswamy, S., Gonzalez, V.D., Lorang, C.G., Bjornson, Z., Spitzer, M.H., Bodenmiller, B., et al. (2015). Palladium-based mass tag cell barcoding with a doublet-filtering scheme and single-cell deconvolution algorithm. Nat. Protoc. *10*, 316–333.

STAR★METHODS

KEY RESOURCES TABLE

REAGENT or RESOURCE	SOURCE	IDENTIFIER
Antibodies		
Fc block clone 2.4G2	BD Biosciences	558636
Anti-mouse CD44 clone IM7	Biolegend	103002
Anti-mouse EpCAM clone G8.8	Biolegend	118202
Anti-mouse CD86 clone GL-1	Biolegend	105002
Anti-mouse MCAM 141Pr clone ME-9F1	Fluidigm	3141016B
Anti-mouse ITGA5 clone 5H10-27(MFR5)	Biolegend	103801
Anti-mouse CD81 clone Eat-2	Biolegend	104902
Anti-mouse CD87 clone 109801	Thermo Fisher	MA5-23853
Anti-PE 145Nd clone PE001	Fluidigm	3145006B
Anti-mouse ITGAV clone RMV-7	Biolegend	104102
Anti-mouse ITGA2 clone Hma2	Biolegend	103501
Anti-mouse PDGFRA 148Nd clone APA5	Fluidigm	3148018B
Anti-mouse PDPN clone 8.1.1	Biolegend	127402
Anti-mouse CD24 (150Nd) clone M1/69	Fluidigm	3150009B
Anti-mouse PDGFRB (151Eu) clone APB5	Fluidigm	3151017B
Anti-mouse ICAM1 clone YN1/1.7.4	Biolegend	116102
Anti-mouse CD63 clone NVG-2	Biolegend	143902
Anti-mouse CD73 clone TY/11.8	Biolegend	127202
Anti-FITC 160Gd clone FIT-22	Fluidigm	3160011B
Anti-mouse ITGB3 clone Cc9.G2 (HMB3-1)	Biolegend	104302
Anti-mouse CD34 clone MEC14.7	Biolegend	119302
Anti-mouse ITGA6 clone GoH3	Biolegend	313602
Anti-Biotin 165Ho clone 1D4-C5	Fluidigm	3165012B
Anti-mouse CD14 clone Sa14-2	Biolegend	123302
Anti-mouse CD74 clone In1/CD74	Biolegend	151002
Anti-mouse CD80 clone 16-10A1	Biolegend	104702
Anti-mouse CD31 clone MEC13.3	Biolegend	102502
Anti-mouse CD38 171Yb clone 90	Fluidigm	3171007B
Anti-mouse ITGB1 clone HMB1-1	Biolegend	102202
Anti-mouse VCAM1 clone 429 (MVCAM.A)	Biolegend	105702
Anti-mouse CD45 175Lu clone 30-F11	Fluidigm	3175010B
Anti-APC 176Yb clone APC003	Fluidigm	3176007B
Anti-mouse MHCI clone 28-14-8	Biolegend	114502
Anti-mouse MHCII 209Bi clone M5/114.15.2	Fluidigm	3209006B
Anti-mouse cytokeratin-7 clone RCK105	Abcam	Ab9021
Anti-mouse pan-cytokeratin clone C-11	Biolegend	628602
Anti-mouse VIM 154Sm clone D21H3	Fluidigm	3154014A
Anti-mouse RFP clone 8E5.G7	Rockland Inc	200-301-379
Anti-mouse DES clone Y66	Abcam	ab271829
Anti-mouse aSMA clone 1A4	Abcam	ab240654
Anti-human/mouse cleaved caspase-3 (CC3) clone D3E9	Cell Signaling Technology	9579
Anti-human/mouse Ki67 clone So1A15	Thermo Fisher	14-5698-82

(*Continued on next page*)

Continued

REAGENT or RESOURCE	SOURCE	IDENTIFIER
Anti-mouse collagen-4 pAb	Abcam	ab6586
Anti-mouse CD64 151Eu clone X54-5/7.1	Fluidigm	3151012B
Anti-mouse CD16/32 clone 93	Biolegend	101302
Anti-mouse CD11b clone M1/70	Biolegend	101202
Anti-mouse PDCA-1 clone 927	Biolegend	127002
Anti-mouse CD68 clone FA-11	Biolegend	137002
Anti-mouse Ly6G 141Pr clone 1A8	Fluidigm	3141008B
Anti-mouse Siglec-F clone E50-2440	BD Biosciences	552125
Anti-mouse PD-L1 clone 10F.9G2	Biolegend	124302
Anti-mouse F4/80 146Nd clone BM8	Fluidigm	3146008B
Anti-mouse CD3e clone 17A2	BD Biosciences	555273
Anti-mouse CD19 149Sm clone 6D5	Fluidigm	3149002B
Anti-mouse CD1d clone 1B1	Biolegend	123502
Anti-mouse CD11c clone N418	Biolegend	117302
Anti-mouse XCR1 clone ZET	Biolegend	148202
Anti-mouse TCRb clone H57-597	Biolegend	109202
Anti-mouse CD45 clone 30-F11	Biolegend	103102
Anti-mouse CX3CR1 clone SA011F11	Biolegend	149002
Anti-mouse CXCR2 clone SA044G4	Biolegend	149302
Anti-mouse CSF1R clone AFS98	Biolegend	135502
Anti-mouse CD40 clone HM40-3	Biolegend	102902
Anti-mouse CD103 clone 2E7	Biolegend	121402
Anti-mouse PD-L2 clone TY25	Biolegend	107202
Anti-mouse VISTA clone MIH63	Biolegend	150202
Anti-mouse SIRPa clone P84	Biolegend	144002
Anti-mouse IL-4Ra clone I015F8	Biolegend	144802
Anti-mouse CD206 169Tm clone C086C2	Fluidigm	3169021B
Anti-mouse CD49b 170Er clone HMa2	Fluidigm	3170008B
Anti-mouse CD80 171Yb clone 16-10A1	Fluidigm	3171008B
Anti-mouse CD86 172Yb clone GL1	Fluidigm	3172016B
Anti-mouse CD101 clone Moushi101	Biolegend	Custom order
Anti-mouse NKp46 clone 29A1.4	Biolegend	137602
Anti-mouse CD38 175Lu clone 90	Fluidigm	3175014B
Anti-mouse Ly-6C clone HK1.4	Biolegend	128002
Anti-mouse CD24 clone M1/69	Biolegend	101802
Anti-mouse Galectin-9 clone 9M1-3	Thermo Fisher	16-9116-85
Anti-mouse iNOS 161Dy clone CXNFT	Fluidigm	3161011B
Anti-mouse CXCR3 clone CXCR3-173	Biolegend	126502
Anti-mouse GITR 143Nd clone DTA1	Fluidigm	3143019B
Anti-mouse CD69 145Nd clone H1.2F3	Fluidigm	3145005B
Anti-mouse TIGIT clone 1G9	Biolegend	142102
Anti-mouse 4-1BB clone 17B5	Biolegend	106107
Anti-mouse CD27 150Nd clone LG.3A10	Fluidigm	3150017B
Anti-mouse LAG3 clone C9B7W	Biolegend	125202
Anti-mouse CD8a 153Eu clone 53-6.7	Fluidigm	3153012B
Anti-mouse CTLA4 154Sm clone UC10-4B9	Fluidigm	3154008B
Anti-mouse CD4 clone RM4-5	Biolegend	100506
Anti-mouse PD-1 159Tb clone 29F.1A12	Fluidigm	3159024B

(*Continued on next page*)

Continued

REAGENT or RESOURCE	SOURCE	IDENTIFIER
Anti-mouse CD62L 160Gd clone MEL-14	Fluidigm	3160008B
Anti-mouse TIM3 162Dy clone RMT3-23	Fluidigm	3162029B
Anti-mouse CD49b clone HMa2	Biolegend	103501
Anti-mouse OX40 clone OX-86	Thermo Fisher	14-1341-82
Anti-mouse KLRG1 clone 2F1	BD Biosciences	562190
Anti-mouse ICOS 168Er clone C398.4A	Fluidigm	3168024B
Anti-mouse CD39 clone 24DMS1	Thermo Fisher	14-0391-82
Anti-mouse SLAM clone TC15-12F12.2	Biolegend	115902
Anti-mouse CD25 clone PC61	Biolegend	102002
Anti-mouse CD127 174Yb clone A7R34	Fluidigm	3174013B
Anti-mouse TCRgd clone UC7-13D5	Biolegend	107502
Anti-mouse GATA3 clone L50-823	BD Biosciences	558686
Anti-mouse GZMB clone GB11	Thermo Fisher	MA1-80734
Anti-mouse TCF1 clone C63D9	Cell Signaling Technology	2203
Anti-mouse EOMES clone Dan11mag	Thermo Fisher	14-4875-82
Anti-mouse TBET 161Dy clone 4B10	Fluidigm	3160010B
Anti-mouse FOXP3 165Ho clone FJK-16s	Fluidigm	3165024A
Anti-RFP clone 8E5.G7	Rockland Inc	200-301-379
Anti-human/mouse pMARPKAPK2 [T334] clone 27B7	Cell Signaling Technology	3007
Anti-human/mouse pTAK1 [S412]	Cell Signaling Technology	9339
Anti-human/mouse pAMPKa [T172] clone 40H9	Cell Signaling Technology	2535
Anti-human/mouse pPLCg2 [Y759] 144Nd clone K86-689.37	Fluidigm	3144015A
Anti-human/mouse pFAK [S910] clone K73-480	BD Biosciences	Custom order
Anti-human/mouse pp90RSK [S380] clone D5D8	Cell Signaling Technology	12032
Anti-human/mouse B-catenin 147Sm clone D10A8	Fluidigm	3147005A
Anti-human/mouse pSTAT4 [Y693] 148Nd clone 38/p-Stat4	Fluidigm	3148006A
Anti-human/mouse p4EBP1 [T37/T46] 149Sm clone 236B4	Fluidigm	3149005A
Anti-human/mouse pSTAT5 [Y694] 150Nd clone 47/Stat5	Fluidigm	3150005A
Anti-human/mouse pGSK3B [S9] clone D85E12	Cell Signaling Technology	5558
Anti-human/mouse pAKT [S473] 152Eu clone D9E	Fluidigm	3152005A
Anti-human/mouse pSTAT1 [Y701] 153Eu clone 58D6	Fluidigm	3153003A
Anti-human/mouse pSMAD1/5/9 [S463]/465]/[S463/465]/[S465/467] clone D5B10	Cell Signaling Technology	13820
Anti-human/mouse p70S6K [T389] clone 1A5	Cell Signaling Technology	9206
Anti-human/mouse pp38 [T180/182] 156Gd clone D3F9	Fluidigm	3156002A
Anti-human/mouse pSTAT3 158Gd clone Y705	Fluidigm	3158005A

(*Continued on next page*)

Continued

REAGENT or RESOURCE	SOURCE	IDENTIFIER
Anti-human/mouse pMEK1/2 [S221] clone 166F8	Cell Signaling Technology	2338
Anti-human/mouse pAKT [T308] clone D25E6	Cell Signaling Technology	13038
Anti-human/mouse pSRC [Y418] clone SC1T2M3	Thermo Fisher	12-9034-82
Anti-human/mouse pMKK3/6 [S189]/[S207] clone D8E9	Cell Signaling Technology	12280
Anti-human/mouse cyclinB1 clone V152	Cell Signaling Technology	4135
Anti-human/mouse IkBa 164Dy clone L35A5	Fluidigm	3164004A
Anti-human/mouse pCREB [S133] 165Ho clone 87G3	Fluidigm	3165009A
Anti-human/mouse pJAK2 [Y1007/1008] clone E132	Abcam	ab219728
Anti-human/mouse pERK1/2 [T202]/[Y204] 167Er clone D1314.4E	Fluidigm	3167005A
Anti-human/mouse pIKKa/b [S176/180] clone 16A6	Cell Signaling Technology	2697
Anti-human/mouse pSMAD2/3 [S465/467]/ [S423/425] clone D27F4	Cell Signaling Technology	8828
Anti-human/mouse pNFkBp65 [S536] clone 92H1	Cell Signaling Technology	3033
Anti-human/mouse pMKK4 [S257] clone C36C11	Cell Signaling Technology	4514
Anti-human/mouse pRelB [S552] clone D41B9	Cell Signaling Technology	5025
Anti-human/mouse pPDK1 [S241] clone J66-653.44.22	BD Biosciences	558395
Anti-human/mouse pRB [S807/S811] clone J112-906	BD Biosciences	558389
Anti-human/mouse pS6 [S235/S236] (175Lu) clone N7-548	Fluidigm	3175009A
Anti-human/mouse pHH3 [S28] clone HTA28	Biolegend	641002
Anti-GFP clone FM264C	Biolegend	338002
Anti-mouse CD90 APC clone G7	Abcam	ab25322
Anti-mouse CD105 Biotin clone MJ7/18	Biolegend	120404
Anti-mouse ITGA1 PE clone HMa1	Biolegend	142604
Anti-mouse CD26 FITC clone H194-112	Biolegend	137806
Anti-mouse EpCAM FITC clone G8.8	Biolegend	118208
Anti-mouse CD45 FITC clone 30-F11	Biolegend	103108
Anti-mouse CD31 FITC clone MED13.3	Biolegend	102506
Anti-mouse PDPN APC clone 8.1.1	Biolegend	127410
Anti-mouse PDPN PE-Cy7 clone 8.1.1	Biolegend	127412
Anti-mouse CD90 PE clone G7	Abcam	ab24904
Anti-mouse CD105 BV421 clone MJ7/18	BD Biosciences	562760
Anti-mouse CD105 PE clone MJ7/18	Biolegend	120408
Anti-mouse CD105 PE-Cy7 clone MJ7/18	Biolegend	120410
Anti-mouse CD105 APC clone MJ7/18	Biolegend	120414
Anti-mouse CD74 AF647 clone In1/CD74	Biolegend	151004

(*Continued on next page*)

Continued

REAGENT or RESOURCE	SOURCE	IDENTIFIER
Anti-mouse MHCII PE-Cy7 clone M5/114.15.2	Biolegend	107630
Anti-mouse MHCII BV421 clone M5/114.15.2	Biolegend	107632
Anti-mouse CD90 AF746 clone 5E10	Biolegend	328116
Anti-mouse CD105 PE clone 43A3	Biolegend	323206
Anti-human pan-Cytokeratinp pAb	Abcam	ab9377
Anti-human PDPN clone D2-40	Agilent Dako	M361901-2
Anti-human CD105 clone 3A9	CST	14606
Anti-human VIM clone D21H3	CST	5741
Anti-mouse aSMA clone 1A4	Sigma Aldrich	A5228
Anti-GFP pAb	Abcam	ab13970
Goat anti-chicken IgG pAb	Abcam	ab207998
Bacterial and Virus Strains		
NEB 5-Alpha Competent *E. coli*	New England BioLabs Inc.	C2987I
Biological samples		
Human FFPE pancreatic ductal adenocarcinoma tumors	Manchester Cancer Research Centre (MCRC) Biobank	See Table S3
Human FFPE colorectal adenocarcinoma tumors	Manchester Cancer Research Centre (MCRC) Biobank	See Table S7
Human FFPE lung adenocarcioma tumors	Manchester Cancer Research Centre (MCRC) Biobank	See Table S7
Human FFPE mammary invasive ductal carcinoma tumors	Manchester Cancer Research Centre (MCRC) Biobank	See Table S7
Chemicals, peptides, and recombinant proteins		
Tris(2-carboxyethyl)phosphine hydrochloride (TCEP)	Thermo Fisher	77720
Yttrium chloride	Sigma Aldrich	204919
Lanthanum chloride	Sigma Aldrich	203521
194-Pt monoisotopic cisplatin	Fluidigm	201194
195-Pt monoisotopic cisplatin	BuyIsotope	Custom order
196-Pt monoisotopic cisplatin	BuyIsotope	Custom order
198-Pt monoisotopic cisplatin	Fluidigm	201198
157Gd isotopically enriched gadolinium chloride	Trace Sciences	Quote
105Pd isotopically enriched palladium nitrate	Trace Sciences	Quote
106Pd isotopically enriched palladium nitrate	Trace Sciences	Quote
108Pd isotopically enriched palladium nitrate	Trace Sciences	Quote
110Pd isotopically enriched palladium nitrate	Trace Sciences	Quote
113In isotopically enriched indium chloride	Trace Sciences	Quote
115In isotopically enriched indium chloride	Trace Sciences	Quote
5-iodo-2'-deoxyuridine (IdU)	Sigma Aldrich	17125
Sodium hydroxide (NaOH)	Sigma Aldrich	757527
Ammonium Acetate (NH4CH3CO2)	Sigma Aldrich	372331
Heparin Sodium Salt	Sigma Aldrich	H3393
DMSO	Sigma Aldrich	D2650
Sodium Azide	Sigma Aldrich	S8032

(*Continued on next page*)

Continued

REAGENT or RESOURCE	SOURCE	IDENTIFIER
Collagenase Type IV	Thermo Fisher	17104019
DNase1	Sigma Aldrich	10104159001
Hyaluronidase	Sigma Aldrich	H3757
Dispase II	Thermo Fisher	17105041
FOXP3 Fixation/Permeabilization Kit	Thermo Fisher	00-5523-00
16% Paraformaldehyde (PFA)	Thermo Fisher	28908
EQ Four Element Calibration Beads	Fluidigm	201078
Cell-ID 125 uM Iridium Intercalator	Fluidigm	201192A
3% hydrogen peroxide	VWR	23614.291P
Casein	Vector	SP5020
Tris Buffer Saline with Tween 20 (TBST)	VWR	J77500.K8
HyClone Antibiotic/Antimycotic	Fisher Scientific	11536481
Accutase Cell Detachment Solution	Sigma Aldrich	A6964
Epitope Retrieval Solution 1 (ER1)	Leica Microsystems	AR9961
Research Detection System 2	Leica Microsystems	DS9777
Bond Antibody Diluent	Leica Microsystems	AR9352
EnVision HRP	Agilent	K4001/4003
Premixed TSA520 Reagent	Perkin Elmer	FP1487001KT
Premixed TSA570 Reagent	Perkin Elmer	FP1488001KT
Premixed TSA650 Reagent	Perkin Elmer	FP1496001KT
4′,6-diamidino-2-phenylindole (DAPI)	Thermo Fisher	62248
ProLong Gold Antifade Mountant	Thermo Fisher	P36930
RBS Lysis Buffer	Biolegend	420301
0.5 M EDTA	Thermo Fisher	15575020
Live/Dead Fixable Near-IR Dead Cell Stain Kit	Thermo Fisher	L10119
Primocin	InvivoGen	ant-pm-1
DMEM with glucose and L-glutamine	Thermo Fisher	41966052
Bovine Serum Albumin (BSA)	Sigma Aldrich	A3294
Fetal Bovine Albumin (FBS)	Thermo Fisher	10270106
Lipofectamine2000	Thermo Fisher	11668019
Optimem Reduced Serum Media	Thermo Fisher	31985070
Polybrene	Sigma Aldrich	107689
Puromycin	Sigma Aldrich	P8833
Polyethylenimine (PEI)	Sigma Aldrich	764647
Universal Mouse Reference RNA	Thermo Fisher	QS0640
Reverse Transcription Buffer	Thermo Fisher	18067017
Mg_2Cl_2	Thermo Fisher	R0971
dNTP Mix	Thermo Fisher	R0191
DL-Dithiothreitol (DTT)	Sigma Aldrich	43815
RNAse Inhibitor	Thermo Fisher	N8080119
Random Hexamers	Thermo Fisher	N8080127
Multiscribe Reverse Transciptase	Thermo Fisher	4311235
TaqMan Pre-Amp Master Mix	Applied Biosystems	4391128
RNAse-free water	Thermo Fisher	10977035
Assay Loading Reagent	Fluidigm	85000736
TaqMan Universal PCR Master Mix	Applied Biosystems	4304437
GE Sample Loading Reagent	Fluidigm	85000746
Hygromycin B	Thermo Fisher	10687010

(*Continued on next page*)

Continued

REAGENT or RESOURCE	SOURCE	IDENTIFIER
1,4,7,10-tetraazacyclododecane-1,4,7-tris-acetic acid-10-maleimidoethylacetamide (mDOTA)	Macrocyclics	B-272
Methanol	Fisher Scientific	10767665
Bis(2,2′-bipyridine)-4′-methyl-4-carboxybipyridine-ruthenium *N*-succinimidyl ester-bis(hexafluorophosphate) (ASCQ_Ru)	Sigma Aldrich	96631
Sodium Bicarbonate (NaHCO3)	Sigma Aldrich	31437
Phosphate-Buffered Saline (for *in vivo*)	Thermo Fisher	10010056
Growth Factor Reduced Matrigel	Corning	356231
Neutral Buffered Formalin	Genta Medical	BIB10L
Low pH Target Retrieval Buffer Ph6	Agilent	S236984
Vectastain Elite ABC HRP Kit	Vector	PK-6100
3,3'-diaminobenzidine (DAB)	Agilent	K3467
Shandon Gill Haematoxylin	Thermo Fisher	6765005
Primary Cell P3 Nucleofector solution	Lonza	V4XP-3032
Electroporation Enhancer Solution	Integrated DNA Technologies	Alt-R Cas9 Electroporation Enhancer, 2 nmol
PBS-based Antibody Stabilization Buffer	Candor Biosciences	13150
Maxpar water (for mass cytometry)	Fluidigm	201069
Phosphate-Buffered Saline (PBS) (for mass cytometry)	Fisher Scientific	10091403
Recombinant Cas-9	Integrated DNA Technologies	1081059
Recombinant mouse TGFB1	RnD Systems	7666-MB-005
Recombinant rat PDGF-BB	RnD Systems	520-BB-050
Recombinant mouse FGF2	RnD Systems	3139-FB-025
Recombinant human/mouse Activin-A	RnD Systems	338-AC-010
Recombinant mouse BMP2	RnD Systems	355-BM-010
Recombinant mouse BMP4	RnD Systems	5020-BP-010
Recombinant mouse BMP9	RnD Systems	5566-BP-010
Recombinant mouse MIF	Biolegend	599504
Recombinant mouse IFNg	PeproTech	315-05
Recombinant mouse TNFa	Peprotech	315-01A
Recombinant mouse IL1a	RnD Systems	400-ML-005
Recombinant mouse IL1b	PeproTech	211-11B
Recombinant mouse IL4	PeproTech	AF-214-14
Recombinant mouse IL13	RnD Systems	413-ML-005
Recombinant mouse IL22	RnD Systems	582-ML-010
Recombinant mouse LIF	PeproTech	250-02
Recombinant mouse BMP7	RnD Systems	5666-BP-010
Recombinant mouse BMP10	RnD Systems	6038-BP-025
Recombinant mouse IL6	PeproTech	216-16
Critical commercial assays		
MaxPar X8 Antibody Conjugation Kits (various metals)	Fluidigm	Mutiple e.g. 141Pr 201141A
Cell-ID 20-plex Pd Barcoding Kit	Fluidigm	201060
TruSeq Small RNA Library Kit	Illumina Inc.	200-0012
Agilent SureSelect Strand Specific RNA Library Prep Kit for Illumina Sequencing	Agilent	G9691B

(*Continued on next page*)

Continued

REAGENT or RESOURCE	SOURCE	IDENTIFIER
Kapa Library Quantification Kit for Illumina Sequencing Platforms	Kapa Biosystems Inc.	KK4835
Illumina HighSeq 500 High Output 1x75 bp Kit	Illumina Inc.	200-24906
RNeasy Micro Kit	QIAGEN	74004
RNeasy Mini Kit	QIAGEN	74104
QIAGEN Plasmid Midi Kit	QIAGEN	12145X4
96x96 Dynamic Array Chip	Fluidigm	
Deposited data		
Mouse Pancreatic Tumor scRNA-seq dataset GSE129455	Elyada et al.	GEO accession: GSE129455
Human Pancreatic Tumor scRNA-seq dataset	Steele et al.	GEO accession: GSE155698
Mouse *in vitro* Pancreatic Fibroblast (PaF) scRNA-seq raw data.	This paper	https://doi.org/10.5281/zenodo.4584773
Mouse PDA CAF bulk RNA-seq dataset	This paper	GEO accession: GSE156985
Mouse *in vitro* Pancreatic Fibroblast (PaF) bulk RNA-seq datset (various stimulations)	This paper	GEO accession: GSE157391
Mouse *in vitro* Pancreatic Fibroblast (PaF) and Liver Fibroblast (LiF) bulk RNA-seq datset	This paper	GEO accession: GSE176057
Mouse subcut CD105pos and CD105neg PaF co-transplant day 10 bulk RNA-seq dataset	This paper	GEO accession: GSE176056
Mouse PDA mass cytometry dataset - Mesenchymal Stroma (S) panel. Raw data	This paper	https://doi.org/10.5281/zenodo.4584773
Mouse PDA mass cytometry dataset - Myeloid/NK/B (MNB) cell panel. Raw data	This paper	https://doi.org/10.5281/zenodo.4584773
Mouse PDA mass cytometry dataset - T cell panel. Raw data	This paper	https://doi.org/10.5281/zenodo.4584773
Mouse *in vitro* Pancreatic Fibroblast (PaF) mass cytometry dataset - Mesenchymal Stroma (S) panel. Raw data	This paper	https://doi.org/10.5281/zenodo.4584773
Mouse *in vitro* Pancreatic Fibroblast (PaF) mass cytometry dataset - Cell Signalling panel. Raw data	This paper	https://doi.org/10.5281/zenodo.4584773
Mouse multi-organ *in vitro* primary fibroblast mass cytometry dataset - Mesenchymal Stroma (S) panel. Raw data	This paper	https://doi.org/10.5281/zenodo.4584773
Mouse multi-GEMM mass cytometry dataset - Mesenchymal Stroma (S) panel. Raw data	This paper	https://doi.org/10.5281/zenodo.4584773
Experimental models: Cell lines		
Mouse PDA B6KPC-TB32043 (PDA#1)	Gift from Dr. Kris Frese, CRUK MI, UK	
Mouse PDA B6KPC-TB32047 (PDA#2)	Gift from Dr. Kris Frese, CRUK MI, UK	
B6 CD105+ Pancreatic Fibroblasts (PaFs)	This paper	
B6 CD105- Pancreatic Firoblasts (PaFs)	This paper	
Phoenix Cells	ATCC (Pear et al., 1993)	Thermo Fisher
HEK293FT	Thermo Fisher	R70007
Human Primary Pancreatic Fibroblasts (hPaFs)	Generon	H-6201

(*Continued on next page*)

Continued

REAGENT or RESOURCE	SOURCE	IDENTIFIER
B6 primary mouse embryonic fibroblasts (MEFs)	Generon	C57-6028
Experimental models: Organisms/strains		
Pdx1-Cre; Kras$^{LSL-G12D/+}$; Trp53$^{LSL-R172H/+}$(KPC)	Hingorani et al. (2005)	
Pdx1-Cre; Kras$^{LSL-G12D/+}$;Trp53$^{LSL-R172H/+}$; Rosa26$^{LSL-tdRFP/LSL-tdRFP}$(RFP KPC)	Luche et al. (2007)	
C57BL/6JOlaHsd (B6)	Envigo	
NOD-scid.*Il2rg$^{-/-}$* (NSG)	Charles River	
B6.*Rag1$^{-/-}$* (RAG1)	Mombaerts et al. (1992)	
B6.*Batf3$^{-/-}$*(BATF3)	Hildner et al. (2008)	
B6.*Villin::CreER; Kras$^{LSL-G12D/+}$; Trp53$^{fl/fl}$; Rosa26$^{Notch1icd/}$*(KPN)	Jackstadt et al. (2019)	
MMTV-PyMT (MMTV-PyMT)	Guy et al. (1992)	
B6.*Kras$^{LSL-G12D/+}$; Trp53$^{fl/fl}$* (KP)	Jackson et al. (2001), Marino et al. (2000)	
B6.*Tyr::CreER; Braf$^{LSL-V600E/+}$* (BRAF^{V600E})	Dhomen et al. (2009)	
Oligonucleotides		
RT-QPCR primer for *Actb*: forward, 5'-aaggccaaccgtgaaaagat-3'	Sigma Aldrich	
RT- QPCR primer for *Actb*: reverse, 5'-gtggtacgaccagaggcatac-3'	Sigma Aldrich	
RT- QPCR primer for *Gapdh*: forward, 5'-gggttcctataaatacggactgc-3'	Sigma Aldrich	
RT-QPCR primer for *Gapdh*: reverse, 5'-ccattttgtctacgggacga-3'	Sigma Aldrich	
RT-QPCR primer for *Pgk1*: forward, 5'-tacctgctggctggatgg-3'	Sigma Aldrich	
RT-QPCR primer for *Pgk1*: reverse, 5'-cacagcctcggcatatttct-3'	Sigma Aldrich	
RT-QPCR primer for *Ppia*: forward, 5'-gccaccctccctaactgc-3'	Sigma Aldrich	
RT-QPCR primer for *Ppia*: reverse, 5'-gcgggctcctactagatggt-3'	Sigma Aldrich	
RT-QPCR primer for *Tbp*: forward, 5'-ggcggtttggctaggttt-3'	Sigma Aldrich	
RT-QPCR primer for *Tbp*: reverse, 5'-gggttatcttcacacaccatga-3'	Sigma Aldrich	
RT-QPCR primer for *Tubb4a*: forward, 5'-gacctatcatggggacagtga-3'	Sigma Aldrich	
RT-QPCR primer for *Tubb4a*: reverse, 5'-cggctctgggaacatagttt-3'	Sigma Aldrich	
RT-QPRC primer for *Acta2*: forward, 5'-ctctcttccagccatctttcat-3'	Sigma Aldrich	
RT-QPCR primer for *Acta2*: reverse, 5'-tataggtggtttcgtggatgc-3'	Sigma Aldrich	
RT-QPCR primer for *Col1a1*: forward, 5'-caggcaagcctggtgaac-3'	Sigma Aldrich	
RT-QPCR primer for *Col1a1*: reverse, 5'-aacctctctcgcctcttgc-3'	Sigma Aldrich	
RT-QPCR primer for *Ctgf*: forward, 5'-tgacctggaggaaaacattaaga-3'	Sigma Aldrich	

(*Continued on next page*)

Continued

REAGENT or RESOURCE	SOURCE	IDENTIFIER
RT-QPCR primer for *Ctgf*: reverse, 5'-agccctgtatgtcttcacactg-3'	Sigma Aldrich	
RT-QPCR primer for *Fndc1*: forward, 5'-tggtcctcaaggaacaaagtg-3'	Sigma Aldrich	
RT-QPCR primer for *Fndc1*: reverse, 5'-ttctgcattcaacaccaagc-3'	Sigma Aldrich	
RT-QPCR primer for *Il6*: forward, 5'-gctaccaaactggatataatcagga-3'	Sigma Aldrich	
RT-QPCR primer for *Il6*: reverse, 5'-ccaggtagctatggtactccagaa-3'	Sigma Aldrich	
RT-QPCR primer for *Cxcl1*: forward, 5'-gactccagccacactccaac-3'	Sigma Aldrich	
RT-QPCR primer for *Cxcl1*: reverse, 5'-tgacagcgcagctcattg-3'	Sigma Aldrich	
RT-QPCR primer for *Ccl2*: forward, 5'-catccacgtgttggctca-3'	Sigma Aldrich	
RT-QPCR primer for *Ccl2*: reverse, 5'-gatcatcttgctggtgaatgagt-3'	Sigma Aldrich	
RT-QPCR primer for *Csf3*: forward, 5'-ccaccttggacttgcttcag-3'	Sigma Aldrich	
RT-QPCR primer for Csf3: reverse, 5'-ccacccctaggttttccatc-3'	Sigma Aldrich	
sgRNA Scrambled non-targeting: 1, 5'-gcacuaccagagcuaacuca-3'	Synthego	
sgRNA Scrambled non-targeting: 2, 5'-guacgucgguauaacuccuc-3'	Synthego	
sgRNA *Eng*: 1, 5'-cucuuuc ugcgagaccugcu-3'	Synthego	
sgRNA *Eng*: 2, 5'-cggcugugaucuacagccug-3'	Synthego	
sgRNA *Eng:* 3, 5'-ucaccc cuuuguggguccac-3'	Synthego	
sgRNA *H2Ab1*: 1, 5'-ucucau ccacacagcuuauu-3'	Synthego	
sgRNA *H2Ab1*: 2, 5'-gaacc agcgcacuuugaucu-3'	Synthego	
sgRNA *H2Ab1*: 3, 5'-ugagg gccucuguccuggac-3'	Synthego	
sgRNA *Cd74*: 1, 5'-auuuc ggaagcuucaugcga-3'	Synthego	
sgRNA *Cd74*: 2, 5'-uuacuu ccuguaccagcaac-3'	Synthego	
sgRNA *Cd74*: 3, 5'-ugagg gccucuguccuggac-3'	Synthego	
sgRNA *Cd80*: 1, 5'-ggaca uggaaacuugaggag-3'	Synthego	
sgRNA *Cd80*: 2, 5'-cgucuu ucacaaagugcuuc-3'	Synthego	
sgRNA *Cd80*: 3, 5'-uaagcucg cuggguuuuga-3'	Synthego	
Recombinant DNA		
pBABE-puro SV40 LT plasmid	Addgene	13970
pCL-Eco plasmid	Addgene	12371
SFFV-eGFP plasmid	Harris et al. (2012)	

(*Continued on next page*)

Continued

REAGENT or RESOURCE	SOURCE	IDENTIFIER
SFFV-mCherry plasmid	Harris et al. (2012)	
pCMV delta R8.2 packaging plasmid	Addgene	12263
pMD2.G envelope plasmid	Addgene	12259
pCSII-IRES2-hygro hTERT plasmid	Gift from Dr. Fernando Calvo, Institute of Cancer Research (ICR), UK	
Software and algorithms		
FCS Normalization Tool	Fluidigm	
FCS Normalization Tool	Zunder et al. (2015)	
www.cytobank.org	Beckman Coulter	
Cytofkit2	https://github.com/JinmiaoChenLab/cytofkit2	
FlowSOM (Cytofkit2 implemnation)	Van Gassen et al. (2015)	
UMAP (Cytofkit2 implementation)	Becht et al. (2018)	
Qu-Path (v0.2.0-m9)	Bankhead et al. (2017)	
FASTQC tool (version 0.11.3)	https://github.com/s-andrews/FastQC	
STAR aligner (version 2.5.1b)	https://github.com/alexdobin/STAR	
Rsubread (version 1.28.1)	https://bioconductor.org/packages/release/bioc/html/Rsubread.html	
DESeq2 (version 3.10)	https://bioconductor.org/packages/release/bioc/html/DESeq2.html	
Ingenuity Pathway Analysis (Dec 2020). Qiagen Digital Insights	https://digitalinsights.qiagen.com	
Seurat (version 3.1.5)	https://github.com/satijalab/seurat	
BioMark Real-Time PCR Analysis Software	Fluidigm	
GraphPad Prism software (version 7)	GraphPad Software Inc	
ComplexHeatmap	https://bioconductor.org/packages/release/bioc/html/ComplexHeatmap.html	
flowCore	https://www.bioconductor.org/packages/release/bioc/html/flowCore.html	
FlowJo (version 10.6.2)	BD LifeSciences	
Corrplot	https://github.com/taiyun/corrplot	
MCPcounter	https://github.com/ebecht/MCPcounter	
Other		
GentleMACS Octo Dissociator	Miltenyi Biotech	
Helios Mass Cytometer	Fluidigm	
Super Sampler	Victorian Airship & Scientific Apparatus LLC	
BOND RX automated platform	Leica Microsystems	
VS120 microscope	Olympus Lifescience	
SCN400	Leica microsystems	
BD FACS AriaIII	BD Biosciences	
BD LSRFortessa	BD Biosciences	
Vevo 3100 Imaging System	Fujifilm VisualSonics	
NextSeq 500 Sequencer	Illumina Inc.	
4D-Nucleofector Core Unit	Lonza	
Nucleocuvette kit/strip	Lonza	V4XP-3032
Nanodrop One/One Spectrophotometer	Thermo Fisher	
Luna Cell Counter	Logosbio	
Alpha 2-4 Benchtop Lyopholiser	MartinChrist Freeze Dryers	
C-tubes	Miltenyi Biotech	130-096-334

(*Continued on next page*)

Continued

REAGENT or RESOURCE	SOURCE	IDENTIFIER
50 kDa Microfilters	Merck Millipore	UFC505096
3 kDa Microfilters	Merck Millipore	UFC500324
Braun Omnican 50 Insulin Syringe/Needles	VWR	9151117

RESOURCE AVAILABILITY

Lead contact

Further information and requests for resources and reagents should be directed to and will be fulfilled by the lead contact, Claus Jørgensen (claus.jorgensen@cruk.manchester.ac.uk)

Materials availability

This study did not generate new unique reagents.

Data and code availability

Bulk RNA-seq data are avaliable at NCBI under GEO accession numbers GSE129455, GSE155698, GSE156985, GSE157391, GSE176056 and GSE176057. Mass cytometry and scRNA-seq data is available on Zenodo at https://doi.org/10.5281/zenodo.4584773.

This paper does not report original code

Any additional information required to re-analyze the data reported in this paper is available from the lead contact upon request.

EXPERIMENTAL MODELS

Animal models

Pdx1-Cre; Kras$^{LSL\text{-}G12D/+}$*; Trp53*$^{LSL\text{-}R172H/+}$ (KPC) mice (Hingorani et al., 2005); 'RFP KPC' mice were generated by crossing KPC and *Rosa26*$^{LSL\text{-}tdRFP/LSL\text{-}tdRFP}$ mice (Luche et al., 2007); B6.*Villin::CreER; Kras*$^{LSL\text{-}G12D/+}$*; Trp53*$^{fl/fl}$*; Rosa26*$^{Notch1icd/+}$ (KPN) mice (Jackstadt et al., 2019); B6.*Kras*$^{LSL\text{-}G12D/+}$*; Trp53*$^{fl/fl}$ ('KP') mice were generated by crossing B6.*Kras*$^{LSL\text{-}G12D/+}$ mice (Jackson et al., 2001) and B6.*Trp53*$^{fl/fl}$ mice (Marino et al., 2000); B6.*Tyr::CreER; Braf*$^{LSL\text{-}V600E/+}$ (BRAF^{V600E}) mice (Dhomen et al., 2009) were generated by crossing B6.*Tyr::CreER* (Mercer et al., 2005) and B6.*Braf*$^{LSL\text{-}V600E/+}$ mice (Yajima et al., 2006); *MMTV-PyMT* mice (Guy et al., 1992); B6.*Rag1*$^{-/-}$ mice (Mombaerts et al., 1992) and B6.*Batf3*$^{-/-}$ mice (Hildner et al., 2008). Animals were bred and maintained under pathogen-free conditions at University of Manchester and CRUK Beatson Institute (CRUK-BI), University of Glasgow. Female C57BL/6 (B6) mice were purchased from Envigo and used at ages specified for each experiment. Female NOD-scid.*Il2rg*$^{-/-}$ (NSG) mice were purchased from Charles River and used at 14 weeks of age. All animal experiments were performed under a UK Home Office License and in accordance with the 'Animal (Scientific Procedures) Act of 1986' under Project License Number 70/8745 and 70/8375 subject to review by the Animal Welfare and Ethical Review Body of Cancer Research UK Manchester Institute, University of Manchester (CRUK MI) and the University of Glasgow (UoG). Experiments are reported in accordance with Animal Research: Reporting of In Vivo Experiments (ARRIVE) 2.0 guidelines.

Human tissue samples

Formalin fixed paraffin embedded (FFPE) human pancreatic ductal adenocarcinoma, colorectal adenocarcinoma, mammary invasive ductal carcinoma and lung adenocarcinoma tumor samples were obtained with informed patient consent by the Manchester Cancer Research Centre (MCRC) Biobank in accordance with the Human Tissue Act 2004 (13_RIMA_04). The MCRC Biobank (ethics code: 18/NW/0092) is licensed by the Human Tissue Authority (license number: 30004) and is ethically approved as a research tissue bank by the South Manchester Research Ethics Committee (Ref: 07/H1003/161+5). The role of the MCRC Biobank is to distribute samples. For more information see www.mcrc.manchester.ac.uk/Biobank/Ethics-and-Licensing.

Cell lines and culture

To limit culture-induced phenotypic changes, all cells were used within one month of thawing and the same frozen batch used for all experiments when possible. All cell lines were regularly tested for mycoplasma infection. Primary pancreatic fibroblasts (PaFs) were expanded *in vitro* from the pancreas of 8-week-old female B6 mice, were never allowed to become confluent and were detached for splitting using Accutase Dissociation Solution. The murine PDA cancer cell lines used in this study (designated as 'PDA' and 'PDA#2' in the manuscript) are BL6KPC-TB32043 and BL6KPC-TB32047 and on a B6 background and were a kind gift from Dr. Kris Frese at CRUK MI. All cells were cultured in Cell Culture Media 10% (CCM(10)), consisting of 10% v/v FBS and 1% v/v HyClone Antibiotic/Antimycotic in DMEM with glucose and L-glutamine.

METHODS DETAILS

Mass cytometry antibody conjugation

Supplier, clone and heavy-metal isotope tag of each mass cytometry antibody used in this study are listed in the Supplemental Information Table. Where possible targets were placed in higher sensitivity channels with minimal spill over from more abundant channels. The dedicated panel builder at dvssciences.com was used to estimate isotope and oxide spill-over and guide channel selection. Particular antibody clones were selected based on widespread use and extensive evidence of specific staining in the literature or from our own flow cytometry analysis. Where indicated antibodies were purchased pre-conjugated (Fluidigm). All other antibodies were purchased in carrier protein-free format and labelled with the indicated heavy-metal tag using Maxpar X8 Antibody Conjugation Kits (Fluidigm) (Han et al., 2018). 200 μg of each antibody was washed twice with 400 μL R buffer (Fluidigm) in a 50 kDa Microfilter (Merck Millipore, UFC505096) by centrifuging at 12,000 g at room temperature (RT) for 6 minutes. Antibodies were partially reduced using 200 μL of a 4 mM solution of tris(2-carboxyethyl)phosphine hydrochloride (TCEP) (Thermo Fisher, 77720) in R-buffer. After 25 min of TCEP reduction, antibodies were washed twice with C-buffer (Fluidigm). In parallel to antibody reduction, metal chelation was performed by adding 10ul of 50 μM lanthanide metal solutions to two equivalents of Maxpar X8 chelating polymer (Fluidigm) in 190 μL of L-buffer (Fluidigm) and incubating for 1 h at RT. The metal loaded polymers were washed once with L-buffer then once with C-buffer in 3 kDa Microfilters (Merck Millipore, UFC500324), by centrifuging at 12,000 g for 20 min. The metal loaded polymer in C-buffer was added to the partially reduced antibody and incubated at 37°C for 1.5 h. Conjugated antibodies were washed six times with W-buffer (Fluidigm), suspended in 100 μL W-buffer, vortexed and left for 5 min at RT before being reverse centrifuged into a fresh 1.6 mL collection tube. Protein content was assessed using a Nanodrop One/One Spectrophotometer (Thermo Fisher) and then 300 μL of PBS-based Antibody Stabilization Buffer (Candor Biosciences, 13150) containing 0.6 mg/mL sodium azide (Sigma Aldrich, S8032) was added and the conjugated antibodies stored at 4°C. To generate cisplatin conjugates, 200 μg of antibody was reduced as described above and incubated with 200 μL of 400 μM monoisotopic cisplatin (BuyIsotope, custom order) in C-buffer at 37°C for 1.5 h and washed and stored as for the polymer/lanthanide conjugates. For any antibody that showed low final protein content (<40% recovery), the process was repeated but with a 10 min TCEP reduction. If significant degradation was still observed, an alternative antibody clone was tested or the target was not included in the panel. Antibodies were titrated in panels by staining samples of known positive and negative controls. See Supplemental Information Table for Panels.

Tumor disaggregations

Buffers and reagents used in tissue processing and cell staining were checked for heavy-metal ion contamination, particularly barium contamination, and buffers were made up in non-glass containers that had not been detergent washed. 5-iodo-2'-deoxyuridine (IdU) (Sigma Aldrich, 17125) was solubilized overnight at RT under mixing, in a minimally basic solution of 0.01 M sodium hydroxide (NaOH) (Sigma Aldrich, 757527) in water, to 10 mg/mL concentration and filtered through a 0.22 μm pore mesh. To label cells in S-phase for mass cytometry studies, mice were injected intraperitoneally with 200 μL of IdU solution 2 h before the mouse was culled by Schedule 1 method and tissues collected. Tumor samples were quickly transferred into ice-cold phosphate-buffered saline (PBS) (Fisher Scientific, 10091403) on ice. All non-tumor tissue that was attached to the outer edge of the denser tumor core was removed, the surface of the tumor samples was carefully dried with sterile paper and tumor weight recorded. Samples were washed once with ice-cold RPMI media and minced with disposable scalpels in 2 mL of disaggregation buffer (DB), consisting of 2 mg/mL Collagenase Type IV (Thermo Fisher, 17104019), 1 mg/mL DNase1 (Sigma Aldrich, 10104159001) and 0.5 mg/mL Hyaluronidase (Sigma Aldrich, H3757) in RPMI. Tumor pieces less than 3 mm in length were transferred to a C-tube (Miltenyi Biotech, 130-096-334) and a further 3 mL of DB added. If tumors were >600 mg, the disaggregation was carried out in two C-tubes, each with a total of 5 mL DB. The C-tube was placed in a GentleMACS Octo Dissociator (Miltenyi Biotech), heating blocks fitted and tumors disaggregated using the automated 37C_m_TDK1 program. Once complete, the C-tube was centrifuged at 100 g for 2 min, to ensure the contents were gathered at the bottom of the tube. The sample was diluted with a further 5 mL of fresh and warmed DB, mixed well by pipetting and filtered into a 50 mL tube through a 70 μm strainer, which was then washed with 10 mL ice-cold RPMI to quench the digestion. The single cell suspension was pelleted at 300 g for 6 min and used for mass or flow cytometry staining.

Mass cytometry live/dead and extracellular staining

All cell pelleting was conducted using a swinging bucket centrifuge, with the braking speed reduced to avoid disruption to the cell pellet. Aspirations were done carefully and always left at least 50 μL of void volume above the pellet. Live cells were spun at 300 g for 6 min and fixed cells spun at 1000 g for 6 min. Particular care was taken during PBS-only washes to ensure that cells had pelleted completely. The disaggregated tumor cell pellet was resuspended in 300 μL of ice-cold PBS, vortexed well and 300 μL of 1 μM 198Pt monoisotopic cisplatin (Fluidigm, 201198) in PBS added, followed by vortexing. After exactly 1 min incubation, the staining was quenched with 20 mL of CSM-E (Cell Staining Buffer – Extracellular) consisting of 5 mg/ml Bovine Serum Albumin (BSA) (Sigma Aldrich, A3294), 0.5% v/v Fetal Bovine Albumin (FBS) (Thermo Fisher, 10270106) and 0.2 mg/mL DNAse1 in PBS. The cells were resuspended and counted using a Luna Cell Counter (Logosbio) on fluorescence mode. The propidium iodide and acridine orange staining allows for improved cell counting of disaggregated tissues compared with trypan blue-based methods. $3x10^6$ cells were aliquoted into a 5 mL polypropylene FACS tube, washed with 3 mL CSM-E and pelleted. 20 μL of 100 U/mL heparin sodium salt (Sigma Aldrich, H3393) solution in PBS and 1 μL Fc block (BD Biosciences, 558636) was added. The contents were mixed by gentle rocking but no vortexing and incubated on ice for 5 min. A master mix of fluorophore-conjugated antibodies (see Supplemental Information

Table) in 50 μL CSM-E was added, mixed by gentle rocking and incubated on ice in the dark. After 20 min the mixture was vortexed. After a total incubation of 45 min, the cells were washed once with 4 mL of CSM-E. A master mix of extracellular targeting, metal-conjugated antibodies (see Supplemental Information Table) in 50 μL of CSM-E was added, mixed by gentle rocking and incubated on ice in the dark. After 20 min the mixture was vortexed. After a total incubation of 45 min, the cells were washed twice with 4 mL of CSM-E. The cell pellet was resuspended in 100 μL of PBS and vortexed and 1 mL of FOXP3 Fixation/Permeabilization Kit (Thermo Fisher, 00-5523-00), 1x FOXP3 Fixation Buffer added, followed by thorough vortexing. After 30 min incubation at RT, 2 mL of 1x FOXP3 Permeabilization Buffer was added and the cells pelleted. The cell pellet was resuspended in 1 mL of 10% v/v DMSO (Sigma Aldrich, D2650) in CSM-I (Cell Staining Buffer – Intracellular), consisting of 5 mg/ml BSA and 0.2 mg/ml sodium azide in PBS, vortexed and frozen at -80°C. For staining the sample with the Myeloid/NK/B cell (MNB) panel, no extracellular Fc block was used. Instead, the cells were incubated with heparin solution for 5 min, followed by metal-conjugated anti-CD64 antibody for 10 min on ice, followed by metal-conjugated anti-CD16/32 antibody for 5 min on ice, before adding the remaining master mix of extracellular antibodies. This ensured strong metal labelling of Fc-receptors, which contributed to accurate sub-setting of the mononuclear phagocyte lineage.

Mass cytometry barcoding and intracellular staining

Once the samples for an entire study had been collected, all the frozen aliquots were allowed to thaw at RT and washed once with 4 mL PBS. Each of the cell pellets were resuspended in a unique barcoding aliquot from the Cell-ID 20-plex Pd Barcoding Kit (Fluidigm, 201060) in 1 mL of cold PBS, vortexed and incubated at RT for 15 min. After the incubation, the mixtures were diluted in 3 mL of CSM-I, pelleted and washed once more with 4 mL CSM-I. Each of the cell pellets from the samples to be included in the study were resuspended in 200 μL of 1x FOXP3 Permeabilization Buffer, pooled into a 5 mL polypropylene FACS tube and pelleted. For each sample included in the pooled sample, 10 μL of 100 U/mL heparin sodium salt in PBS and 0.5 μL of Fc block was added and the sample mixed by gently rocking. After incubating for 5 min at RT in the dark, a master mix of intracellular targeting, metal-conjugated antibodies (see Supplemental Information Table) in CSM-I was added. For each sample included in the pooled sample, one equivalent of antibody and 25 μL of CSM-I was used and scaled up as required. The sample was mixed by gentle rocking and incubated on ice in the dark. After 20 min the mixture was vortexed. After a total incubation of 45 min the cells were washed twice with 4 mL of CSM-I. The cell pellet was resuspended in 1 mL of PBS and vortexed well. For every individual sample included in the pooled sample, a minimum of 500 μL of 4% Paraformaldehyde (PFA) (Thermo Fisher, 28908) in PBS was added to ensure complete fixation, using larger tubes as needed. If during sample acquisition, the heavy-metal markers are seen to 'streak', this is an indication the cells were not sufficiently fixed at this stage. The sample was vortexed and stored overnight at 4°C in the dark.

Mass cytometry DNA staining and acquisition

On the day of acquisition, 0.5 μL of 125 μM of Cell-ID Iridium Intercalator (Fluidigm, 201192A) was added per individual sample included and vortexed well. After 1 h of incubation at RT the cells were washed once with PBS and aliquoting to allow staggered acquisition. Typically, a pooled sample containing >15 individual samples was stored as x4 cell pellets, each prepared just before acquisition. Each cell pellet was washed twice with water and resuspended at a concentration of $1x10^6$ cells/mL in 15% EQ Four Element Calibration Beads (Fluidigm, 201078) in water, filtered twice through 70 μm Filcons (BD Biosciences, 340633) and acquired on a Helios Mass Cytometer (Fluidigm), using a Super Sampler (Victorian Airship & Scientific Apparatus LLC) to improve the consistency of sample delivery. The sample was acquired at a maximum of 500 events/s and sample lines and nebulizers were replaced each time an additional $5x10^6$ events had been recorded.

Mass cytometry data processing

FCS files were normalized for signal-drift using the built-in Helios normalization tool (Fluidigm) and individual sample events deconvoluted using either the debarcoder (Fluidigm) or a stand-alone debarcoder (Zunder et al., 2015) with a Mahalanobis distance of 10 and 15 respectively and a minimum barcode separation of 0.26 for both. FCS files were uploaded to the cloud-based cytometry platform Cytobank (www.cytobank.org, Beckmann Coulter) and checked for consistent signal across the entire acquisition period, as well as clean and correct barcode deconvolution. Live cell events were selected based on DNA-191Ir positivity and cisplatin-198Pt negativity. Because samples were stained with cisplatin separately, this gating step was conducted using sample tailored gating. 191Ir+ debris and cell doublets and aggregates were removed based on event length. If possible, target cells were selected by manual biaxial gating: MNB cell events were selected as CD45+CD3ε- and T cell events selected as CD45+CD3ε+. Target cells were exported as FCS files and uploaded to the Cytofkit2 package (version 2.0.1). Cells were clustered using FlowSOM (Van Gassen et al., 2015) and visualized using UMAP projections and expression overlays (Becht et al., 2018), exporting cell data with annotated clusters for further downstream analysis. For target cells that consist of cell populations that are difficult to separate cleanly from non-target cells by simple biaxial gating, such as tumor mesenchymal stromal populations, an initial analysis of high-dimensional clustering and visualization was carried out which allowed use of the full dataset to cluster and annotate events. Clusters of target cells were exported and then re-uploaded for further analysis. Three KPC tumors could not be weighed (mouse #16,17 and 18) and one mouse did not receive an IdU injection (mouse #16), so this data is not present in the respective analysis. KPC mouse #19 was only stained using the mesenchymal stroma (S) antibody panel and not the MNB and T cell panels, which gave n=18 KPC PDA tumors in which each sample was stained with all three antibody panels.

Mouse organ disaggregations

Primary fibroblast/fibroblast-like cells were expanded from the following mouse organs: pancreas, colon, small intestine, mammary tissue, shaved back skin, stomach, mesentery adipose tissue, spleen, thymus, lungs, liver, kidneys, bladder, esophagus and heart. The entire hind legs were collected and bone marrow processed separately (see below). Unless otherwise stated, tissues were isolated from female 8-week-old B6 mice. The prostate was isolated from 8-week-old male B6 mice. The number of organs required for successful fibroblast expansion from each tissue is detailed in the Supplemental Information Table. All tissues were transferred to ice-cold sterile PBS on ice. The stomach, small intestine and colon were flushed clear with PBS. Some tissues were processed manually and others were disaggregated using a GentleMACS dissociator (See Supplemental Information Table). Previous experiments had indicated which method yielded the most fibroblasts from each tissue (for a full list of methods used, see Supplemental Information Table). Each tissue was transferred to a 10 cm cell culture dish and washed once with ice-cold RPMI. For some specific tissues, DB was supplemented with 0.5 mg/mL Dispase II (Thermo Fisher, 17105041) to aid disaggregation (noted in Supplemental Information Table). For manual disaggregation, 3 mL of RT DB was added and the tissue minced using disposable scalpels, with a further 17 mL of DB added once pieces were below 3 mm and incubated at 37°C for 25 min. The cells, tissue fragments and buffer were then transferred to a centrifuge tube and the contents allowed to settle for ~10 s. The settled tissue pieces were transferred to a separate centrifuge and repeatedly mixed to break up the fragments. The contents of both centrifuge tubes were combined and quenched with 20 mL of cell culture media (CCM), consisting of 20% v/v FBS, 1% v/v HyClone Antibiotic/Antimycotic (Fisher Scientific, 11536481) and 0.2% v/v Primocin (InvivoGen, ant-pm-1) in DMEM with glucose and L-glutamine (Thermo Fisher, 41966052). Cells and remaining tissue fragments were centrifuged at 300 g for 6 min and resuspended in 40 mL CCM and transferred to a 225 cm^2 culture flask. Methods for GentleMACS tissue disaggregations were specific for each tissue (listed in Supplemental Information Table). Once the program was complete the C-tube was centrifuged at 100 g for 2 min, to ensure contents were gathered at the bottom of the tube. The sample was diluted with a further 15 mL of fresh DB, mixed by pipetting and quenched with 20 mL CCM. Cells and remaining tissue fragments were centrifuged at 300 g for 6 min and resuspended in 40 mL CCM and plated into a 225 cm^2 flask. For isolation of bone marrow stromal cells, muscle was removed from each pair of intact tibias and fibias, the ends of the bones cut with a disposable scalpel and the bone marrow flushed out with 5 mL DB using a needle and syringe. The combined bone marrow extracts were vortexed to break up clumps, quenched with 20 mL CCM, pelleted, resuspended in 40 mL CCM and transferred to a 225 cm^2 culture flask. Frozen B6 primary mouse embryonic fibroblasts (MEFs) (Generon, C57-6028) were thawed and resuspended in 40 mL CCM and transferred to a 225 cm^2 culture flask. All primary cell cultures were grown in an incubator at 37°C with 5% CO2, humidified air. Media was carefully replaced at 24 h and 48 h, taking care not to dislodge attached tissue fragments. Primary fibroblast isolations were used when the cells reached ~50% confluence, which varied between 6-15 d (Supplemental Information Table). For isolations to be analyzed by mass cytometry, cells were lifted by aspirating media, washing with sterile PBS (Thermo Fisher, 10010023) and incubating with 10 mL of Accutase Cell Detachment Solution (Sigma Aldrich, A6964) at 37°C for 10 mins. The dissociation buffer was quenched with 30 mL CCM and the cells allowed to settle in the same flask (without washing out the dissociation buffer). This step removes many non-fibroblast cell types that do not survive detachment well. The following day 40 μL of 10 mM IdU solution in 0.2 M NaOH/water was added directly to the media, mixed by swirling and the cells incubated at 37°C for 20 min. Media was aspirated, cells lifted with 10 mL Accutase Cell Detachment Solution, diluted with 20 mL PBS and centrifuged at 300 g for 6 min at 4°C. The cell pellet was resuspended in 100 μL PBS, vortexed and 100 μL of 1 μM 198Pt cisplatin in PBS added, followed by vortexing. After exactly 1 min incubation, the staining was quenched with 10 mL of CSM-I, cells pelleted, resuspended in 2 mL CSM-I, counted and $3x10^6$ cells aliquoted into a 5 mL polypropylene FACS tube. The remaining staining, acquisition and analysis steps were as described above for the *ex vivo* analysis.

Mass cytometry cell signaling panel generation

Supplier, clone and heavy-metal isotope tag of each antibody used in the cell signaling mass cytometry analysis are listed in the Supplemental Information Table. Where indicated antibodies were purchased pre-conjugated (Fluidigm). All other antibodies were labelled with the indicated metal tag using the Maxpar X8 antibody conjugation kit (Fluidigm), as described above. Cell signaling antibodies were titrated in panels against *in vitro* cell lines stimulated with recombinant cytokines and growth factors. Antibody clones were prioritized based on extensive prior validation (Kumar et al., 2020; Lun et al., 2017, 2019; Rapsomaniki et al., 2018) or confirmation of expected signal node activation during the antibody titration step. A custom 6-choose-3 barcode scheme using enriched isotopes of 105Pd, 106Pd, 108Pd, 110Pd, 113In and 115In (Trace Sciences) was generated using established methodology (Zunder et al., 2015). Stocks of 10 mM palladium/indium salt solutions in L-buffer were diluted 1:10 in 20 mM ammonium acetate ($NH_4CH_3CO_2$) (Sigma Aldrich, 372331). 127 μL of these 1 mM palladium/indium nitrate solutions were added to 2 mg of 1,4,7,10-tetraazacyclododecane-1,4,7-tris-acetic acid-10-maleimidoethylacetamide (mDOTA) (Macrocyclics, B-272) in a 1.5 mL polypropylene tube giving a 2:1 ratio of chelator:metal. Volumes were adjusted based on the accurate weight of mDOTA. After 1 min of vortexing the tube was snap frozen in dry ice/ethanol bath and stored at -80°C. Tubes were opened and lyophilized overnight in a cooled Alpha 2-4 Benchtop Lyopholizer (MartinChrist Freeze Dryers), working quickly to ensure the contents did not thaw before being desiccated. The resulting powder was dissolved to 10 mM in dry DMSO (Sigma Aldrich, D2650) and an aliquot diluted 5000x to give a 2 μM working stock. This was titrated against PFA fixed and methanol permeabilized *in vitro* cells, to mimic final assay conditions as closely as possible. Once an optimal dilution for each of the six barcodes was found 1:1:1 mixtures were generated in a 6-choose-3 barcode scheme (Zunder et al., 2015) and each of the 20 possible combinations was titrated to ensure optimal staining, before being aliquoted and stored at -20°C.

Mass cytometry signaling analysis

$1.5x10^6$ mCherry+ CD105+ pancreatic fibroblasts and $1.5x10^6$ GFP+ CD105- pancreatic fibroblasts were combined in 30 mL of reduced-serum cell culture media (CCM(0.5)), consisting of 0.5% v/v dialyzed FBS (dFBS) (Thermo Fisher, 26400044) and 1% v/v HyClone Antibiotic/Antimycotic in DMEM with glucose and L-glutamine, and plated into a 225 cm^2 cell culture flask. After 24 h, 40 μL of 10 mM IdU solution in 0.2 M NaOH/water was added directly to the media, mixed well and the cells incubated at 37°C for a further 20 min. The media was aspirated and replaced with 28 mL of warmed CCM(0.5) containing cytokine or growth factors, as detailed in the Supplemental Information Table. The conditions consisted of x1 no stimulation control and x19 recombinant cytokine or growth factor stimulations. After exactly 5 min of stimulation at 37°C, 4 mL of 16% PFA was added to the media, to give a final PFA concentration of 2%, and immediately swirled over the cells to fix. After 30 min of fixation, the media was aspirated, and the attached cells washed with PBS, CSM-I, and then PBS. 15 mL of Accutase Cell Detachment Solution was added and the flasks incubated at 37°C for 15 min. Because buffer-mediated detachment is less efficient for fixed cells, a cell scraper was used to further detach the cells from the flask and collected in a centrifuge tube and diluted with 20 mL PBS. Cells were centrifuged at 1000 g for 6 min with reduced braking, aspirated and resuspended in 2 mL PBS, vortexed and permeabilized by slowly adding 5 mL of -20°C methanol (Fisher Scientific, 10767665) with vortexing, followed by incubation at -20°C for 20 min. The methanol-permeabilized cells were diluted with 10 mL PBS and then a further 10 mL CSM-I and pelleted. Cells were resuspended in PBS, counted and a maximum of $3x10^6$ cells aliquoted into separate 5 mL polypropylene FACS tubes. After washing with 4mL of PBS and resuspending the cell pellets in void volume, one aliquot of each unique 6-choose-3 barcode dissolved in 1mL of ice-cold PBS was added to each sample and vortexed. Once a 30 min incubation at RT was complete, the cells were washed twice with 4 mL CSM-I, pooled into a single 5 mL polypropylene FACS tube in CSM-I and pelleted. The 20-sample pooled cell pellet was resuspended in the void volume and 200 μL of 100 U/mL heparin sodium salt solution and 10 μL of Fc block added. After 5 min at RT a master mix containing 20 equivalents of each antibody from the cell signaling panel (Supplemental Information Table) in 500 μL of CSM-I was added and vortexed. After staining for 2h at RT with regular vortexing, the sample was washed three times with 4 mL CSM-I and resuspended in 1 mL PBS, transferred to a larger centrifuge tube and fixed in 10 mL of 4% PFA in PBS. The sample was vortexed and stored at 4°C in the dark overnight. After the overnight fixation, the PFA/PBS was washed out with PBS and the cells incubated in 1mL of 100 ug/mL bis(2,2′-bipyridine)-4′-methyl-4-carboxybipyridine-ruthenium *N*-succinimidylester-bis(hexafluorophosphate) (ASCQ_Ru) (Sigma Aldrich, 96631) in 0.1 M sodium bicarbonate ($NaHCO_3$) (Sigma Aldrich, 31437) solution for 1h at RT, before continuing with the PBS and water washes and acquisition, as described above.

Multiplexed immunofluorescence

Multiplexed Tyramide Signal Amplification (TSA) immunofluorescence staining was performed using the BOND RX automated platform (Leica Microsystems). 4um sections of FFPE tumors were cut and mounted on charged slides. Dewaxing and heat induced epitope retrieval of slides was automated on the Bond RX, using Epitope Retrieval Solution 1 (ER1) (Leica Microsystems, AR9961) for 20 min at 100°C. Using the Research Detection System 2 (Leica Microsystems, DS9777), endogenous peroxidase was blocked using 3% v/v hydrogen peroxide (VWR, 23622.260) in Tris Buffer Saline with Tween 20 (TBST) (VWR, J77500.K8) for 10 min and the slides further blocked with 10% w/v casein (Vector, SP5020) in TBST. Antibody application, detection and TSA amplification was conducted in three sequential rounds following the same general procedure: incubation with the primary antibody in Bond Antibody Diluent (Leica Microsystems, AR9352) for 30 min, followed by detection using EnVision HRP (Agilent, K4001/4003) for 30 min, followed by a specific premixed TSA reagent (Perkin Elmer) at 1/200 for 30 min. Antibody sequence and TSA-fluorophore selection were optimized to reduce non-specific staining and tyramide binding site competition. The first staining round used mouse anti-human CD105 antibody (CST clone 3A9) at 1/200 and TSA570 (FP1488001KT). The second round used rabbit anti-human pan-CK antibody (Abcam ab9377) at 1/200 and TSA520 (FP1487001KT). The third round used mouse anti-human podoplanin antibody (Dako cloneD2/40) at 1/100 or anti-human VIM antibody (CST clone D21H3) at 1/500 and TSA650 (FP1496001KT). Following labelling with TSA, antibodies were removed using a heat stripping step in ER1 for 10 min at 100°C. This was not applied following application of the third antibody. Finally, nuclei were counterstained with 0.33 ug/ml 4′,6-diamidino-2-phenylindole (DAPI) (Thermo Fisher, 62248) for 15 min and coverslipped with ProLong Gold Antifade Mountant (Thermo Fisher, P36930). Slides were scanned using a VS120 microscope (Olympus Lifescience) at 20x and analyzed using QuPath (v0.2.0-m9) (Bankhead et al., 2017).

FACS and flow cytometry

To isolate CD105+/- CAFs directly from PDA tumors, single cell suspensions were prepared as described above for analysis by mass cytometry. Red blood cells (RBCs) were lysed using 5 mL of ice-cold 1x RBS Lysis Buffer (Biolegend, 420301) for 2 min on ice. The lysis was quenched with 20 mL FACS buffer (FB), consisting of 2% v/v FBS and 2 mM ethylenediaminetetraacetic acid (EDTA) (Thermo Fisher, 15575020) in PBS and pelleted by centrifugation at 300 g for 6 min with reduced braking. Cells were counted using a Luna Cell Counter on fluorescence mode, washed once with 20 mL PBS and stained with Live/Dead Fixable Near-IR Dead Cell Stain Kit (Thermo Fisher, L10119), using 0.25 μL of reagent in 0.5 mL of ice-cold PBS per $1x10^6$ cells. After 20 min on ice, the staining was quenched with 20 mL FB and cells pelleted. 0.25 μL of Fc block per $1x10^6$ cells was added to the void volume and cells gently mixed. After 5 min on ice, a master mix containing anti-EpCAM-FITC, anti-CD45-FITC, anti-CD31-FITC, anti-PDPN-APC (all Biolegend), anti-CD90-PE (Abcam) and anti-CD105-BV421 (BD Biosciences) was added at 0.25 μL of each antibody in 20 μL FB per $1x10^6$ cells. Cells were vortexed, stained on ice in the dark for 45 min, washed once with 20 mL FB, resuspended to $5x10^6$ cells/mL, filtered through 70 μm Filcons into 5 mL polypropylene FACS tubes and sorted on a BD FACS AriaIII (BD Biosciences) using

the gating strategy described in the manuscript. FACS sorted CD105+ and CD105- fibroblasts in CCM were centrifuged, aspirated and cells lysed in RLT buffer (QIAGEN) and RNA isolated using a RNeasy Micro Kit (QIAGEN, 74004), according to the manufacturer's instructions. For flow cytometry analysis or FACS of *in vitro* cells (e.g. isolation and surface marker analysis of CD105+/- pancreatic fibroblasts), a similar protocol was used without the RBC lysis and dead cell staining steps, and alternative fluorophore conjugates were applied. For a full list of antibodies used for flow cytometry/FACS see Supplemental Information Table. For flow cytometry/FCAS analysis all samples were analyzed on a BD LSRFortessa (BD Biosciences). Flow cytometry/FACS plots were generated in Cytobank.

Bulk RNA sequencing and analysis

RNA was isolated from FACS purified cells or whole tumor lysates at timepoints indicated in the manuscript. Indexed PolyA libraries were prepared using 50 ng of total input RNA and 16 cycles of amplification with the Agilent SureSelect Strand Specific RNA Library Prep Kit for Illumina Sequencing (Agilent, G9691B). Libraries were quantified by qPCR using a Kapa Library Quantification Kit for Illumina Sequencing Platforms (Kapa Biosystems Inc., KK4835). Paired-end 75 base-pair sequencing was carried out by clustering 1.9-2.0 pM of the pooled libraries on a NextSeq 500 Sequencer (Illumina Inc.) Pre-alignment quality control was performed using the FASTQC tool (version 0.11.3). Raw sequencing reads were aligned to the mouse reference genome GRCm38/mm10 using STAR aligner (version 2.5.1b) and gene annotation was taken from Ensembl build 92. Read counts were determined by using the *featureCounts* function from the Bioconductor package Rsubread (version 1.28.1). For analysis of pancreatic fibroblast transcriptional response to recombinant protein stimulations, a similar protocol was applied but only single-end reads were measured. Differential gene expression analysis was performed using the Bioconductor package DESeq2 (Love et al., 2014). For the *ex vivo* KPC CAF analysis, a gene was called as significantly differentially expressed if its abundance changed more than 2-fold between populations of interest, with a Benjamini-Hochberg(BH)-adjusted p-value <0.05. For the *in vitro* pancreatic fibroblast stimulation analysis, batch effect correction was performed using DESeq2 as recommended by DESeq2 workflow guidelines. A gene was considered as differentially expressed if BH-adjusted p-value <0.05 between stimulation and baseline conditions. No fold change cut-off was applied. For single gene expression comparisons, values were calculated either as TPM or scaled/normalized expression values directly from the DEseq2 analysis. For TGFB and IL1 receptor and signaling mediator gene expression comparisons, read counts from the baseline and stimulation conditions were combined for comparison of gene expression between CD105+ and CD105- fibroblasts (these genes were not significantly differentially expressed between baseline and stimulation samples). Ingenuity Pathway Analysis (Qiagen) was conducted according to manufacturer's recommendations. MCPcounter analysis was performed by converting gene names to the human annotation and using standard paramters (Becht et al., 2016).

scRNA-seq re-analysis

Single-cell mRNA sequencing (scRNA-seq) data containing mouse PDA mesenchymal cells was obtained from a publicly available dataset (Elyada et al., 2019), available at Gene Expression Omnibus (GEO) under the accession number GSE129455. Pre-processing steps, analysis and visualizations were done using the R package Seurat (Butler et al., 2018). The downloaded data is already normalized by log-normalization. The built-in function *ScaleData* was implemented to centralize expression of each gene, to shift the mean values to 0 and scale the variance from -1 to 1. Then according to best practices, we allocated 2000 of the most variable genes using the built-in function *FindVariableFeatures*. Based on the obtained variable genes, principal component analysis (PCA) was implemented by the function *RunPCA*. We estimated 50 principal components for each cell and, after performing an elbow test (function *ElbowPlot*) and JaskStraw estimation (functions *JackStraw*, *ScoreJackStraw* and *JackStrawPlot*), selected the top 20 principal components for further analysis. For cell clustering, Seurat's graph-based k-Nearest Neighbors (kNN) approach was implemented (functions *FindNeighbors* and *FindClusters*). Dimension 20 and resolution 0.5 were used as clustering parameters. UMAP method was used for data visualization (function *RunUMAP*). Scatter plot visualizations were done by Seurat's functions *DimPlot* and FeaturePlot. A similar workflow was used to analyze the Steele et al. human pancreas and PDA dataset (Steele et al., 2020) Fibroblast clusters were enriched as outlined in Figure S3E

scRNA-seq of *in vitro* pancreatic fibroblasts

scRNA-seq on *in vitro* pancreatic fibroblasts was performed at Hubrecht single Cell Genomics according to an adapted version of the SORT-seq protocol (Muraro et al., 2016) with primers as previously described (Van den Brink et al., 2017). The pancreas from 3 8-week-old female B6 mice was disaggregated and the fibroblasts expanded *in vitro* as described above. After 7 d, cells were lifted and individual single cells were plated into 3 separate 384-well plates containing 384 primers and Mineral oil. A sperate flow cytometry experiment showed the majority of cells at this time point were EpCAM-CD45-CD31-PDPN+ fibroblasts. After sorting, plates were centrifuged at 300 g for 3 min and stored at -80° C. For amplification, cells were heat-lysed at 65° C followed by cDNA synthesis using the CEL-Seq2 protocol (Hashimshony et al., 2016) and robotic liquid handling platforms. After second strand cDNA synthesis, the barcoded material was pooled into libraries of 384 cells and amplified using *in vitro* transcription. Following amplification, the rest of the CEL-Seq2 protocol was followed for preparation of the amplified cDNA library, using TruSeq Small RNA Library Kits (Illumina, 2000012). The DNA library was paired-end sequenced on a Nextseq 500 Sequencer (Illumina) using an Illumina High Output 1x75 bp Kit (Illumina Inc., 20024906). During sequencing, Read 1 was assigned 26 bp and was used for identification of the Illumina library barcode, cell barcode and Unique Molecular Identifiers (UMIs). Read 2 was assigned 60 bp and used to map to the reference transcriptome of mm10 with Burrows-Wheeler Aligner (BWA) (Anders and Huber, 2010). Data was indexed using Samtools (version 1.9)

and aggregated using the UMI-tools package (version 1.0.1). Single-cell transcriptomics analysis was done using the R package Seurat (Butler et al., 2018), as above.

In vitro fibroblast isolation and culture

Primary pancreatic fibroblasts (PaFs) were expanded *in vitro* from the pancreas of 8-week-old female B6 mice, as described above. At d7, cells were FACS sorted into LIN(CD45/CD31/EpCAM)-PDPN+CD90+CD105+ and LIN-PDPN+CD90+CD105- populations. Notably, Ficoll density gradient isolation of pancreatic fibroblasts from healthy murine pancreas, using standard methods, also yielded mixed $CD105^{pos}$ and $CD10^{5neg}$ fibroblast populations. For immortalization, cells were transduced with SV40 LT (Addgene, 13970). After selection, cells were expanded, purity checked by flow cytometry and frozen stocks made and used for downstream functional assays. GFP and mCherry expressing target cells were generated using a second-generation lentiviral system (Harris et al., 2012) (Addgene 12263 and Addgene, 12259). No puromycin selection was carried out and GFP/mCherry expressing cells were isolated by FACS. For cancer cell and fibroblast co-culture experiments $2x10^6$ mCherry+ PDA cells and 2x10^6 GFP+ PaFs were plated in 20 mL CCM(10) in a 225 cm^2 flask and analyzed after 48 h. To analyze the primary PaF surface marker changes under recombinant protein stimulation, primary PaFs were expanded *in vitro* as described, and incubated in 75 cm^2 flasks with recombinant proteins in CCM(10) (at concentrations listed in the Supplemental Information Table) for 3 d. Cells were analyzed by mass cytometry as described above. To analyze the transcriptomic responses of CD105+ and CD105- PaFs to recombinant protein stimulation, 10^5 CD105+ and CD105- PaFs were plated into 6 well plates in 2 mL CCM(0.5). The following day the media was replaced with CCM(0.5) containing recombinant cytokines or growth factors (see Supplemental Information Table) and after 6 h, cells were aspirated, washed with ice-cold PBS and lysed using RLT buffer, fully detached with a cell scraper and RNA isolated using RNeasy Mini Kit (QIAGEN, 74104), according to the manufacturer's instructions. Human pancreatic fibroblasts (hPaFs) (Generon, H-6201) were cultured in CCM, CD105+ and CD105- cells separated by FACS and cell lines generated using the lentiviral system described above with a pCSII-IRES2-hygro plasmid containing an hTERT expression inset, which was a kind gift from Dr. Farnando Calvo at the Institute of Cancer Research London, followed by 50 ug/mL hygromycin B (Thermo Fisher, 10687010) selection for 7 days.

BioMark HD multiplex qPCR

Assay primers and probes were designed using the Roche Universal Probe Library Assay Design Centre Tool (https://lifescience.roche.com/en_gb/brands/universal-probe-library.html). Where possible, primers were selected to span different exons to minimize amplification of genomic DNA. See Supplemental Information Table for primer sequences and TaqMan probe numbers. New primers and probes were validated by qPCR using Universal Mouse Reference RNA (Thermo Fisher, QS0640). cDNA was synthesized from 500 ng of RNA in a 50 μL reaction mixture of 1x Reverse Transcription Buffer (Thermo Fisher, 18067017), 1.75 mM Mg_2Cl_2 (Thermo Fisher, R0971), 2 mM dNTP Mix (Thermo Fisher, R0191), 5mM DL-Dithiothreitol (DTT) (Sigma Aldrich, 43815), 100 U/mL RNAse Inhibitor (Thermo Fisher, N8080119), 2.5 μM Random Hexamers (Thermo Fisher, N8080127) and 2500 U/mL Multiscribe Reverse Transciptase (Thermo Fisher, 4311235). Reverse transcription was carried out at 25°C for 10 min, 37°C for 60 min, 95°C for 5 min and 4°C indefinitely before being stored at -20°C. A pre-amplification of 2.5 μL of the cDNA mixture was conducted in 10 μL of 1x TaqMan Pre-Amp Master Mix (Applied Biosystems, 4391128) and a pool of all assay-specific primers at 5 nM (see Supplemental Information Table), by temperature cycling at 95°C for 10 min for 1 cycle, 95°C for 15 s and 60°C for 4 min for 14 cycles and 4 degree indefinitely until being diluted with 40 μL RNAse-free water (Thermo Fisher, 10977035) and storage at -20°C. Assay mixes for the qPCR reactions were made using 8 μM of each primer and 1 μM of the appropriate hydrolysis probe in 1x Assay Loading Reagent (Fluidigm, 85000736). Sample mixes were made by diluting the amplified cDNA 1:1 in TaqMan Universal PCR Master Mix (Applied Biosystems, 4304437) and GE Sample Loading Reagent (Fluidigm, 85000746). Samples and assays were carefully loaded on a 96x96 Dynamic Array Chip (Fluidigm, BMK-M-96.96) and analyzed according to manufacturer's instructions using standard settings, auto-exposure settings and with ROX as the passive reference dye. Raw qPCR data was analyzed using the BioMark Real-Time PCR Analysis Software (Fluidigm). Assay dependent thresholds were used to calculate cycle threshold (Ct) values and relative expression calculated as: relative expression = $2^{-\Delta Ct}$, where: ΔCt = (Ct value gene A) – (Geometric mean (Ct values house-keeping genes)). A combination of house-keeping genes (*Actb, Gapdh, Pgk1, Ppia, Tbp, Tubb4a*) was used for normalization to mitigate potential confounding issues caused by differential housekeeping-gene expression between cell lines.

Genetically engineered annimal models

KPC colonies on mixed backgrounds were bred in-house in individually ventilated cages, under pathogen-free conditions at CRUK Beatson Institute (CRUK-BI) and maintained in conventional caging with environmental enrichment, access to standard chow and water *ad libitum*. Genotyping was performed by Transnetyx (Cordoba, TN, USA). Mice of both sexes were monitored 3 times weekly and when a diagnosis of pancreatic cancer was made by abdominal palpation, tumor growth was monitored by ultrasound imaging (Fujifilm VisualSonics, Vevo 3100 preclinical imaging system). Mice were culled by Schedule 1 method, as per institutional guidelines, when exhibiting moderate symptoms of PDA, such as swollen abdomen, loss of body conditioning resembling cachexia or reduced mobility. RFP KPC colonies on a mixed background were maintained under pathogen-free conditions at the UoM and monitored as described above. B6.*Rag1*$^{-/-}$ mice and B6.*Batf3*$^{-/-}$ mice were maintained at the UoM and both sexes used at >12 weeks of age. KPN mice of both sexes at 6-12 weeks age were injected intraperitoneally with a single dose of 2 mg tamoxifen (Sigma Aldrich, T5648) and primary colorectal tumors collected at clinical end point, defined as animal weight loss and/or hunching and/or cachexia. Female *MMTV-PyMT* mice were monitored for tumor growth by caliper measurement and tumors collected when total tumor volume was

>900 mm^3, typically across multiple foci. KP mice of both sexes at 8-14 weeks of age were anaesthetized using isoflurane and intranasally administered with 50 μL of $1x10^6$ PFU replication-deficient Cre-expressing adenovirus, as per standard protocols (Meuwissen et al., 2001) and monitored for tumor formation by computerized tomography scans. Resulting lung tumors were collected 16 weeks after adenoviral induction. Female $BRAF^{V600E}$ mice, 8-12-weeks old, had 1 mg freshly prepared tamoxifen in ethanol applied to their shaven back. 4 weeks after transgene induction, the back skin was UV irradiated with a UV6 lamp (UV280-380 nm) every week for 4 weeks. Once tumors were visible, tumor volume was measured weekly and collected at a minimum volume of 500 mm^3.

Subcutaneous co-transplant model

The majority of subcutaneous co-transplant studies in this study used syngeneic female B6 mice of 14 weeks of age. Where indicated female 14 week old NSG mice were used. Both male and female *Rag1*$^{-/-}$ and *Batf3*$^{-/-}$ mice of mixed ages >12 weeks old were used where indicated and sex/age matched across cohorts. During optimization, KPC PDA cells on a B6 background were injected in 100 μL PBS (Thermo Fisher, 10010056) but this fails to retain fibroblasts within the growing tumor (see manuscript Figure S6). For all subsequent transplants Growth Factor Reduced Matrigel (Corning, 356231) was used. Where possible, a single Matrigel lot was used for experiments to minimize the impact of lot-to-lot variation. Cancer cells (BL6KPC-TB32043 or BL6KPC-TB32047 from B6 fully backcrossed KPC mice) and fibroblasts were lifted 20-24 h before the day of injection using Accutase Cell Detachment Solution and $6x10^6$ and $3x10^6$ cells plated, respectively into 225 cm^2 flasks. Cancer cells were cultured in CCM(10) and fibroblasts in CCM. One the day of injection, cells were lifted again using Accutase Cell Detachment Solution, washed twice with ice-cold PBS and counted in triplicate using a Luna Cell Counter on bright-field mode. The required number of cancer cells and fibroblasts were combined in 5 mL polypropylene FACS tubes, washed once more with PBS and carefully and fully aspirated. Ice-cold Matrigel were added using pre-cooled pipette tips to obtain a final concentration of each cell type of 5000 cells/uL and gently mixed on ice. Braun Omnican 50 Insulin Syringe/Needles (VWR, 9151117) were used to accurately measure 20 μL of cell/Matrigel mix with no dead-volume, which was injected subcutaneously into the right flank of the mouse (therefore giving 10^5 cancer cells and 10^5 fibroblasts). 20 μL injection volume was found to be the optimal balance between generating plugs with no necrosis and consistent injection volume. Tumor width and length were measured (blinded to the study) by calipers and tumor volume (V) calculated as V = (2xwidth)xlength)/2. Study end point was V>900 mm^3, if the mouse lost >10% body weight or if a mouse's health showed any other signs of deterioration e.g. loss of activity, altered breathing, behavioral changes. For gene expression analysis, subcutenous tumors were collected at day 10, lysed in 500 uL Trizol utilizing a TissueLyzer (QIAGEN) and RNA isolated using DirectZol kits (Zymo) following manufacturers recommendations.

Immunohistochemistry of subcutaneous tumors

Subcutaneous co-transplant tumors were collected at 7 and 30 d after implantation. Large tumors were cut in half. Samples were fixed for 24h in 10% v/v Neutral Buffered Formalin (Genta Medical, BIB10L), processed and paraffin embedded (Leica Microsystems). 4um cut sections were mounted onto charged glass slides and stained manually. Slides were dewaxed by x3 5 min xylene washes and rehydrated in 100%, 90% then 70% ethanol for 1 min each. Heat induced epitope retrieval was conducted using a Biocare Declocker at 110°C for 15 min and allowed to cool for 15 min using Low pH Target Retrieval Buffer Ph6 (Agilent, S236984). Slides were cooled in running water for 2 min and endogenous peroxidases blocked using 3% v/v hydrogen peroxide in TBST for 10 min. Following further washing in TBST, slides were blocked with 10% w/v casein in TBST for 20 min. Staining was conducted using chicken anti-GFP antibody (Abcam, ab13970) at 1/500 in TBST for 1 h at RT, followed by x2 5 min TBST washes. Detection of the primary antibody used a biotinylated goat anti-chicken IgG antibody (Abcam, ab207998) at 1/200 in TBST for 30 min at RT, followed by Vectastain Elite ABC HRP Kit (Vector, PK-6100) for 30 mins at RT, x2 5 min TBST washes and 3,3'-diaminobenzidine (DAB) (Agilent, K3467) for 5 min. Finally, nuclei were counterstained with 1x Shandon Gill Haematoxylin (Thermo Fisher, 6765005) and then dehydrated and coverslips applied before being scanned using an SCN400 (Leica microsystems) and analyzed using QuPath.

CRISPR-Cas-9 gene editing

For *in vitro* fibroblasts, we found nucleofection-based CRISPR-Cas-9 methods to be far superior to other methods to generate efficient gene knockouts. For each target gene, three separate gRNAs were designed (Synthego 'Mulit-Guide' platform), such that their spatial distribution favored large (>50bp) genomic deletions rather that small indels, resulting in improved knockout efficiency and consistency. gRNAs were synthesized and chemically modified to improve stability and reduce intracellular immune responses. Ribonucleoprotein (RNP) complexes were formed by diluting 2 μL of 100 μM of multi-gRNA (Synthego) in Tris-EDTA (TE) (Synthego) and 1 μL of 20 μM recombinant Cas-9 (Integrated DNA Technologies (IDT), 1081059) in RNase-free PBS in 12 μL Primary Cell P3 Nucleofector solution (Lonza, V4XP-3032) and incubating at RT for 20 min. To $2.5x10^5$ cells in 5 μL Nucelofector solution, 0.8 μL of Electroporation Enhancer Solution (IDT, Alt-R Cas9 Electroporation Enhancer, 2 nmol) was added, followed by 15 μL of the RNP solution and mixed by pipetting. This was transferred to a well of a 20 μL Nucleocuvette Strip (Lonza, V4XP-3032) and transfected using a 4D-Nucleofector Core Unit (Lonza), using the CM-137 program. Cells were allowed to rest for 3 min before being plated in CCM and cultured as normal. Transfection with a pool of x2 separate non-targeting (NT) gRNAs (Synthego) was used to generate control cells. Gene knockout was confirmed in a split of the cells at the protein level by flow cytometry after 7 d, using IFNγ stimulation to induce expression of *H2Ab1* and *Cd74*. Surface MHCII expression was measured and CD74 expression was measured by intra-

cellular staining (CD74 is predominantly located in the ER/endosomes), using the FOXP3 Fixation/ Permeabilization kit. Cells were not purified further as gene knockout was consistently >95% for all targeted genes.

QUANTIFICATION AND STATISTICAL ANALYSIS

Plotting and statistical tests were performed in Prism (version 7, GraphPad Software Inc.) or R Statistical Software. For RNA-seq data visualization, differentially expressed genes (DEGs) from DESeq2 were scaled by library size using the function *estimateSizeFactors*, the data transformed by the function *normTransform* and the obtained expression values used for visualization. Heatmap plots were drawn using the R package ComplexHeatmap. Heatmap visualization of CyTOF data was achieved by first processing the data using the R package flowCore (Hahne et al., 2009). According to best practices, data was transformed by hyperbolic arc-sine with cofactor = 5 by the function *asinh*. The z-score was calculated by the function *scale* and heatmaps drawn using the R package ComplexHeatmap. Principle Component Analysis (PCA) plots were generated using the *pcaplot* function. For the abundance/phenotype cross-cluster correlation analysis, the number of cells in each FlowSOM cluster as a percentage of the total number of gated cells from each sample was used as the abundance input data. To calculate the fraction of proliferating and dying cells in each cluster, FCS files containing all target cells, including FlowSOM cluster annotation were exported from Cytofkit2 and uploaded to FlowJo (version 10.6.2, BD Life Sciences). S-phase cells were defined as cells with both Ki67 mass intensity signal $\geq$ 20 and IdU mass intensity signal $\geq$ 20. Dying cells were defined as cells with cleaved caspase-3 (CC3) mass intensity signal $\geq$ 8. The abundance of each FlowSOM cluster and the percentage of S-phase and dying cells within each FlowSOM cluster for each sample was exported and used as the phenotypic input data for the cross-correlation analysis. Since all antibody panels were measured on each of the 18/19 PDA samples, the abundance, proliferation and apoptosis data for each of the 20 FlowSOM clusters from each of the three panels (60 total clusters) was concatenated into one data frame for these 18 samples. Correlation analysis was performed on selected abundance, proliferation and apoptosis comparisons (see manuscript for specific comparisons), using Spearman correlation measurement with permutation testing adjusted for multiple testing using Benjamini-Hochberg correction. The correlation results were visualized by the R package corrplot.

Cancer Cell, Volume *39*

Supplemental information

Single-cell analysis defines a pancreatic fibroblast lineage that supports anti-tumor immunity

Colin Hutton, Felix Heider, Adrian Blanco-Gomez, Antonia Banyard, Alexander Kononov, Xiaohong Zhang, Saadia Karim, Viola Paulus-Hock, Dale Watt, Nina Steele, Samantha Kemp, Elizabeth K.J. Hogg, Joanna Kelly, Rene-Filip Jackstadt, Filipa Lopes, Matteo Menotti, Luke Chisholm, Angela Lamarca, Juan Valle, Owen J. Sansom, Caroline Springer, Angeliki Malliri, Richard Marais, Marina Pasca di Magliano, Santiago Zelenay, Jennifer P. Morton, and Claus Jørgensen

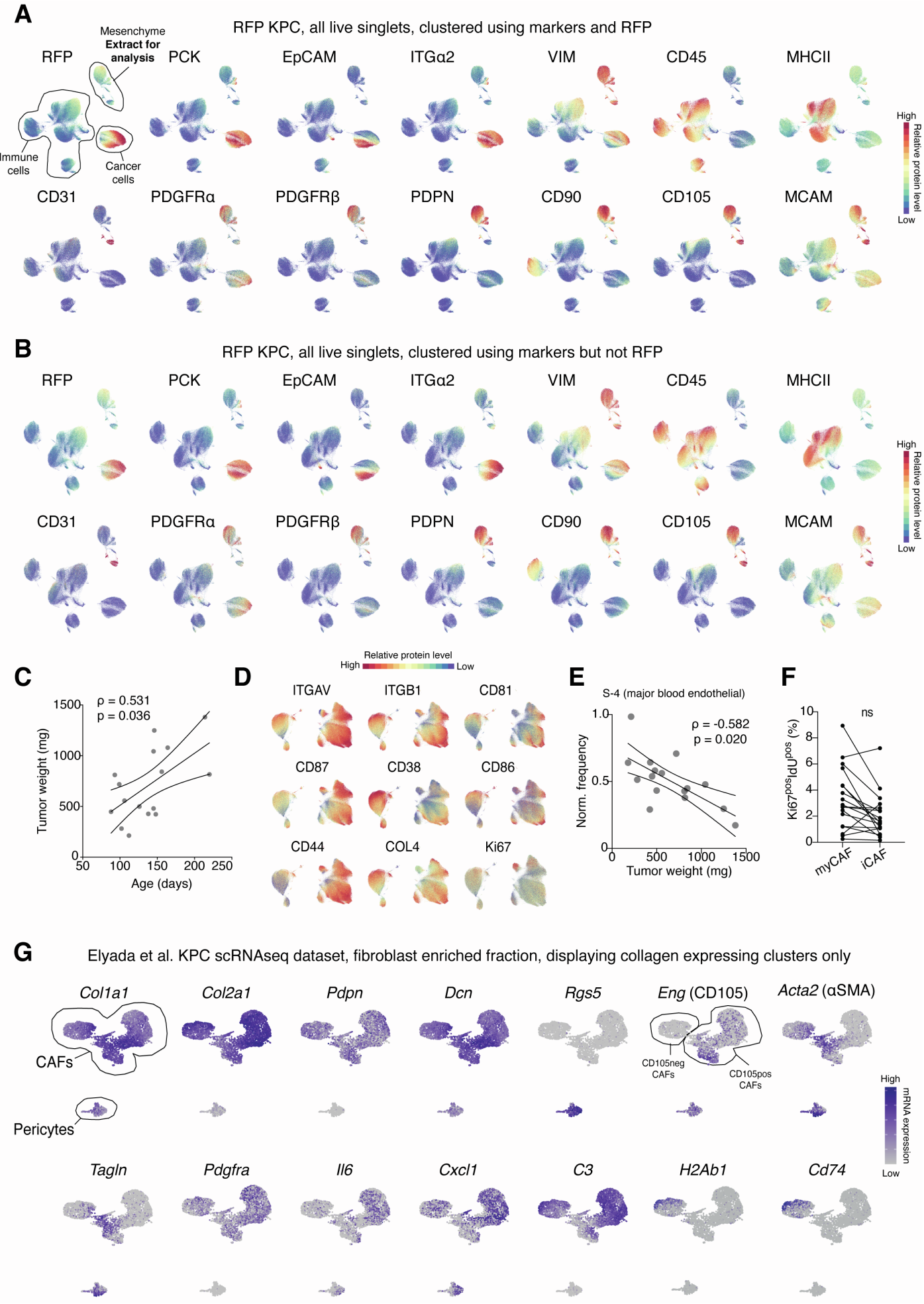
A
RFP KPC, all live singlets, clustered using markers and RFP
Mesenchyme
Extract for analysis
Immune cells
Cancer cells
RFP
PCK
EpCAM
ITGα2
VIM
CD45
MHCII
CD31
PDGFRα
PDGFRβ
PDPN
CD90
CD105
MCAM
High
Relative protein level
Low
B
RFP KPC, all live singlets, clustered using markers but not RFP
RFP
PCK
EpCAM
ITGα2
VIM
CD45
MHCII
CD31
PDGFRα
PDGFRβ
PDPN
CD90
CD105
MCAM
High
Relative protein level
Low
C
ρ = 0.531
p = 0.036
Tumor weight (mg)
Age (days)
D
Relative protein level
High
Low
ITGAV
ITGB1
CD81
CD87
CD38
CD86
CD44
COL4
Ki67
E
S-4 (major blood endothelial)
ρ = -0.582
p = 0.020
Norm. frequency
Tumor weight (mg)
F
ns
Ki67posIdUpos (%)
myCAF
iCAF
G
Elyada et al. KPC scRNAseq dataset, fibroblast enriched fraction, displaying collagen expressing clusters only
Col1a1
Col2a1
Pdpn
Dcn
Rgs5
Eng (CD105)
Acta2 (αSMA)
CAFs
CD105neg CAFs
CD105pos CAFs
Pericytes
High
mRNA expression
Low
Tagln
Pdgfra
Il6
Cxcl1
C3
H2Ab1
Cd74

Supplemental Figure 1, related to Figure 1. Phenotypic and compositional heterogeneity of pancreatic cancer-associated mesenchymal cells

(A) UMAP projection of all live, single cells from an RFP KPC tumor sample using all phenotypic markers to drive clustering. PCK: pan-cytokeratin.

(B) UMAP projection of all live, single cells from an RFP KPC tumor sample, as for (A), but RFP is not used to drive clustering. PCK: pan-cytokeratin.

(C) Correlation between KPC mouse age and weight of tumors collected at humane endpoint. ρ=Spearman correlation coefficient, 90% confidence intervals displayed. Mean age of mice included in study was 142 days.

(D) UMAP projection from Figure 1A, displaying relative signal intensity of additional phenotypic markers not included in Figure 1D.

(E) Spearman correlation analysis between the relative frequency of the endothelial cell subset, S-4 and PDA tumor weight. ρ=Spearman correlation coefficient, 90% confidence intervals displayed.

(F) Frequency of myCAFs (αSMA^{high} PDGFRα^{low}) and iCAFs (αSMA^{low} PDGFRα^{high}) in S-phase (Ki67^{pos} IdU^{pos}).

(G) Reanalysis of single cell transcriptomic data from Elyada et al. The pre-defined fibroblast enriched fraction was used and only collagen expressing cells analyzed. Data is displayed as UMAP projections with overlaid relative expression levels of example genes, including canonical fibroblast genes (*Col1a1/2*, *Pdpn*, *Dcn*), the canonical pericyte gene (*Rgs5*), *Eng* (the gene that encodes CD105) and myCAF-, iCAF- and apCAF-associated genes (*Acta2*, *Tagln* and *Pdgfra*, *Il6*, *Cxcl1*, *C3*, and *H2Ab1*, *Cd74* respectively).

Samples are compared using Spearman correlation adjusted for multiple testing using Benjamini-Hochberg correction (C, E) or paired t-test (F). ns. non-significant

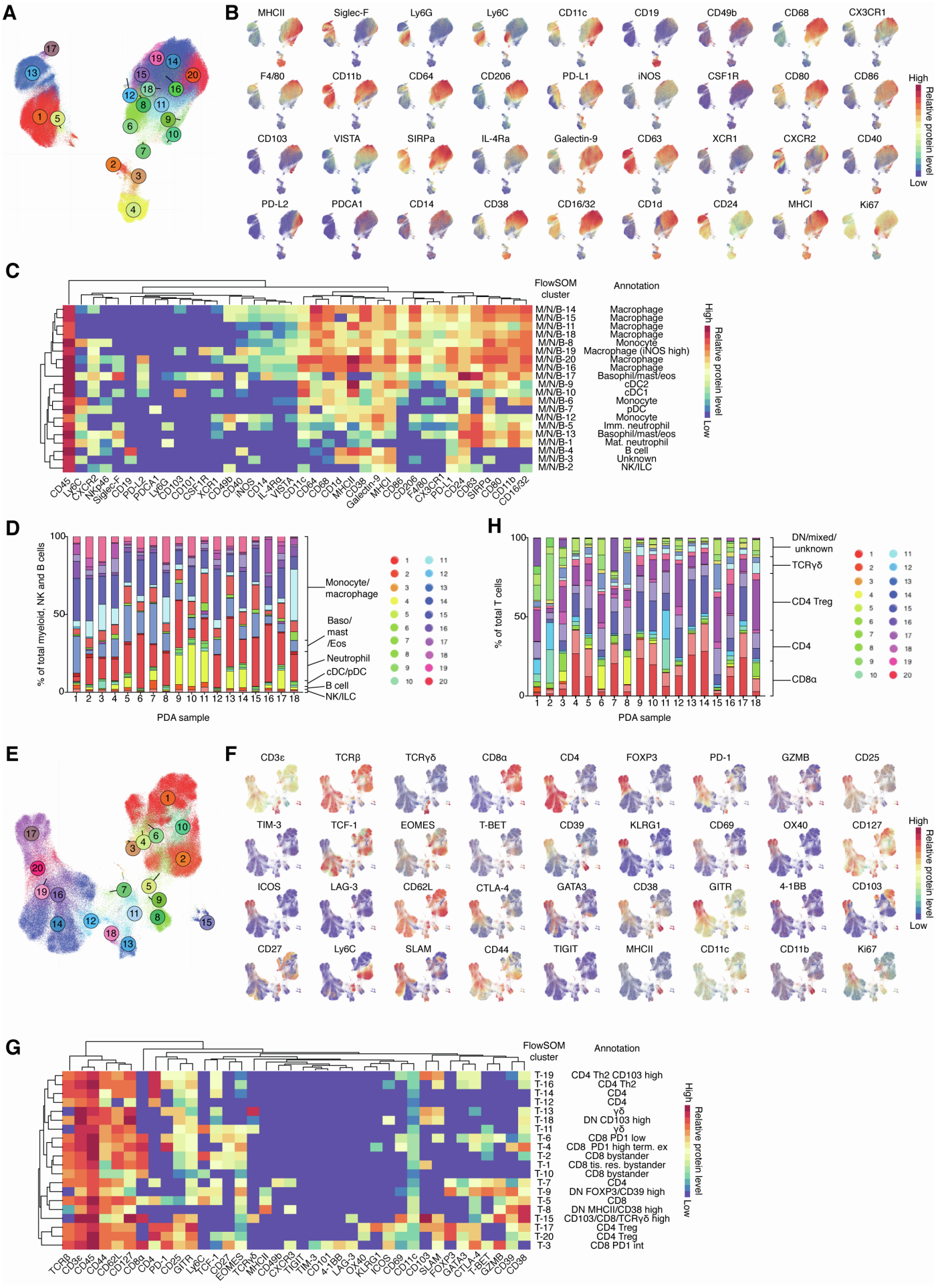
A
B
MHCII
Siglec-F
Ly6G
Ly6C
CD11c
CD19
CD49b
CD68
CX3CR1
F4/80
CD11b
CD64
CD206
PD-L1
iNOS
CSF1R
CD80
CD86
CD103
VISTA
SIRPa
IL-4Ra
Galectin-9
CD63
XCR1
CXCR2
CD40
PD-L2
PDCA1
CD14
CD38
CD16/32
CD1d
CD24
MHCI
Ki67
High
Relative protein level
Low
C
FlowSOM cluster
Annotation
M/N/B-14 Macrophage
M/N/B-15 Macrophage
M/N/B-11 Macrophage
M/N/B-18 Macrophage
M/N/B-8 Monocyte
M/N/B-19 Macrophage (iNOS high)
M/N/B-20 Macrophage
M/N/B-16 Macrophage
M/N/B-17 Basophil/mast/eos
M/N/B-9 cDC2
M/N/B-10 cDC1
M/N/B-6 Monocyte
M/N/B-7 pDC
M/N/B-12 Monocyte
M/N/B-5 Imm. neutrophil
M/N/B-13 Basophil/mast/eos
M/N/B-1 Mat. neutrophil
M/N/B-4 B cell
M/N/B-3 Unknown
M/N/B-2 NK/ILC
CD45 Ly6C CXCR2 NKp46 Siglec-F CD19 PD-L2 PDCA1 Ly6G CD103 CD101 CSF1R XCR1 CD49b CD40 iNOS CD14 IL-4Ra VISTA CD11c CD64 CD68 CD1d MHCII CD38 Galectin-9 MHCI CD86 CD206 F4/80 CX3CR1 PD-L1 CD24 CD63 SIRPa CD80 CD11b CD16/32
D
% of total myeloid, NK and B cells
PDA sample
Monocyte/ macrophage
Baso/ mast /Eos
Neutrophil
cDC/pDC
B cell
NK/ILC
H
% of total T cells
PDA sample
DN/mixed/ unknown
TCRγδ
CD4 Treg
CD4
CD8α
E
F
CD3ε TCRβ TCRγδ CD8α CD4 FOXP3 PD-1 GZMB CD25
TIM-3 TCF-1 EOMES T-BET CD39 KLRG1 CD69 OX40 CD127
ICOS LAG-3 CD62L CTLA-4 GATA3 CD38 GITR 4-1BB CD103
CD27 Ly6C SLAM CD44 TIGIT MHCII CD11c CD11b Ki67
High
Relative protein level
Low
G
FlowSOM cluster
Annotation
T-19 CD4 Th2 CD103 high
T-16 CD4 Th2
T-14 CD4
T-12 CD4
T-13 γδ
T-18 DN CD103 high
T-11 γδ
T-6 CD8 PD1 low
T-4 CD8 PD1 high term. ex
T-2 CD8 bystander
T-1 CD8 tis. res. bystander
T-10 CD8 bystander
T-7 CD4
T-9 DN FOXP3/CD39 high
T-5 CD8
T-8 DN MHCII/CD38 high
T-15 CD103/CD8/TCRγδ high
T-17 CD4 Treg
T-20 CD4 Treg
T-3 CD8 PD1 int
TCRβ CD3ε CD45 CD44 CD62L CD127 CD8α CD4 PD-1 CD25 GITR Ly6C TCF-1 CD27 EOMES TCRγδ MHCII CD49b CXCR3 TIGIT TIM-3 CD101 4-1BB LAG-3 OX40 KLRG1 ICOS CD69 CD11c CD103 SLAM FOXP3 GATA3 CTLA-4 T-BET GZMB CD39 CD38
High
Relative protein level
Low

Supplemental Figure 2, related to Figure 2. Phenotypic and compositional heterogeneity of pancreatic cancer-associated immune subsets

(A) UMAP projection of single $CD45^{pos}$ $CD3^{neg}$ cells (MNB: Myeloid, NK, B cell) from 18 of the 19 tumors analyzed for the mesenchymal stroma with color-coded FlowSOM clusters (1-20). Each sample contributes an equal number of cells to the dataset. Total of $5x10^5$ cells displayed.

(B) UMAP projection (from (A)) displaying overlaid relative signal intensity of example phenotypic markers.

(C) Heatmap of marker median mass intensities (MMIs) displayed as z-scores. Each FlowSOM MNB cluster is grouped by unsupervised hierarchical clustering based on marker MMIs. Cell-type annotations based on canonical phenotypic markers are listed.

(D) Stacked bar graph displaying relative abundance of KPC PDA MNB FlowSOM clusters grouped into major MNB cell sub-types.

(E) UMAP projection of single $CD45^{pos}$ $CD3^{pos}$ cells (T cells) from 18 of the 19 tumors analyzed for the mesenchymal stroma with color-coded FlowSOM clusters (1-20). Each sample contributes an equal number of cells to the dataset. Total of $5x10^5$ cells displayed.

(F) UMAP projection from (E) displaying overlaid relative signal intensity of example phenotypic markers.

(G) Heatmap of marker median mass intensities (MMIs) displayed as z-scores. Each FlowSOM T cell cluster is grouped by unsupervised hierarchical clustering based on marker MMIs. Cell-type annotations based on canonical phenotypic markers are listed.

(H) Stacked bar graph displaying relative abundance of KPC PDA T cell FlowSOM clusters grouped into major T cell sub-types.

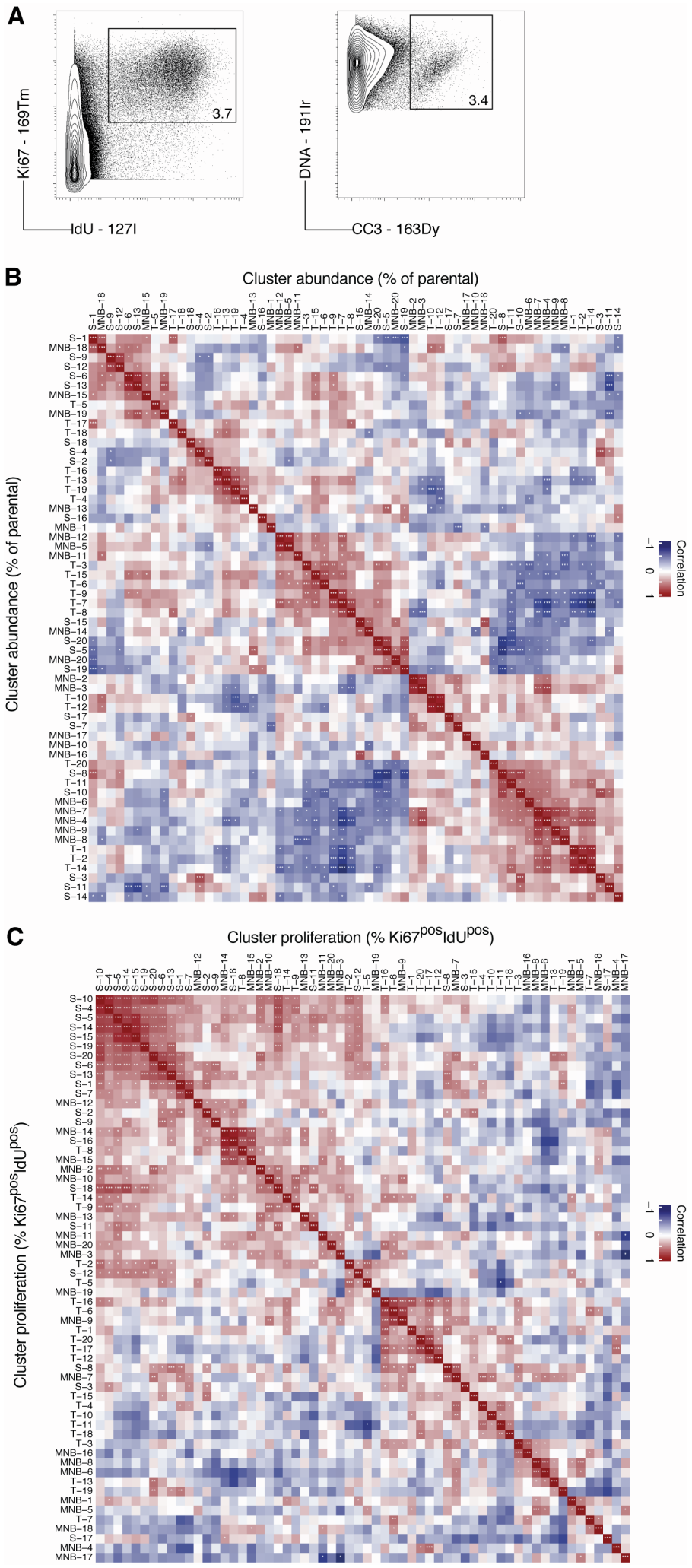
A
Ki67 - 169Tm
IdU - 127I
3.7
DNA - 191Ir
CC3 - 163Dy
3.4
B
Cluster abundance (% of parental)
Cluster abundance (% of parental)
Correlation
C
Cluster proliferation (% Ki67posIdUpos)
Cluster proliferation (% Ki67posIdUpos)
Correlation

Supplemental Figure 3, related to Figure 2. Co-regulated CAF and immune subsets within the PDA tumor microenvironment

(A) Example mass cytometry (MC) data with Ki67 and IdU (left) and DNA and cleaved caspase-3 (CC3) (right). Cells in S-phase, at the time the tumor was collected, can be clearly identified as $Ki67^{pos}$ IdU^{pos} and apoptotic cells as $CC3^{pos}$.

(B-C) Correlation matrix with Spearman correlation coefficients of all pairwise comparisons of mesenchymal stromal and immune cell subset frequencies (B) and proliferation rates (C). All pairwise apoptosis rate correlations are included in Table S2.

Samples were compared using Spearman correlation adjusted for multiple testing using Benjamini-Hochberg correction (J,K). *p<0.05, **p<0.01, ***p<0.001.

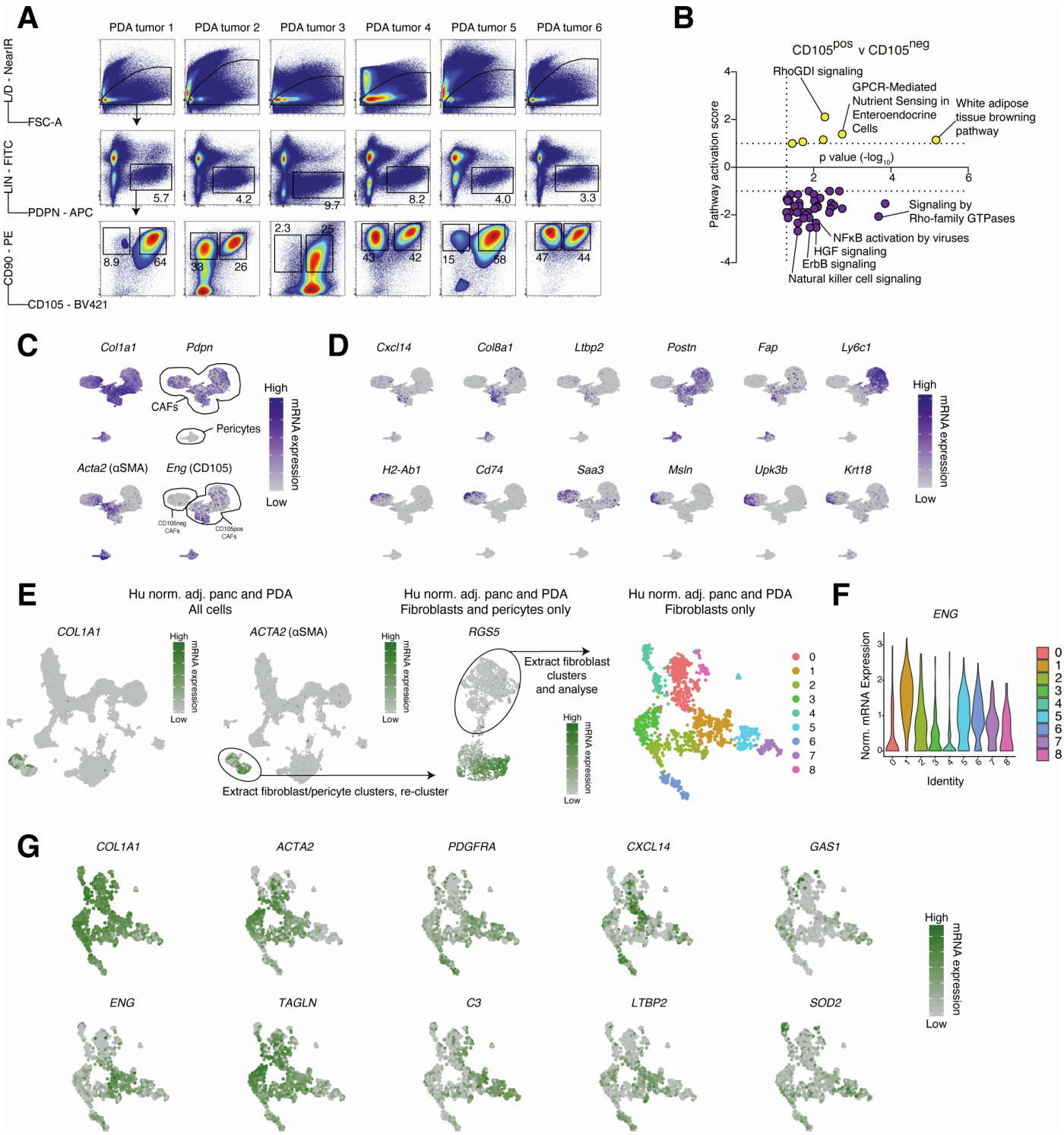
A
PDA tumor 1
PDA tumor 2
PDA tumor 3
PDA tumor 4
PDA tumor 5
PDA tumor 6
L/D - NearIR
FSC-A
LIN - FITC
PDPN - APC
CD90 - PE
CD105 - BV421
5.7
4.2
9.7
8.2
4.0
3.3
8.9
64
38
26
2.3
25
43
42
15
58
47
44
B
CD105pos v CD105neg
RhoGDI signaling
GPCR-Mediated Nutrient Sensing in Enteroendocrine Cells
White adipose tissue browning pathway
p value (-log10)
Pathway activation score
Signaling by Rho-family GTPases
NFκB activation by viruses
HGF signaling
ErbB signaling
Natural killer cell signaling
C
Col1a1
Pdpn
CAFs
Pericytes
Acta2 (αSMA)
Eng (CD105)
CD105neg CAFs
CD105pos CAFs
High
mRNA expression
Low
D
Cxcl14
Col8a1
Ltbp2
Postn
Fap
Ly6c1
H2-Ab1
Cd74
Saa3
Msln
Upk3b
Krt18
E
Hu norm. adj. panc and PDA
All cells
COL1A1
ACTA2 (αSMA)
Hu norm. adj. panc and PDA
Fibroblasts and pericytes only
RGS5
Extract fibroblast clusters and analyse
Extract fibroblast/pericyte clusters, re-cluster
Hu norm. adj. panc and PDA
Fibroblasts only
F
ENG
Norm. mRNA Expression
Identity
G
COL1A1
ACTA2
PDGFRA
CXCL14
GAS1
ENG
TAGLN
C3
LTBP2
SOD2

Supplemental Figure 4, related to Figure 3. CD105 expression discriminates two distinct CAF populations in murine and human PDA

(A) FACS gating used to isolate EpCAM^{neg} CD31^{neg} CD45^{neg} CD90^{pos} PDPN^{pos} - CD105^{pos} (n=6) and - CD105^{neg} (n=6) PDA CAFs. L/D: Live/Dead, LIN: EpCAM CD31 CD45. Scatter gating for singlets is not shown.

(B) Ingenuity Pathway Analysis (IPA) of isolated PDA CAF gene expression, displaying pathway activation score. Displaying plots for positively enriched (enriched in CD105^{pos}, yellow) (B) and negatively enriched (enriched in CD105^{neg}, purple) (C).

(C-D) Reanalysis of single cell transcriptomic data from Elyada et al. The pre-defined fibroblast enriched fraction was used and only collagen expressing cells analyzed. Data is displayed as UMAP projections with overlaid expression levels of example genes, including canonical fibroblast genes (*Col1a1*, *Pdpn*, *Acta2*) and Eng (the gene that encodes CD105) (C), genes with increased expression in CD105^{pos} PDA CAFs (*Cxcl14*, *Col8a1*, *Ltbp2*, *Postn*, *Fap* and *Ly6c1*) and gene with increased expression in CD105^{neg} PDA CAFs (*H2Ab1*, *Cd74*, *Saa3*, *Msln*, *Up3kb* and *Krt18*) (D).

(E) Single cell transcriptomic analysis of human (Hu) PDA tumor (n=14) and normal adjacent (norm adj) (n=2) (Steele et al., 2020). Displayed as UMAP projections with the expression levels of listed genes overlaid. The method for extracting fibroblast cells is shown using example genes to navigate appropriate clusters. Fibroblast clusters are visualized by color-coding (right).

(F) Violin plots displaying *ENG* expression levels (standard Seurat normalized) of the fibroblast clusters from (E). Plots display maximum and minimum data range with width representing probability density.

(G) UMAP projection of fibroblasts from (E), with overlaid expression of *COL1A1* and ENG, myCAF-associated genes (*ACTA2* and *TAGLN*), iCAF-associated genes (*PDGFRA* and *C3*), example CD105^{pos} fibroblast signature genes (*CXCL14* and *LTBP2*) and example CD105^{neg} fibroblast signature genes (*GAS1* and *SOD2*).

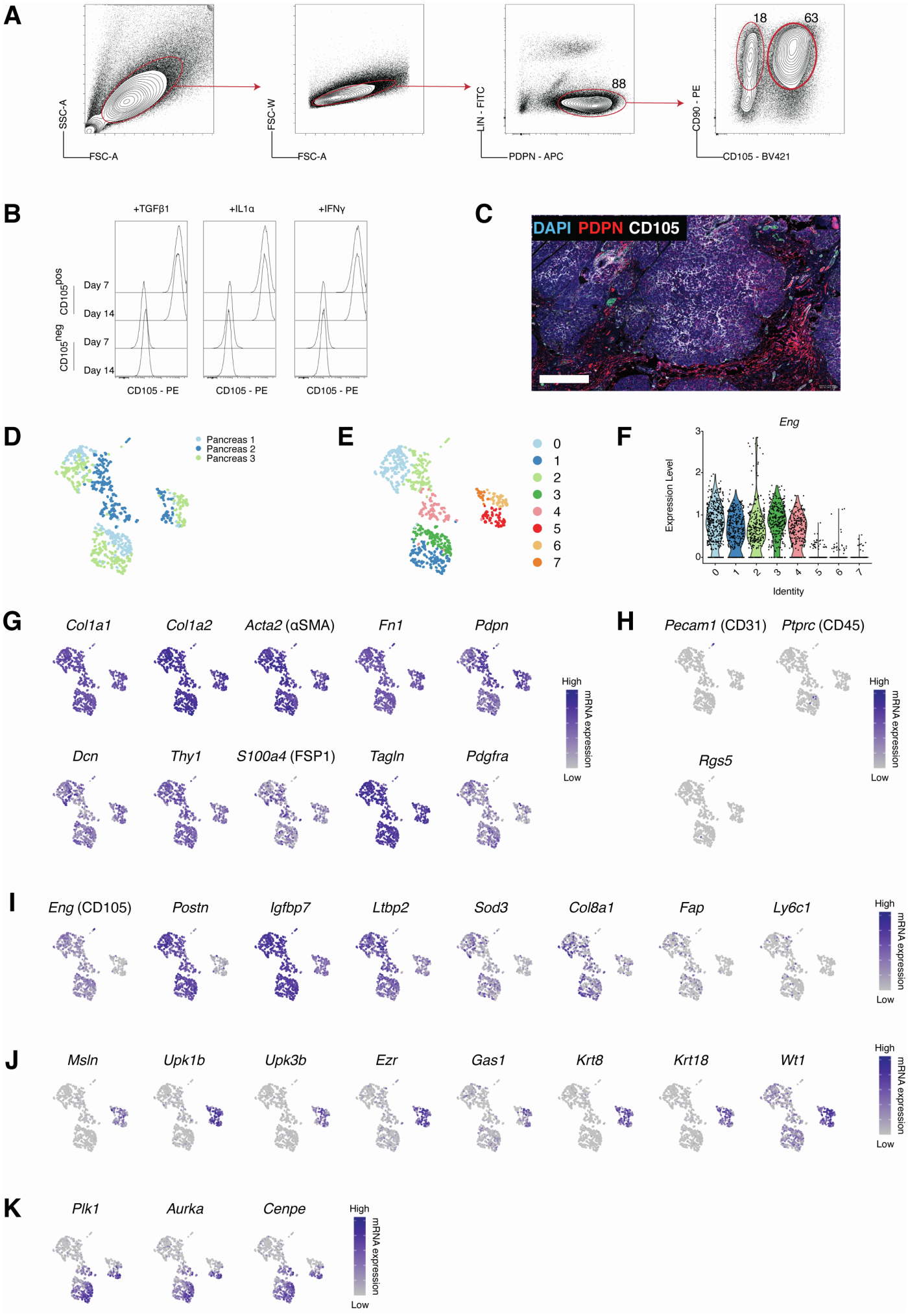
A
SSC-A
FSC-A
FSC-W
FSC-A
LIN - FITC
PDPN - APC
88
CD90 - PE
CD105 - BV421
18
63
B
+TGFβ1
+IL1α
+IFNγ
CD105pos
CD105neg
Day 7
Day 14
Day 7
Day 14
CD105 - PE
CD105 - PE
CD105 - PE
C
DAPI PDPN CD105
D
Pancreas 1
Pancreas 2
Pancreas 3
E
0
1
2
3
4
5
6
7
F
Eng
Expression Level
Identity
G
Col1a1
Col1a2
Acta2 (αSMA)
Fn1
Pdpn
Dcn
Thy1
S100a4 (FSP1)
Tagln
Pdgfra
High
mRNA expression
Low
H
Pecam1 (CD31)
Ptprc (CD45)
Rgs5
High
mRNA expression
Low
I
Eng (CD105)
Postn
Igfbp7
Ltbp2
Sod3
Col8a1
Fap
Ly6c1
High
mRNA expression
Low
J
Msln
Upk1b
Upk3b
Ezr
Gas1
Krt8
Krt18
Wt1
High
mRNA expression
Low
K
Plk1
Aurka
Cenpe
High
mRNA expression
Low

Supplemental Figure 5, related to Figure 4. Phenotypic plasticity of mesenchymal marker expression

(A) Representative FACS gating strategy to isolate CD105^{pos} and CD105^{neg} pancreatic fibroblasts (PaFs) after 7 days of *in vitro* expansion from normal healthy pancreas. L/D: Live/Dead, LIN: EpCAM CD31 CD45. Plots are representative of n=8 experiments.

(B) Flow cytometry analysis of CD105 in populations of purified CD105^{pos} and CD105^{neg} PaFs after 7 and 14 days in culture with TGFβ1, IL1α or IFNγ. Plots are representative of n=4 experiments.

(C) Representative immunohistochemistry (IHC) analysis of normal but inflamed human pancreas tissue, adjacent to PDA tumors. Stained with DAPI (blue) and with antibodies targeting podoplanin (PDPN) (red) and CD105 (white). Scale bar = 750 µm.

(D-J) Single cell transcriptomic analysis of *in vitro* expanded fibroblasts from healthy mouse pancreas (n=3), after 7 days of culture (same time point for the FACS isolation described in (A)). Displayed as UMAP projections (D, E, G-K). Comparison of the n=3 samples demonstrates concordant results (D). Clusters are defined in (E) and *Eng* gene expression in each cluster displayed (F). Expression levels of example genes are overlaid, including canonical fibroblast genes (G), canonical genes of endothelial, immune and perivascular cells (H), *Eng* and other CD105^{pos} fibroblast signature genes (I), CD105^{neg} signature and mesothelial-associated genes (J) and cell cycle-associated genes (K).

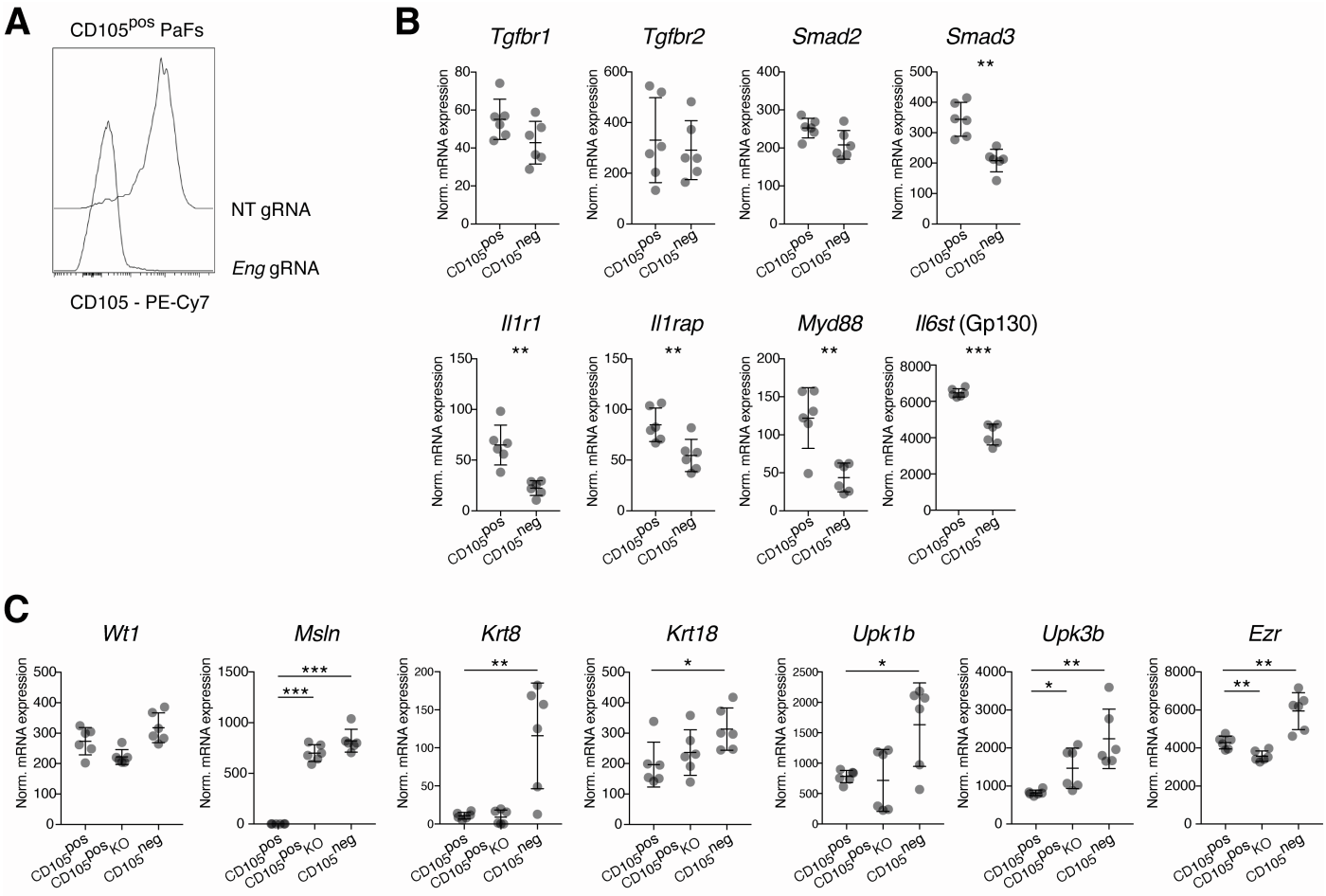
A
CD105pos PaFs
NT gRNA
Eng gRNA
CD105 - PE-Cy7
B
Tgfbr1
Tgfbr2
Smad2
Smad3
Il1r1
Il1rap
Myd88
Il6st (Gp130)
Norm. mRNA expression
CD105pos
CD105neg
C
Wt1
Msln
Krt8
Krt18
Upk1b
Upk3b
Ezr
CD105pos
CD105posKO
CD105neg

Supplemental Figure 6, related to Figure 5. Differential signaling engagement of CD105^{pos} and CD105^{neg} PaFs

(A) Flow cytometry validation of knockout of cell surface CD105 in CD105^{pos} pancreatic fibroblasts (PaFs) by CRISPR-Cas-9 gene editing.

(B) mRNA expression of genes associated with TGFβ signal transduction (*Tgfrb1*, *Tgfbr2*, *Smad2* and *Smad3*), IL1 signal transduction (*Il1r1*, *Il1rap* and *Myd88*) and *Il6st* (Gp130) in CD105^{pos} (n=6) and CD105^{neg} (n=6) PaFs. Gene expression measured by RNA-seq and quantified as DEseq2 median ratio normalized expression values. Displaying expression values as mean±standard deviation (SD).

(C) mRNA expression of genes associated with mesothelial identity in CD105^{pos}, CD105^{pos} KO and CD105^{neg} PaFs, Gene expression measured by RNA-seq and quantified as DEseq2 median ratio normalized expression values. Displaying expression values as mean±standard deviation (SD).

Samples are compared using unpaired t-test (B-C). ns. non-significant, *p<0.05, **p<0.01, ***p<0.001.

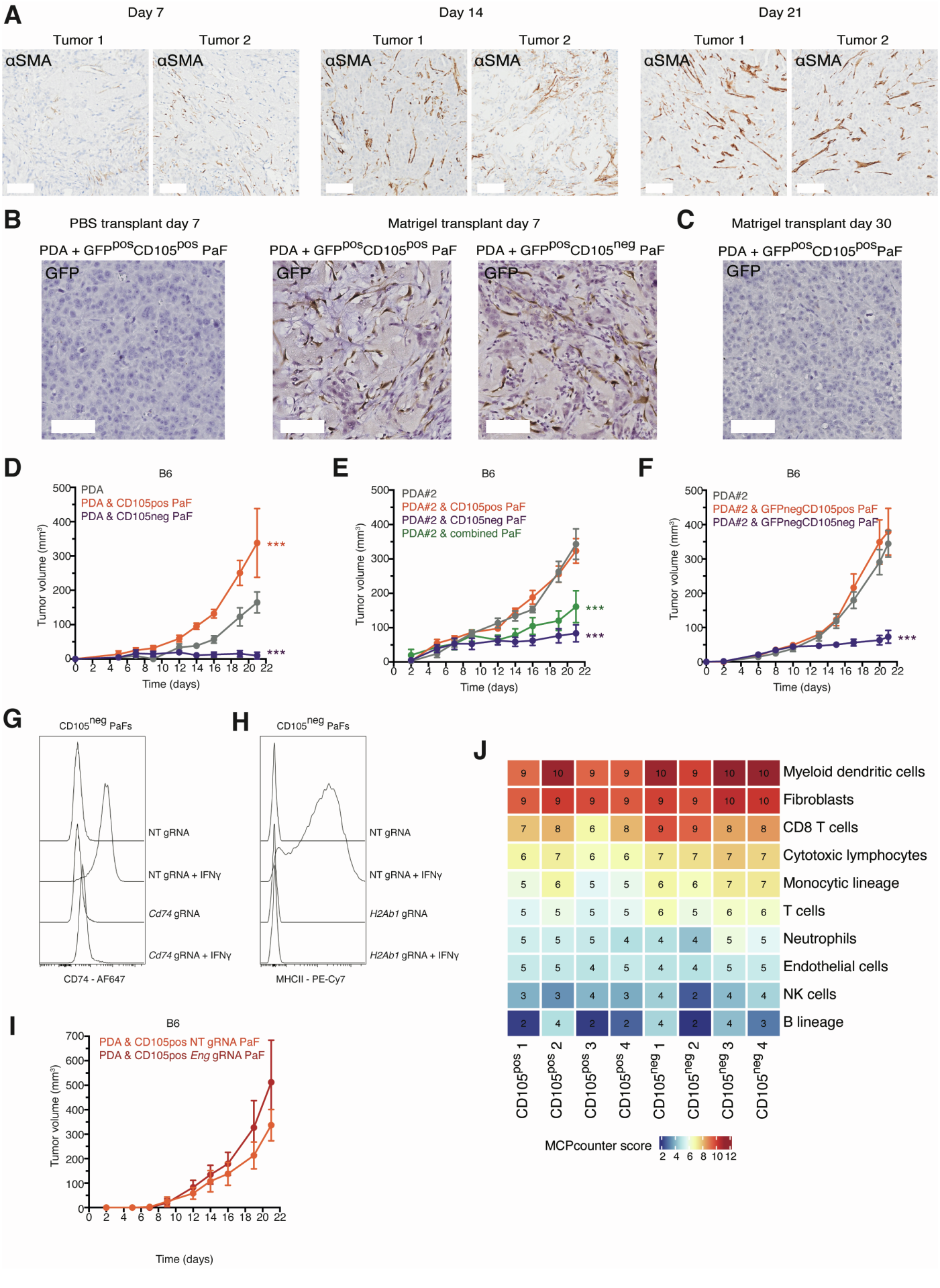
A
Day 7
Day 14
Day 21
Tumor 1
Tumor 2
αSMA
B
PBS transplant day 7
Matrigel transplant day 7
PDA + GFPposCD105pos PaF
PDA + GFPposCD105neg PaF
GFP
C
Matrigel transplant day 30
PDA + GFPposCD105posPaF
D
B6
PDA
PDA & CD105pos PaF
PDA & CD105neg PaF
Tumor volume (mm3)
Time (days)
***
E
PDA#2
PDA#2 & CD105pos PaF
PDA#2 & CD105neg PaF
PDA#2 & combined PaF
F
PDA#2 & GFPnegCD105pos PaF
PDA#2 & GFPnegCD105neg PaF
G
CD105neg PaFs
NT gRNA
NT gRNA + IFNγ
Cd74 gRNA
Cd74 gRNA + IFNγ
CD74 - AF647
H
H2Ab1 gRNA
H2Ab1 gRNA + IFNγ
MHCII - PE-Cy7
I
PDA & CD105pos NT gRNA PaF
PDA & CD105pos Eng gRNA PaF
J
Myeloid dendritic cells
Fibroblasts
CD8 T cells
Cytotoxic lymphocytes
Monocytic lineage
T cells
Neutrophils
Endothelial cells
NK cells
B lineage
CD105pos 1
CD105pos 2
CD105pos 3
CD105pos 4
CD105neg 1
CD105neg 2
CD105neg 3
CD105neg 4
MCPcounter score

Supplemental Figure 7, related to Figure 6. CD105^{neg} fibroblasts restrict tumor growth *in vivo*

(A) Immunohistochemistry (IHC) of subcutaneous tumors from mono-transplanted KPC PDA tumor cells in Matrigel at indicated time points. Stained with an αSMA targeting antibody and Haematoxylin. Represetative of n=4-5 tumors. Scale bar = 80 µm.

(B) IHC of subcutaneous tumors from co-transplanted KPC PDA tumor cells and GFP^{pos} pancreatic fibroblasts (PaFs) into syngeneic B6 mice. Stained with a GFP targeting antibody and Haematoxylin. No GFP^{pos} fibroblasts are observed in the growing tumors after 7 days when the cells are injected in PBS (left) but are highly abundant in growing tumors in which cells are injected in Matrigel (right). Scale bar = 80 µm.

(C) No GFP^{pos} fibroblasts are retained 30 days after KPC PDA tumor cells and GFP^{pos} PaFs are co-transplanted. This likely represents a limitation of this model for studies of long-term cancer cell and fibroblast interactions *in vivo*.

(D-F) Tumor growth of subcutaneous injection of 10^5 PDA tumor cells or co-transplantation with 10^5 CD105^{pos} or CD105^{neg} pancreatic fibroblasts (PaFs) in syngeneic B6 mice. Shown are independent experiment from Figure 6B (D), with alternative KPC PDA cell line from a fully backcrossed B6 mouse (E) and with PaFs with no GFP expression (F). n=5 mice per condition.

(G, H) Flow cytometry validation of CD74 (I) and MHCII (J) knock out in CD105^{neg} PaFs by CRISPR-Cas-9 gene editing.

(I) Tumor growth of subcutaneous injection of 10^5 PDA tumor cells co-transplanted with 10^5 CD105^{pos} PaFs with Eng expression disrupted by CRISPR-Cas-9 gene editing. CD105^{pos} PaFs transfected with non-targeting (NT) gRNAs are used as control. n=5 mice per condition.

(J) MCPcounter analysis of bulk gene expression profiles of subcutaneous KPC PDA and CD105^{pos} PaFs or CD105^{neg} PaF co-transplanted tumors at day 10.

Data is displayed as mean tumor volumes±standard error of the mean (SEM) (D-F and I).

Conditions are compared using 2-way ANOVA (B-G). *$p<0.05$, **$p<0.01$, ***$p<0.001$.

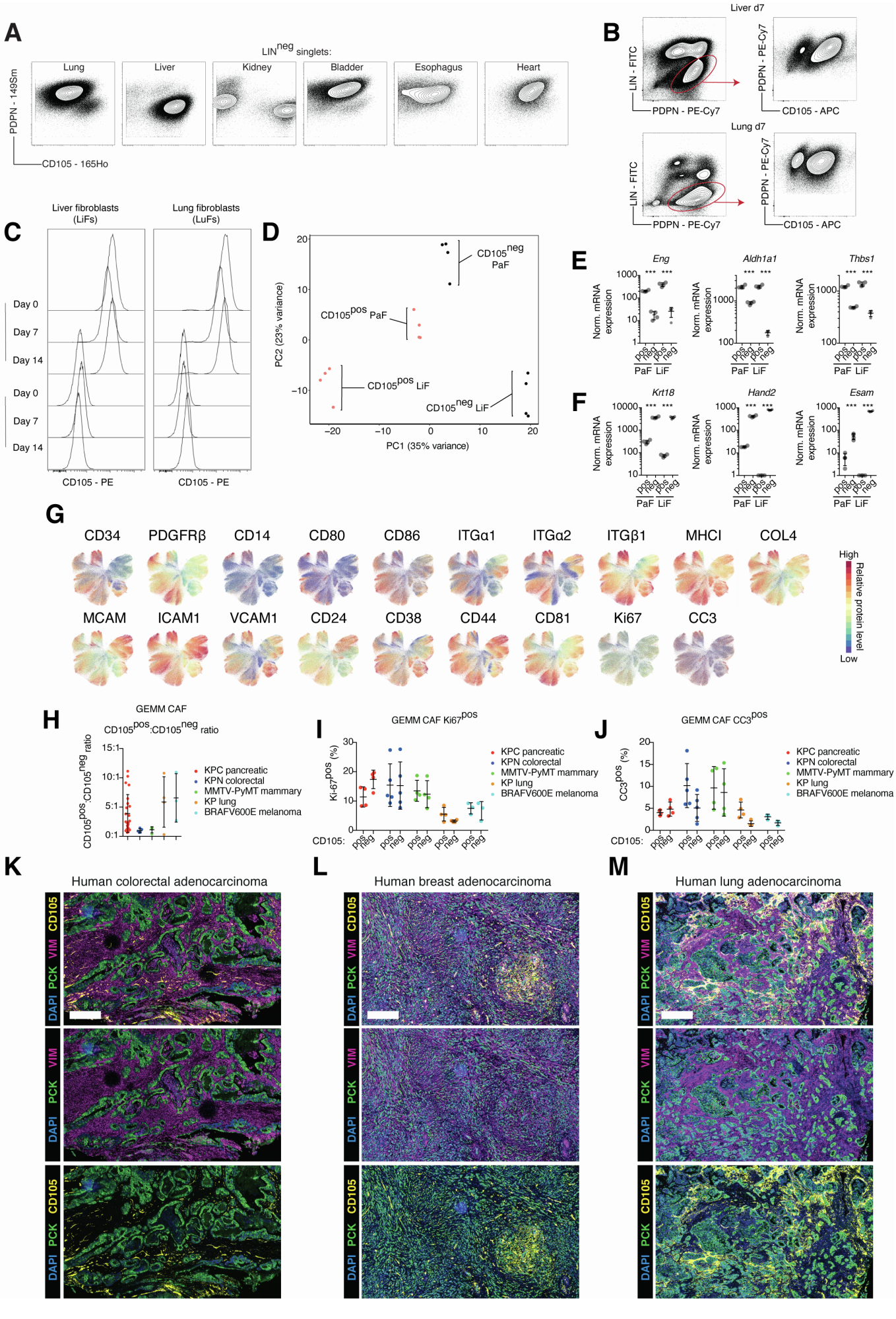
A
LIN^neg singlets:
Lung
Liver
Kidney
Bladder
Esophagus
Heart
PDPN - 149Sm
CD105 - 165Ho
B
Liver d7
LIN - FITC
PDPN - PE-Cy7
PDPN - PE-Cy7
CD105 - APC
Lung d7
LIN - FITC
PDPN - PE-Cy7
PDPN - PE-Cy7
CD105 - APC
C
Liver fibroblasts (LiFs)
Lung fibroblasts (LuFs)
CD105^pos isolation
Day 0
Day 7
Day 14
CD105^neg isolation
Day 0
Day 7
Day 14
CD105 - PE
CD105 - PE
D
CD105^neg PaF
CD105^pos PaF
CD105^pos LiF
CD105^neg LiF
PC2 (23% variance)
PC1 (35% variance)
E
Eng
Aldh1a1
Thbs1
Norm. mRNA expression
pos neg pos neg pos neg
PaF LiF
F
Krt18
Hand2
Esam
Norm. mRNA expression
pos neg pos neg pos neg
PaF LiF
G
CD34
PDGFRβ
CD14
CD80
CD86
ITGα1
ITGα2
ITGβ1
MHCI
COL4
MCAM
ICAM1
VCAM1
CD24
CD38
CD44
CD81
Ki67
CC3
High
Relative protein level
Low
H
GEMM CAF
CD105^pos:CD105^neg ratio
CD105^pos:CD105^neg ratio
15:1
10:1
5:1
0:1
KPC pancreatic
KPN colorectal
MMTV-PyMT mammary
KP lung
BRAFV600E melanoma
I
GEMM CAF Ki67^pos
Ki-67^pos (%)
CD105: pos neg pos neg pos neg pos neg pos neg
KPC pancreatic
KPN colorectal
MMTV-PyMT mammary
KP lung
BRAFV600E melanoma
J
GEMM CAF CC3^pos
CC3^pos (%)
CD105: pos neg pos neg pos neg pos neg pos neg
KPC pancreatic
KPN colorectal
MMTV-PyMT mammary
KP lung
BRAFV600E melanoma
K
Human colorectal adenocarcinoma
DAPI PCK VIM CD105
DAPI PCK VIM
DAPI PCK CD105
L
Human breast adenocarcinoma
DAPI PCK VIM CD105
DAPI PCK VIM
DAPI PCK CD105
M
Human lung adenocarcinoma
DAPI PCK VIM CD105
DAPI PCK VIM
DAPI PCK CD105

Supplemental Figure 8, related to Figure 7. CD105^{pos} and CD105^{neg} fibroblasts are identified in normal and tumor-bearing tissues

(A) Mass cytometry (MC) analysis of *in vitro* expanded, low passage, primary fibroblast isolations from mouse organs not displayed in Figure 7A. Cells expressing canonical markers of epithelial, immune, endothelial and perivascular cells are excluded from the analysis and live, singlets are displayed in plots showing PDPN and CD105 levels. LIN: EpCAM CD45 CD31

(B) Flow cytometry analysis of EpCAM^{neg} CD45^{neg} CD31^{neg} (LIN^{neg}) and PDPN^{pos} liver (top) and lung (bottom) fibroblasts from day 7 primary cell isolations, an earlier time-point than the analysis of these isolations by MC in Figure 7A and Figure S7A.

(C) Flow cytometry analysis of purified and CD105^{pos} and CD105^{neg} liver (LiF) and lung (LuF) fibroblasts after 1 and 2 weeks of *in vitro* culture. Plots are representative of n=4 experiments.

(D) Principle component (PC) analysis of differentially expressed genes between *in vitro* expanded CD105^{pos} and CD105^{neg} LiFs and pancreatic fibroblasts (PaFs).

(E-F) mRNA expression of genes associated with CD105 expression in liver and pancreatic fibroblasts. Gene expression measured by RNA-seq and quantified as DEseq2 median ratio normalized expression values. Displaying expression values as mean ± standard deviation (SD).

(G) UMAP projection from Figure 7B, displaying relative intensity of additional phenotypic markers not included in Figure 7F.

(H) MC analysis of the ratio of CD105^{pos}:CD105^{neg} CAFs in tumors from genetically engineered mouse models (GEMMs) of pancreatic (KPC) (n=23), colorectal (KPN) (n=5), mammary (MMTV-PyMT) (n=4), lung (KP) (n=4) and melanoma (BRAF^{v600E}) (n=3) cancer. Data from the n=19 PDA tumor samples analyzed in Figure 1 were combined to increase the accuracy of the ratio measured for the pancreatic GEMM tumors. Displayed as mean ± standard deviation (SD).

(I-J) MC analysis of proliferation (I) and apoptosis (J) rates of CD105^{pos} and CD105^{neg} GEMM CAFs. n=5 tumors for each genotype (paired CD105^{pos} and CD105^{neg} fractions). Displayed as mean ± SD.

(K-M) Immunohistochemistry (IHC) analysis of additional representative human colorectal (K), breast (L) and lung adenocarcinoma (M) tumor samples stained for pan-cytokeratin (PCK) (green), vimentin (VIM) (purple), CD105 (yellow) and DAPI (blue). Scale bar = 500 μm.